Fall 12-3-2019

MULTISCALE MODELING OF FRACTURE IN QUASI-BRITTLE MATERIALS USING BIFURCATION ANALYSIS AND ELEMENT ELIMINATION METHOD

Keyvan Zare Rami
University of Nebraska-Lincoln, keyvan.zare@huskers.unl.edu

MULTISCALE MODELING OF FRACTURE IN QUASI-BRITTLE MATERIALS USING BIFURCATION ANALYSIS AND ELEMENT ELIMINATION METHOD

by

Keyvan Zare-Rami

A DISSERTATION

Presented to the Faculty of

The Graduate College at the University of Nebraska

In Partial Fulfillment of Requirements

For the Degree of Doctor of Philosophy

Major: Engineering

(Civil Engineering)

Under the Supervision of Professor Yong-Rak Kim

Lincoln, Nebraska

December 3, 2019

MULTISCALE MODELING OF FRACTURE IN QUASI-BRITTLE MATERIALS USING BIFURCATION ANALYSIS AND ELEMENT ELIMINATION METHOD

Keyvan Zare-Rami, Ph.D.

University of Nebraska, 2019

Advisor: Prof. Yong-Rak Kim

Analyzing the fracture of heterogeneous materials is a complex problem, due to the fact that the mechanical behavior of a heterogeneous material is strongly dependent on a variety of factors, such as its microstructure, the properties of each constituent, and interactions between them. Therefore, these factors must be effectively taken into account for accurate analysis, for which the multiscale method has been widely used. In this scheme, the computational homogenization method is used to obtain the effective macroscopic properties of a heterogeneous material based on the response of a Representative Volume Element (RVE). The growth of damage in an RVE can be simulated by using common damage theories (such as formation of microcracks) and treated according to standard homogenization theories, which results in degradation of the effective mechanical properties of the material. In most cases, increasing the loading further causes microcracks to accumulate and to consequently form a localized band within the RVE, which may become sufficiently large as compared to the size of the RVE. Standard homogenization approaches have several theoretical shortcomings in dealing with localized RVE that bring into question their viability. This study aims to develop and implement methods to account for localization of RVE

and then reflecting it as a discontinuity on the macroscale model within a two-way coupled multiscale framework. In the proposed method, localization of RVE is assessed by bifurcation analysis, which is performed on the anisotropic tangent stiffness tensor of the RVE. The anisotropic tangent stiffness tensor is obtained by separately applying normal and shear displacement boundary conditions on the damaged RVE at each time step. Once the bifurcation analysis meets the onset of weak discontinuity requirement, a discontinuity is inserted on the macroscale model. The element elimination method is used to simulate the discrete representation of cracks on the macroscale model. The entire algorithm was implemented in the form of a two-way linked multiscale code in FORTRAN. Additionally, certain examples were solved using the developed code to demonstrate the viability of the proposed method. The results show that this approach can successfully simulate fracture in a heterogeneous quasi-brittle material without losing its key microstructural details.

To my parents and to my dear Azadeh

Acknowledgement

I would like to thank my PhD advisor, Prof. Yong-Rak Kim, for giving me this great opportunity to join his research group and his guidance and support throughout these five years. I must express my appreciation to Prof. David Allen, for kindly sharing the multiscale code with me so I could work on them for this study. I would also like to thank my dissertation committee: Prof. Chung Song, Prof. Yuris Dzenis, and Prof. Chungwook Sim for taking time to read my dissertation and their valuable comments and suggestions. I would like to warmly thank all my colleagues for the perfect working and social atmosphere during these years. Last in this list but first in my heart, I would like to thank to my fiancée, Azadeh Mostafavi, for all her love and support.

Contents

List of Figures

List of Tables

Chapter 1

Introduction

1.1 Background

Almost all materials are heterogeneous at some length scales. In the continuum length scale, heterogeneity is defined as any discontinuity and contrast in properties. When a heterogeneous material is loaded, its nonuniform microstructure causes a nonuniform distribution of stress and strain throughout the material [Nemat-Nasser and Hori, 2013]. As the loading increases, the material starts to degrade at certain regions that experience higher stress and/or have weaker properties. In quasi-brittle materials, material degradation occurs in forms of nucleation and growth of microcracks. It has been shown that a further increase in loading can result in accumulation and coalescence of microcracks and, consequently, failure of the material.

Akcaoglu et al. [Akcaoglu et al., 2005] quantified the density of microcracks in fiber-reinforced cement paste samples under different stress levels. This work showed that sample failure is due to the accumulation of microcracks, which is controlled by the microstructure of the mixture. Wang et al. [Wang et al., 2007] investigated

fracture of a metal matrix composite using the in situ scanning electron microscopy (SEM). Their work showed that microcracks typically nucleate along the particle-matrix interface where bonding between phases is weaker, and visible macrocracks are the result of coalescence of microcracks, as shown in Figure 1.1.

The microstructural characteristics of a material, such as morphological characteristics, properties of individual phases, and interaction between phases, play an important role in nucleation and accumulation of microcracks and, consequently, in the propagation of macrocracks. Ideally, the most straightforward analysis approach to account for microstructural characteristics is to model them explicitly. However, such a modelling of microstructural details in a single model, which is also known as direct numerical simulation (DNS), is often impractical from a computational point of view. Fortunately, in most cases, the effective microscale properties is sufficient to predict macroscale behaviors with reasonable accuracy. There are many studies that have accounted for the microstructural characteristics of materials and have implicitly related them to macroscale crack propagation models [Xia et al., 1995, Moorthy and Ghosh, 1998, Bazant and Oh, 1983, Budarapu and Rabczuk, 2017]. Especially over the past few decades, several studies have used multiscale approaches to link macroscale crack propagation to microscale damage mechanisms. These studies used the homogenized properties that were calculated over the microscale model to predict crack propagation in heterogeneous materials. Although many studies have shown the multiscale approach to be capable of dealing with material degradation due to microscale damage, there has been little agreement on how to approach failure and post-failure of microscale model in this framework.

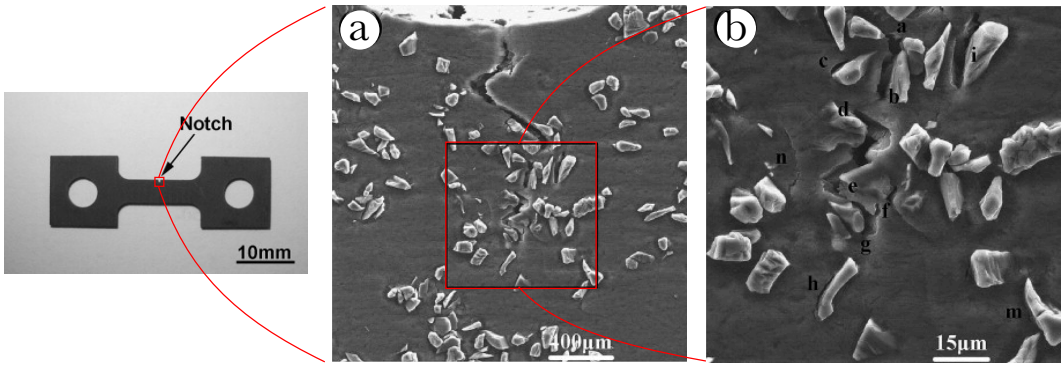

Figure 1.1: Development of microcracks in a particulate composite material [Wang et al., 2007].

1.2 Knowledge Gap

In an standard multiscale method, the effective macroscale properties of a heterogeneous material are obtained using standard homogenization methods on a Representative Volume Element (RVE). Using standard homogenization methods, growth of damage in RVE is presented in the form of degradation of the effective properties. In most cases, a further increase in loading causes the RVE to first become localized and then to fail. Many researchers have interpreted localization or failure of RVE to be formation of a discontinuity on the macroscale model. However, a review of the literature shows that researchers have not agreed upon the following subjects:

- How failure or localization of a material at a microscale model should be assessed.
- How the homogenization method should be applied on a microscale model with a localized deformation pattern.
- How the failure of the microscale model should be reflected on the macroscale

model.

1.3 Research Objectives

The objective of this dissertation is to develop a multiscale method that can be used to simulate the fracture process in heterogeneous materials, thereby at least partially filling the aforementioned gaps. More specifically, this dissertation seeks to incorporate the following functionalities into a multiscale method framework:

- A new failure criterion for heterogeneous materials that incorporates material degradation due to microcrack development that occurs at a microscale model.
- A fracture simulation method that is compatible with the multiscale method and is able to represent a discontinuity in the macroscale model.

This study provides the theoretical framework and proof-of-concept by verifying the numerical implications of the framework. To fully demonstrate the functionality of this approach, validation is performed by comparing the simulation results with experimental data. Also, the implications of the proposed framework is limited to two-dimensional (2D) cases; however, the concept is applicable to three-dimensional (3D) cases as well.

1.4 Hypothesis and Approach

This study hypothesizes that a two-way linked multiscale approach equipped with a proper criterion to assess microscale model failure and an effective method to simulate cracking in the macroscale model can effectively model crack propagation in

heterogeneous materials. The overall sketch of this approach is depicted in Figure 1.2. This research proposes that the following steps be considered in the multiscale fracture simulation approach:

- Analyzing a heterogeneous system is performed by dividing the problem into two separate length scales. The effective constitutive model of macroscale model is derived from a microscale representative volume element (RVE) through a two-way linked multiscale approach. This approach takes into account the softening behavior of the material caused by development of evenly distributed micro-damage within the RVE (for a detailed discussion, see section Core Part No. 1: Two-way Linked Multiscale Modeling). The cohesive zone model (CZM) is used to simulate the microdamage mechanism within an RVE.

- As loading increases, microcracks may coalescence and create a weak band while its length is comparable to the RVE's length scale [Souza and Allen, 2011]. At this stage, the RVE loses its material stability; however, it may still be able to carry some load. It is assumed that the creation of a weak band is equivalent to creation of a weak discontinuity surface that can be identified by performing bifurcation analysis on tangent stiffness matrix of RVE (for a detailed discussion, see section Core Part No. 2: Localization of RVE).

- Localization of an RVE determines whether a crack propagates/nucleates at the macroscale model. In this process, it is assumed that when the weak discontinuity criterion is satisfied for an RVE, material separation occurs at the corresponding location on the macroscale model. In general, this assumption may not be true, but it is reasonable for quasi-brittle materials where the transition between forming a weak discontinuously band and complete separation of

material is relatively negligible. To model material separation at the macroscale model, an element elimination technique that explicitly inserts a strong discontinuity in the Finite Element (FE) solution was selected (for a detailed discussion, see section Core Part No. 3: Crack simulation Using Element Elimination Method).

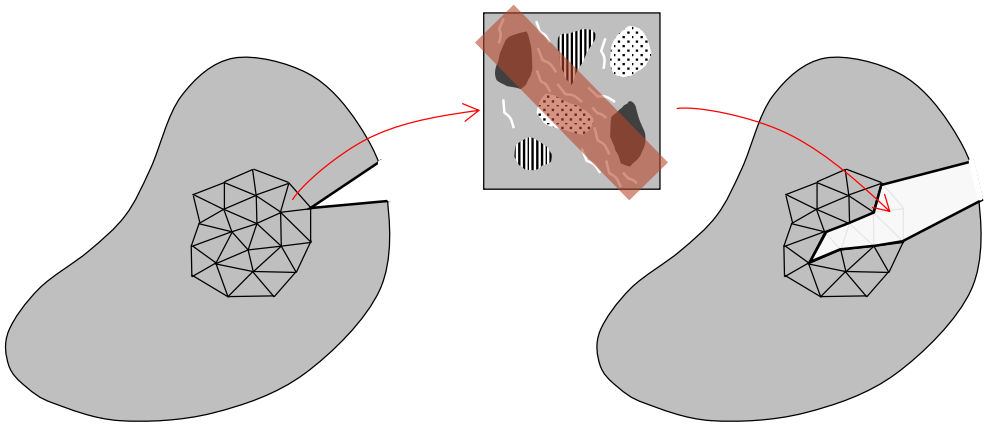

Figure 1.2: The sketch of multiscale simulation of fracture.

1.5 Dissertation Outline

Following Chapter 1: Introduction, this dissertation is organized as follows:

Chapter 2: Literature Review

Chapter 2 provides a brief overview of studies that used a multiscale approach to simulate fracture in heterogeneous materials. This literature review focuses on studies that incorporate numerical implication of the two-way linked multiscale approach in their framework. The objectives of this chapter are to present the current understanding of this approach and knowledge gaps.

Chapter 3: Theory and Background

The third chapter is concerned with the theoretical background of topics that contribute to the objectives of this dissertation. The proposed approach is built on three main components: two-way linked multiscale modeling, bifurcation analysis, and simulation of material separation using element elimination techniques. All three components are covered in three separate sections.

Chapter 4: Implementation of Algorithms

Chapter 4 describes the algorithm associated with the multiscale fracture simulation that is proposed in this study. Also, details of implementing of the proposed algorithm into a finite element code is discussed in this chapter.

Chapter 5: Example Problems

Verification and example problems are presented in Chapter 5. Certain example problems are solved in this chapter in order to represent accurate implementation of the proposed algorithm, to prove the hypothesis, and to evaluate the capability of this approach.

Chapter 6: Conclusions and Recommendations

The final chapter presents conclusions of this research, draws upon the proposed approach, addresses current limitations, and identifies potential future research topics.

Chapter 2

Literature Review

This chapter provides a literature review of studies that used numerical methods that included material heterogeneity to predict crack propagation. Along with the current understanding of the problem, research gaps are also presented in this chapter.

2.1 Introduction

Many researchers have studied the effect of material heterogeneity on microscopic damage evolution and material failure at macroscopic scale. In an early study, Andersson (1977) investigated crack propagation by placing a special cell containing only a single void along a crack path. This cell represented a simplified version of microscopic heterogeneity of a material. Crack propagation was simulated by analyzing the void growth of the cell ahead of the crack tip [Andersson, 1977]. This is similar to the void growth model that was initially introduced by Rice (1969) [Rice and Tracey, 1969, Mishnaevsky Jr et al., 1998] and was extended for simulation of ductile fracture by Xia (1995) [Xia and Shih, 1995a, Xia and Shih, 1995b, Xia and

Shih, 1996, Xia et al., 1995]. The general concept of this approach is explained well in [Broberg, 1997]. Broberg showed that crack growth can be modeled by analyzing a cell of a material where "The cell is regarded as the smallest material unit that contains reasonably sufficient information about crack growth in the material".

Over the past two decades, a number of researchers have sought to predict crack propagation at the macroscopic level using multiscale methods. Multiscale methods are built upon micromechanics and are able to include sufficient details of material heterogeneity for analyzing its behavior. In this approach, a heterogeneous material is treated as a homogeneous material with effective properties. The effective properties are obtained by analyzing a Representative Volume Element (RVE). The RVE should include sufficient details of the microstructure of the material. The effective properties of an RVE are calculated using the Homogenization methods [Nemat-Nasser and Hori, 2013, Hill, 1972]. In the absence of damage in an RVE – which means the RVE is not evolving over time – the homogenized properties are obtained only once for a given RVE. Such methods are generally known as Upscaling or Hierarchical methods in the literature (Figure 2.1).

In contrast, when the RVE is evolving, the homogenization process needs to be completed recursively over time to be able to capture potential progressive damage within an RVE. This concept, which is known as the Two-way linked multiscale, FE^2, or Semi-concurrent approach, is well integrated with numerical methods such as the Finite Element Method (FEM) and the Extended Finite Element Method (XFEM) [Feyel and Chaboche, 2000, Massart et al., 2007, Ozdemir et al., 2008, Geers et al., 2010, Belytschko and Song, 2010, Verhoosel et al., 2010b, Souza and Allen, 2010, Nguyen et al., 2011, Kim et al., 2013, Toro et al., 2016]. The process of the two-way linked multiscale approach is presented in Figure 2.2. In this approach, the

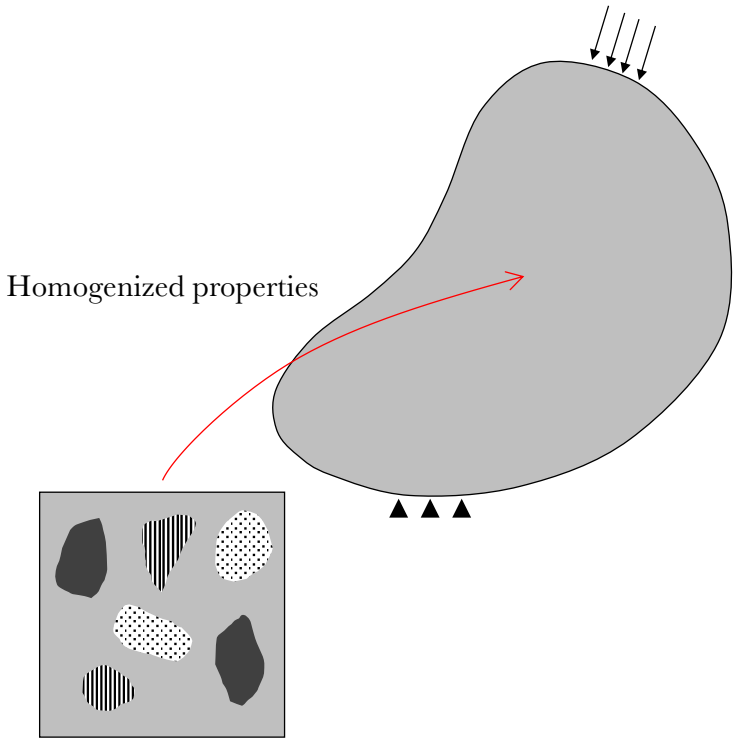

Figure 2.1: Upscaling method diagram.

macroscale and microscale models are analyzed separately. As shown in Figure 2.2, this method consists of three major steps that are completed at each time step.

1. The macroscopic scale is solved in order to obtain the stress and strain field within the heterogeneous object. The current state of stress or strain at a material point is applied to the RVE in the form of far field boundary condition.

2. The RVE is solved under the applied boundary condition in order to obtain the response of the RVE. The effective constitutive properties are calculated based on homogenization method from the response of the RVE. The homogenization method takes into account microdamage of the RVE.

3. The homogenized constitutive properties are used to update the properties of the material for the next time step.

As long as microcracks are distributed evenly over the RVE, it can be treated as stiffness reduction in the homogenized tangent stiffness matrix. However, microdamage can grow unevenly and form a localized band within the RVE, which can be regarded as localization of RVE. Localization of RVE has two major consequences that violate the basic assumptions of standard homogenization.

- The homogenization theory assumes that the RVE is statistically representative of the material. However, localized RVE violates this assumption [Kouznetsova et al., 2002, Gitman et al., 2007]. When strain localization occurs within an RVE, the localized area does not scale with the size of the RVE; thus, the homogenized properties that are calculated using standard homogenization theories change with respect to RVE size.

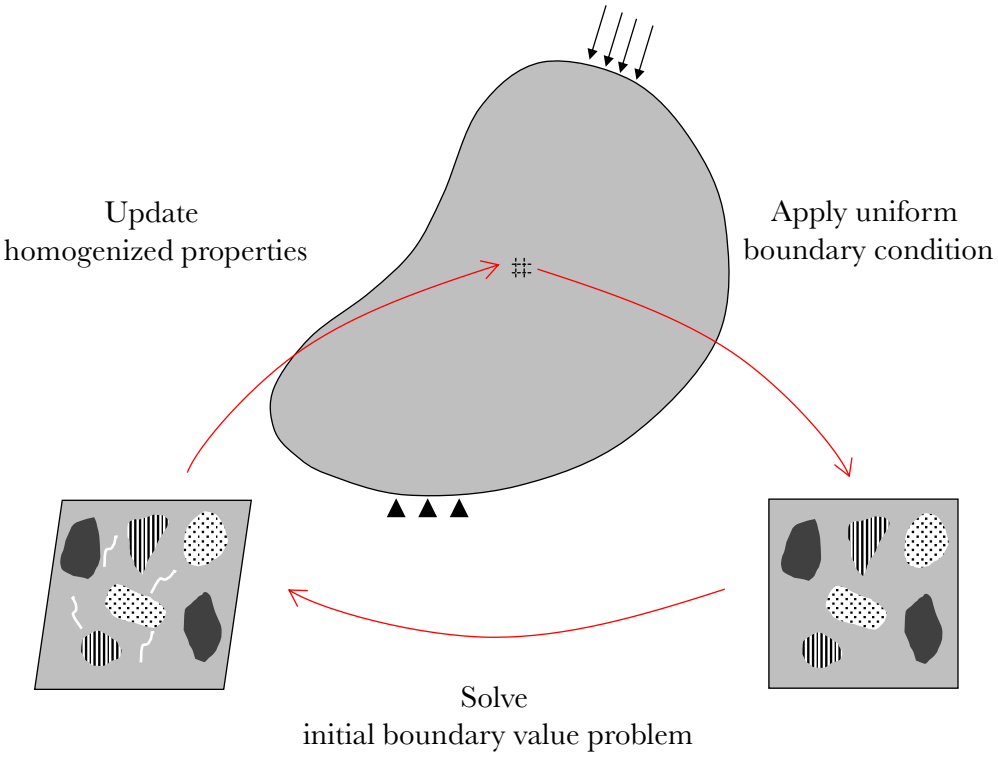

Figure 2.2: Two-way linked multiscale method diagram.

- It is assumed that RVE represents a material point that experiences continuous stress and strain fields [Inglis et al., 2008]. However, when localization occurs in an RVE, this assumption is not valid.

The next section gives a brief overview of the recent works that address these issues.

2.2 Relevant Studies

Verhoosel et al. [Verhoosel et al., 2010b] have proposed an averaging scheme that provides traction-separation relation for evolution of macroscopic cohesive and adhesive fraction based on FE^2 method. This study extended the work done by Verhoosel et al. in [Verhoosel et al., 2010a]. They applied the averaging process on microscale models representing the bulk material and the adhesive layer in order to obtain the traction-separation relation in the vicinity of a crack tip, as shown in Figure 2.3. In addition, Figure 2.4 shows the schematic view of the microscale model. They have considered different fracture models for adhesive and cohesive failure processes on the microscale. Homogenized constitutive behavior of macroscale, before when the failure criterion is met, is obtained using the volume averages of the microscopic quantities. But in order to calculate homogenized cohesive interface traction-separation behavior, the projection of microscale Cauchy stress on the macroscopic crack plane is used.

Neguyen et al. (2010) has implemented a multiscale approach for modeling crack in heterogeneous material [Nguyen et al., 2010, Nguyen et al., 2011, Nguyen et al., 2012a, Nguyen et al., 2012b, Nguyen et al., 2012c]. They replaced a heterogeneous body undergoing a localized failure with a macro-scale homogenized body with a discrete cohesive crack and a meso-scale model with a localized band of diffuse damage,

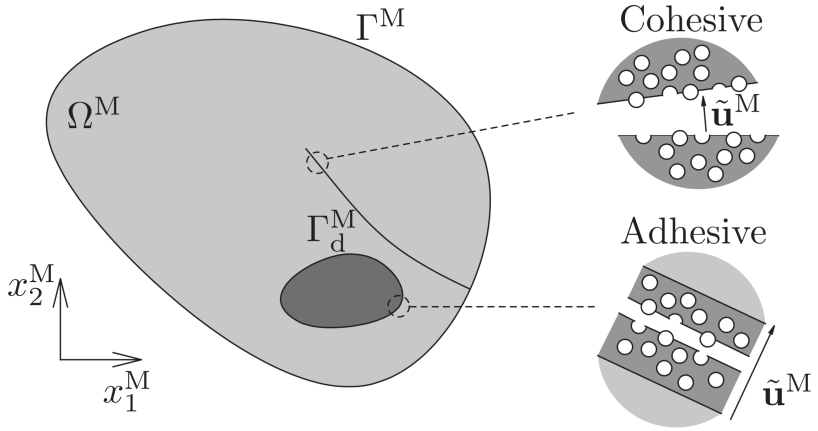

Figure 2.3: Schematic representation of the macroscale model [Verhoosel et al., 2010b].

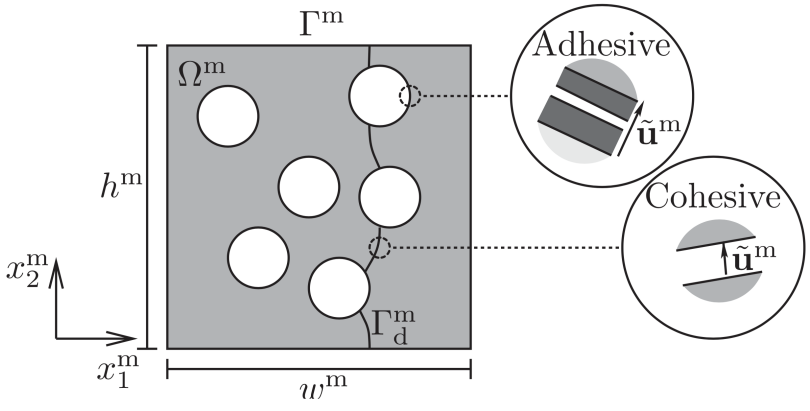

Figure 2.4: Schematic representation of the microscale model [Verhoosel et al., 2010b].

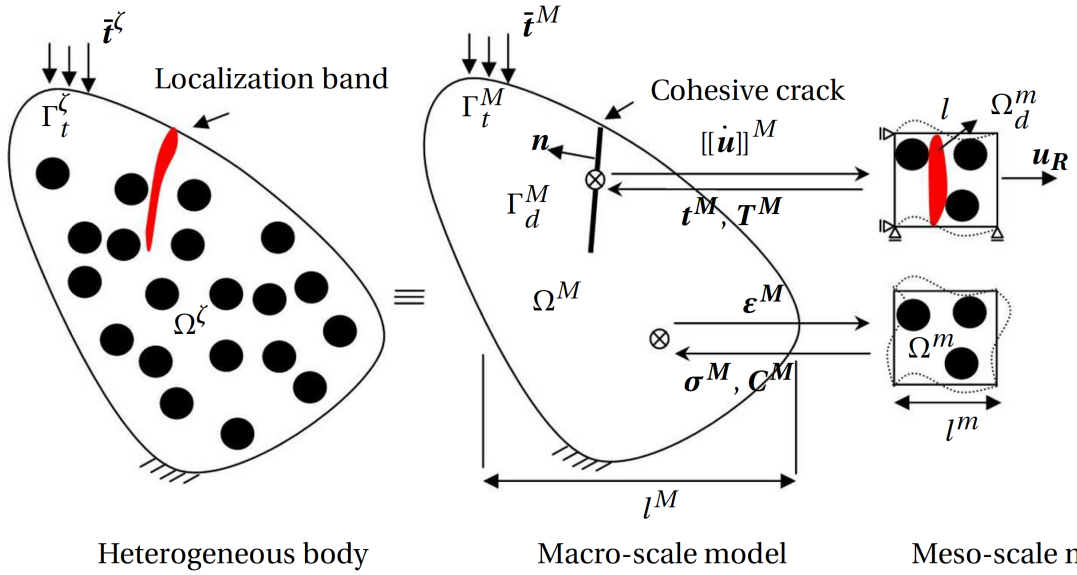

Figure 2.5: The multiscale scheme proposed by Neguyen et al. [Nguyen et al., 2012c].

as shown in Figure 2.5. The cohesive crack at macro-scale is simulated using XFEM. The continuous-discontinuous computational homogenization is used to determine cohesive law for the cohesive macro-crack. In this method the homogenized stiffness of bulk elements near to a macro-crack is obtained from unloading of the localized RVE. In addition, an RVE with the boundary condition shown in Figure 2.5 is used to obtain homogenized cohesive behavior on the macro-crack surface while the averaging process is done over the active damaged zone, Ω_d^m. This approach was later extended by Karamnejad et al. for problems under impact loading [Karamnejad and Sluys, 2014, Karamnejad and Sluys, 2015, Karamnejad, 2016, Karamnejad et al., 2017].

Belytschko et al. (2007) proposed a multiscale method, *Multiscale Aggregating Discontinuities* (MAD), as shown in Figure 2.6, to simulate fracture of heterogeneous materials [Loehnert and Belytschko, 2007, Belytschko et al., 2008, Belytschko and Song, 2010, Song and Belytschko, 2009]. In this approach, the problem is decomposed into two scales: fine scale and coarse scale. The XFEM is utilized to simulate strong

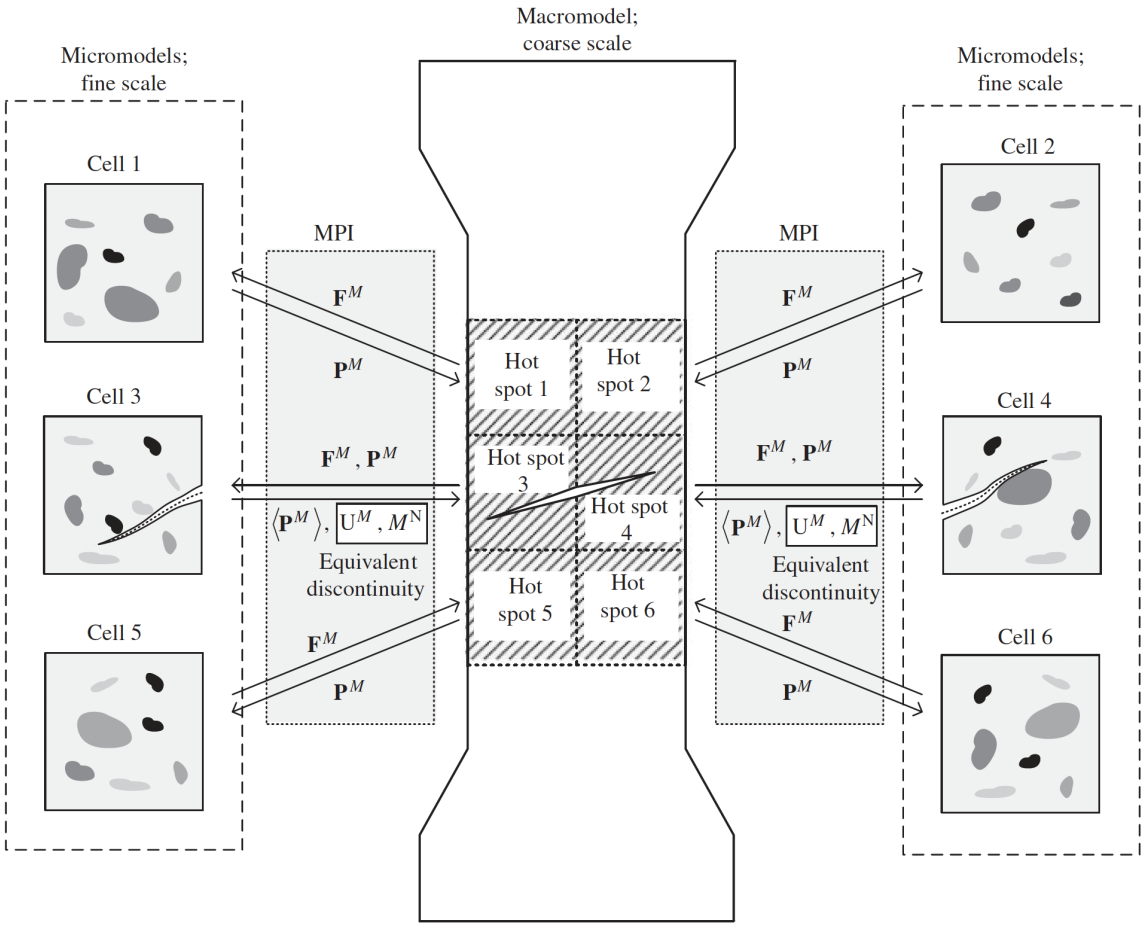

Figure 2.6: Schematic of macro–micro linkages of the MAD method [Belytschko and Song, 2010].

discontinuity in both scales. When a fine scale model loses its strict ellipticity a coarse-grained discontinuity is inserted to the macroscale model. The strict ellipticity is defined based on the tangent matrix which relates the deformation gradient and first Piola–Kirchhoff stress. The averaging quantities of localized fine scale model is obtained from a "perforated" unit cell from which subdomains that are unstable (where the material loses strict ellipticity, i.e. the areas of material that include cracks) are excluded.

Oliver et al. [Oliver et al., 2014, Oliver et al., 2015] have formulated and simulated

material failure in a multiscale framework. Fracture in larger length scale is simulated by a Continuum Strong Discontinuity Approach, introduced earlier by Oliver [Oliver, 1995]. The points of strain localization band are linked to a conventional RVE-like cell, which is called failure-cell. The failure-cell is equipped with cohesive-bands with a predefined position to capture damage in RVE. It is claimed that the failure-cell does not need to be statistically representative of the material, however standard homogenization procedures are applied to it. Strain-localization band width is determined from size of failure-cell and the amount of activated failure mechanisms in failure-cell.

Toro and coworkers [Toro et al., 2014, Toro et al., 2016] have extended a multiscale failure method, which was initially developed by Sanchez et al. [Sanchez et al., 2013] and named the method as the *Failure-Oriented Multiscale Formulation* (FOMF). They tried to address the aforementioned issues regarding localization of RVE. They introduced a failure mechanism in the larger length scale based on cohesive interface model. The phenomenological model of cohesive interface is characterized through homogenization of the RVE. They have proposed a homogenization method which gives cohesive interface traction-separation relation from adopted RVE, while it is objective with respect to the size of the RVE.

Souza and Allen employed two-way linked multiscale approach to simulate so-called macrocracks as the result of accumulation of microcracks, as shown in Figure 2.7 [Souza and Allen, 2011]. In this approach, microcracks are simulated within RVE using the *Cohesive Zone Model* (CZM). When density of microcracks in an RVE meets a certain criteria, an equivalent to RVE localization, a cohesive element with a proper direction will be inserted to the larger length scale problem such that it follows the XFEM formulation (Figure 2.8). This cohesive element is then linked to

an RVE which is cloned from the localized RVE. As loading continues, microcracks in cloned RVE coalesces until the RVE completely fails and thereby the cohesive element breaks into two traction-free surfaces.

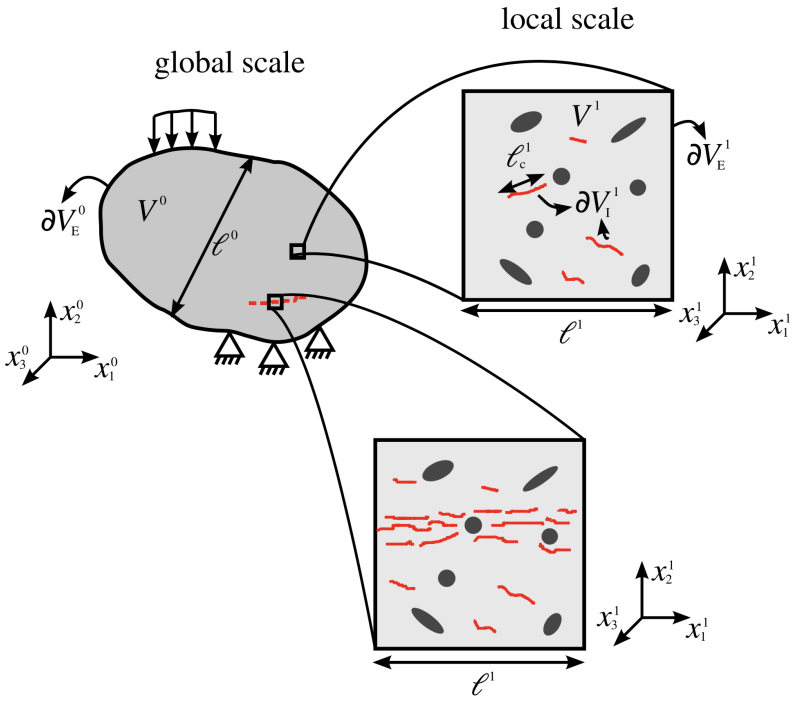

Figure 2.7: Schematic representation of a two-scale IBVP [Souza and Allen, 2010].

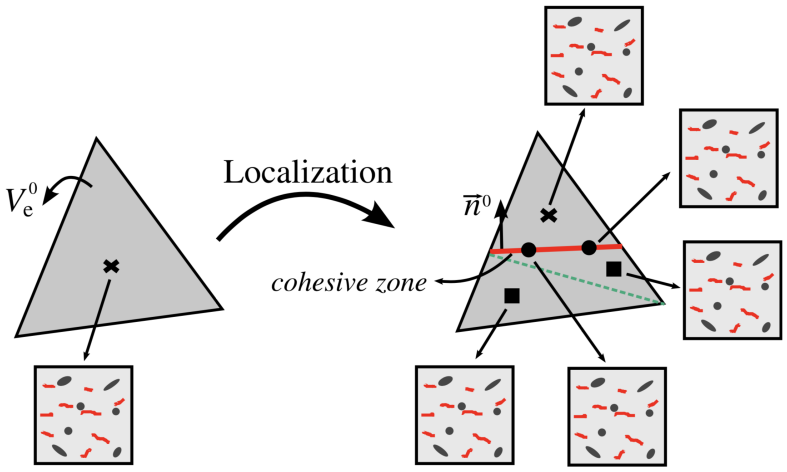

Figure 2.8: Cohesive zone insertion at global-scale elements [Souza and Allen, 2010].

Chapter 3

Theory and Background

The proposed method in this dissertation is built on three major components:

- Two-way linked multiscale modeling
- Bifurcation analysis
- Element elimination method

This chapter gives the theoretical background of each component in three separate sections.

3.1 Core Part No. 1: Two-way Linked Multiscale Modeling

The two-way linked multiscale approach is entirely based on the postulate of statistical homogeneity of a composite. It means that the geometrical microstructure of the material can be expressed as an assembly of finite unit cells as shown in Figure 3.1. This cell, also called as Representative Volume Element (RVE), must be sufficiently

large to describe the overall properties of the composite [Hill, 1972, Qin and Yang, 2008]. This postulate implies that the overall effective properties of a composite is equal to the volume average of those properties over an RVE of that composite. The correct application of multiscale concept requires the following assumptions:

- The composite must be statistically homogeneous. A strict definition of a statistically homogeneous media is presented in terms of n-point probabilities and ensemble averages, which indicates that probability of finding a phase at a point is independent of the point's location [Hori and Nemat-Nasser, 1999, Beran, 1965, Kroner, 1972].

- A definable RVE must exist and fully represent the characteristics of the heterogeneous material. The efficient size of the RVE can be found by monitoring the RVE's response versus its size. The minimum RVE size at which the effective property converges to a constant value is sufficient to define the RVE [Gitman et al., 2007].

- Characteristic length of a statistically homogenous object (L) and corresponding RVE (l) must be widely separated [Hill, 1972].

Using this approach, a composite material can be simulated by dividing the problem into two separate length scales: *global-scale* or *macro-scale* and *local-scale* or *micro-scale*. The global-scale model defines the geometry of the heterogeneous body. The local-scale model is defined by a *Representative Volume Element* (RVE) that describes the microstructure of the composite. It is assumed that an RVE ideally represents a point at the global-scale model. Hence, the overall behavior of RVE is assumed to be equivalent to the behavior of the composite at the corresponding

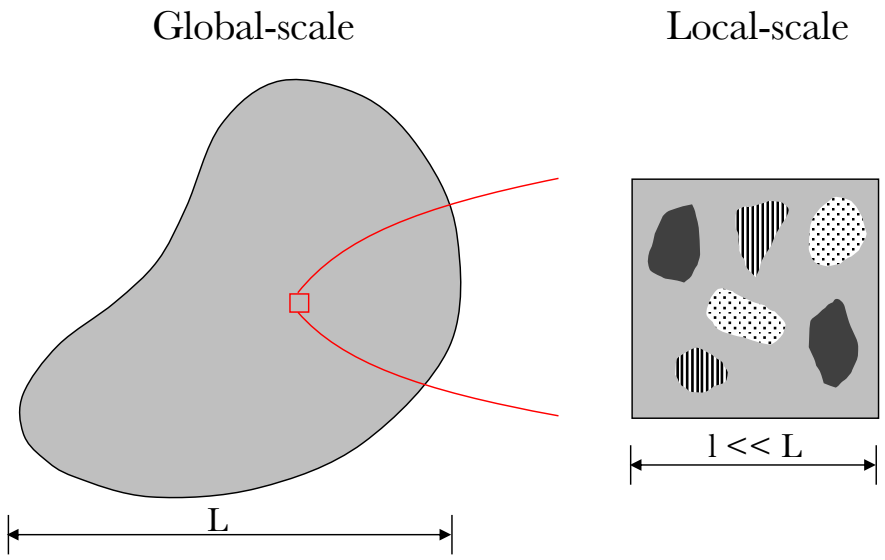

Figure 3.1: Schematic view of a heterogeneous body and its representative volume element.

neighboring material. Hence, the effective (average) constitutive behavior of the composite at the global-scale model is defined as the relation between the average of field variables, i.e. stress and strain, over the RVE.

3.1.1 Homogeneous Boundary Conditions

The state variables can be determined by solving an initial boundary value problem (IBVP) for the RVE, while it is subjected to a homogeneous boundary condition which can be applied as either traction $\hat{T}_i$ or displacement $\hat{U}_i$ boundary conditions [Souza et al., 2008, Souza and Allen, 2010, Kim et al., 2013]. The traction or displacement boundary conditions are calculated based on the stress or strain values at the corresponding location on the global-scale model. The boundary condition applied to the RVE must be homogeneous in order to expect statistically homogeneous field variables. Equation 3.1 and Equation 3.2 are used to obtain the homogeneous

traction and displacement boundary condition respectively [Hashin, 1983].

$$\hat{T}_i = \sigma_{ij}^G n_j \qquad \text{on } S_E^L \tag{3.1}$$

$$\hat{U}_i = \epsilon_{ij}^G x_j \qquad \text{on } S_E^L \tag{3.2}$$

where σ_{ij}^G and ϵ_{ij}^G are the constant stress and constant strain of a point at the global-scale model; $\hat{T}_i$ and $\hat{U}_i$ are the traction and displacement boundary conditions acting on the RVE's external boundary (S_E^L). Throughout this dissertation, the superscripts G and L will be used to indicate global-scale and local-scale models respectively.

In the multiscale method, any stiffness reduction due to damage accumulation in the RVE is reflected as a stiffness reduction in the effective tangent constitutive tensor. Therefore, when there is progressive damage or microstructural change in the local-scale model, the multiscale framework should be formulated in a two-way linked and incremental form, as shown in Figure 3.2. Therefore, in a two-way multiscale approach at each time step:

- The boundary conditions of RVE are updated according to the strain or stress state at the global-scale model (global-scale to local-scale linking).
- The effective properties of the global-scale model are updated according to the current response of the RVE (local-scale to global-scale linking).

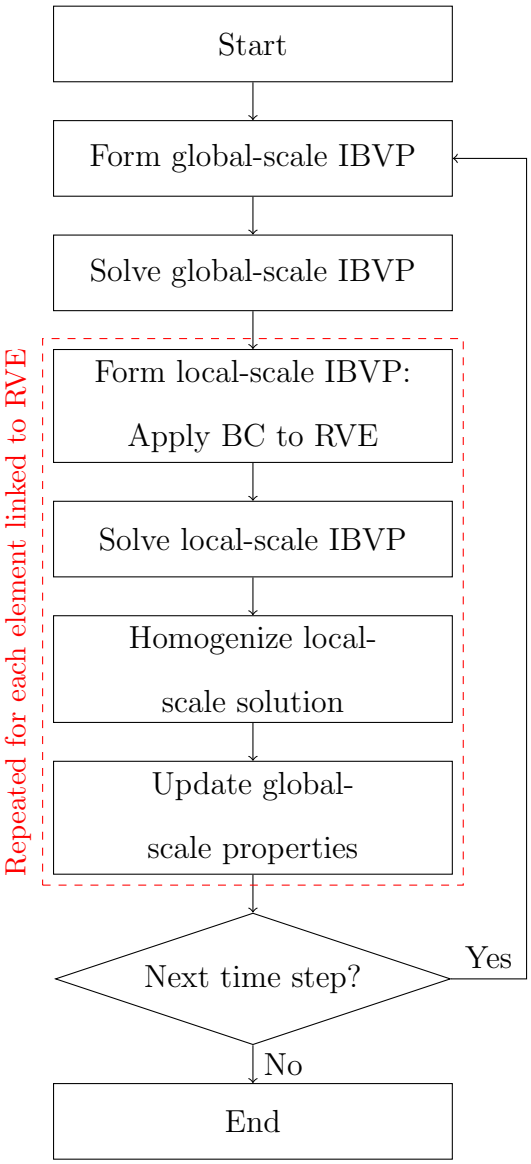

Figure 3.2: Algorithm of two-way linked multiscale method.

3.1.2 Homogenization

The two-way linked multiscale method is implemented in a recursive scheme, in which the global-scale strain or stress tensor is used to calculate the RVE's displacement or traction boundary condition. Also the stiffness tangent tensor in the global-scale

model is equivalent to the effective stiffness tensor obtained from solving the IBVP of the RVE. The effective stiffness tensor is defined as the relationship between the homogenized stress and strain field over an RVE.

$$\bar{\sigma}_{ij}^{L} = C_{ijkl}^{*} \bar{\epsilon}_{kl}^{L} \tag{3.3}$$

$$\bar{\epsilon}_{ij}^{L} = S_{ijkl}^{*} \bar{\sigma}_{kl}^{L} \tag{3.4}$$

Since the heterogeneous material is assumed to be statistically homogeneous, the volume averaging method is applicable to homogenize the field variables over the RVE.

$$\Delta\epsilon_{ij}^{G} = \Delta\bar{\epsilon}_{ij}^{L} = \frac{1}{V^{L}} \int_{V^{L}} \Delta\epsilon_{ij}^{L} dV \tag{3.5}$$

$$\Delta\sigma_{ij}^{G} = \Delta\bar{\sigma}_{ij}^{L} = \frac{1}{V^{L}} \int_{V^{L}} \Delta\sigma_{ij}^{L} dV \tag{3.6}$$

where $\bar{\sigma}_{ij}^{L}$ and $\bar{\epsilon}_{ij}^{L}$ are the volume average of the stress and strain tensor over the RVE, respectively. Using the divergence theorem, Equation 3.5 and 3.6 can be rewritten as follows:

$$\Delta\epsilon_{ij}^{G} = \Delta\bar{E}_{ij}^{L} + \Delta\bar{e}_{ij}^{L} \tag{3.7}$$

where

$$\Delta\bar{E}_{ij}^{L} = \frac{1}{V^{L}} \int_{S_{E}^{L}} \frac{1}{2} \big(\Delta u_{i}^{L} n_{j}^{L} + \Delta u_{j}^{L} n_{i}^{L} \big) dS \tag{3.8a}$$

$$\Delta\bar{e}_{ij}^{L} = \frac{1}{V^{L}} \int_{S_{I}^{L}} \frac{1}{2} \big(\Delta u_{i}^{L} n_{j}^{L} + \Delta u_{j}^{L} n_{i}^{L} \big) dS \tag{3.8b}$$

and

$$\begin{aligned}\Delta\sigma_{ij}^{G} &= \Delta\bar{\sigma}_{ij}^{L} \\ &= \frac{1}{V^{L}}\int_{S_{E}^{L}} \Delta\sigma_{ij}^{L} n_{k}^{L} x_{j}^{L} dS\end{aligned} \tag{3.9}$$

where $\bar{E}_{ij}^{L}$ and $\bar{e}_{ij}^{L}$ are the volume averaged strain over the external (S_{E}^{L}) and internal (S_{I}^{L}) boundaries over the RVE, respectively. n_{i}^{L} is the outward unit normal vector to the external and internal boundaries.

It is worth to mention that the internal boundaries are due to developing microcracks (free surfaces) inside the RVE, which implies the averaged measure of damage. Also, regarding Equation 3.9, the volume averaged stress is equal to the external boundary averaged traction vectors only if the sum of traction vectors over the internal boundary surfaces is zero [Souza et al., 2008].

3.1.3 Governing Equations

Global-scale IBVP

Consider the global-scale problem as a general body with an interior V^{G} and a boundary S^{G}, as shown in Figure 3.3, in the absence of body forces and inertial effects. Hence, the mechanical IBVP is defined by a set of governing equations, boundary conditions, and initial condition:

- Conservation of linear momentum
- Conservation of angular momentum
- Strain-displacement relations for small strain condition
- Constitutive equation

$$\sigma^G_{ji,j} = 0 \qquad \text{in } V^G \tag{3.10}$$

$$\sigma^G_{ij} = \sigma^G_{ji} \qquad \text{in } V^G \text{ and on } S^G \tag{3.11}$$

$$\epsilon^G_{ij} = \frac{1}{2}\left(u^G_{i,j} + u^G_{j,i}\right) \qquad \text{in } V^G \tag{3.12}$$

$$\sigma^G_{ij}(t) = \Omega^{\tau=t}_{\tau=-\infty}\left\{\epsilon^G_{kl}(\tau)\right\} \qquad \text{in } V^G \tag{3.13}$$

where σ_{ij}, ϵ_{ij}, and u_i are the Cauchy stress tensor, infinitesimal strain tensor, and displacement vector, respectively; $\Omega^{\tau=t}_{\tau=-\infty}$ represents a history-dependent constitutive behavior.

The initial values for all the state variables are assumed to be zero.

$$\sigma_{ij}(t=0) = 0 \qquad \text{in } V^G \text{ and on } S^G \tag{3.14}$$

$$\epsilon_{ij}(t=0) = 0 \qquad \text{in } V^G \text{ and on } S^G \tag{3.15}$$

$$u_i(t=0) = 0 \qquad \text{in } V^G \text{ and on } S^G \tag{3.16}$$

Also, both displacements and tractions are specified on the body as follows:

$$u_i(t) = \hat{U}_i \qquad \text{on } S^G_{E_u} \tag{3.17}$$

$$t_i(t) = \sigma_{ij}\, n_j = \hat{T}_i \qquad \text{on } S^G_{E_t} \tag{3.18}$$

where $\hat{U}_i$ and $\hat{T}_i$ are known boundary displacements and boundary tractions, respectively; $S^G_{E_u}$ and $S^G_{E_t}$ are subdivisions of S^G_E such that $S^G_{E_u} \cup S^G_{E_t} = S^G_E$ and $S^G_{E_u} \cap S^G_{E_t} = \varnothing$.

Local-scale IBVP

As mentioned earlier, the global-scale's effective constitutive properties are derived from the response of a local-scale RVE. The effective properties can be calculated by averaging the local-scale state variables, stresses and strains, which are obtained from

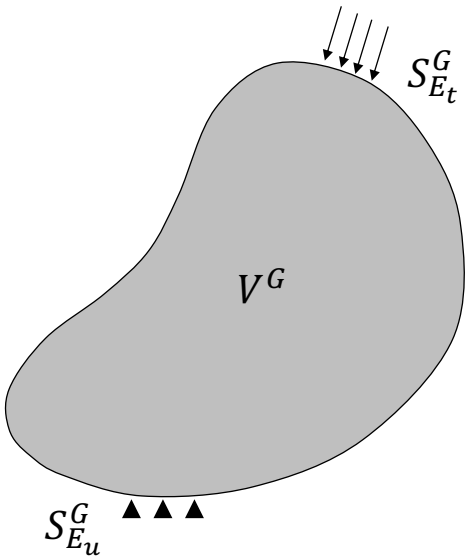

Figure 3.3: Global-scale initial boundary value problem.

solving the local-scale IBVP under homogenous displacement or traction boundary condition. For each RVE, the homogeneous boundary condition is linked to the state variables of the corresponding location in the global-scale model.

Let's consider the local-scale body as a general body containing discrete cracks and cohesive zones as shown in Figure 3.4. This body has an interior V^L and a boundary S^L which consists of three parts: S^L_I which denotes the boundary of discrete cracks; S^L_C which denotes the boundary of cohesive zones; and S^L_E which denotes the external boundary of the local-scale body. Similar to the global-scale model, the IBVP at the local-scale model is defined by the following governing equations:

$$\sigma^L_{ji,j} = 0 \qquad \text{in } V^L \tag{3.19}$$

$$\sigma^L_{ij} = \sigma^L_{ji} \qquad \text{in } V^L \text{ and on } S^L \tag{3.20}$$

$$\epsilon^L_{ij} = \frac{1}{2}\left(u^L_{i,j} + u^L_{j,i}\right) \qquad \text{in } V^L \tag{3.21}$$

$$\sigma^L_{ij}(t) = \Omega^{\tau=t}_{\tau=-\infty}\left\{\epsilon^L_{kl}(\tau)\right\} \qquad \text{in } V^L \tag{3.22}$$

where all variables used here are the same as those used in the global-scale model, except the superscript L which represents the local-scale model.

The behavior ahead of a crack tip is expressed by the general traction–displacement relationship:

$$T^L_i(t) = \mathcal{T}^{\tau=t}_{\tau=-\infty}\{\delta u_k(\tau)\} \qquad \text{on } S^L_C \tag{3.23}$$

where $\mathcal{T}^{\tau=t}_{\tau=-\infty}$ represents a history-dependent cohesive zone model traction–separation relationship.

The initial values and boundary conditions are also specified as follows:

$$\sigma_{ij}(t=0) = 0 \qquad \text{in } V^L \text{ and on } S^L \tag{3.24}$$

$$\epsilon_{ij}(t=0) = 0 \qquad \text{in } V^L \text{ and on } S^L \tag{3.25}$$

$$u_i(t=0) = 0 \qquad \text{in } V^L \text{ and on } S^L \tag{3.26}$$

$$u_i(t) = \hat{U}_i \qquad \text{on } S^L_{E_u} \tag{3.27}$$

$$t_i(t) = \hat{T}_i \qquad \text{on } S^L_{E_t} \tag{3.28}$$

where the superscript L represents the local-scale model.

)

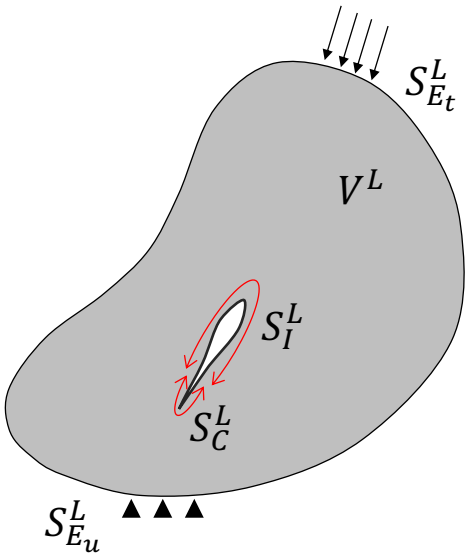

Figure 3.4: Local-scale initial boundary value problem.

3.1.4 Constitutive Equations

Elastic Constitutive Equation

The general elastic constitutive relationship, which is not time dependent, is given by:

$$\sigma_{ij}(t) = C^E_{ijkl}\,\epsilon_{kl}(t) \qquad \text{in } V \tag{3.29}$$

where C^E_{ijkl} is the fourth order elastic modulus tensor.

For isotropic materials, Equation 3.29 can be rewritten as the following form:

$$\sigma_{ij}(t) = \frac{E\nu}{(1+\nu)(1-2\nu)}\delta_{ij}\,\epsilon_{kk}(t) + \frac{E}{(1+\nu)}\epsilon_{ij}(t) \qquad \text{in } V \tag{3.30}$$

where E and ν are elastic modulus and Poisson's ratio; δ_{ij} is Kronecker delta.

Viscoelastic Constitutive Equation

The constitutive equation is given for a general anisotropic and linear viscoelastic material in the convolution integral form [Christensen, 2012]:

$$\sigma_{ij}(t) = \int_0^t C_{ijkl}(t-\tau)\frac{\partial \epsilon_{kl}(\tau)}{\partial \tau}d\tau \qquad \text{in } V \tag{3.31}$$

where $C_{ijkl}(t-\tau)$ is the fourth order tensor of relaxation modulus; t is the time of interest, while τ is the time-history integration variable.

Equation 3.31 can be rewritten for isotropic material, with a time-independent Poisson's ratio, by the following:

$$\begin{aligned}\sigma_{ij}(t) =& \frac{\nu}{(1+\nu)(1-2\nu)}\int_0^t E(t-\tau)\delta_{ij}\frac{\partial \epsilon_{kk}(\tau)}{\partial \tau}d\tau \\ &+ \frac{1}{(1+\nu)}\int_0^t E(t-\tau)\frac{\partial \epsilon_{ij}(\tau)}{\partial \tau}d\tau\end{aligned} \qquad \text{in } V \tag{3.32}$$

where $E(t)$ and ν are viscoelastic stress relaxation modulus and time-independent Poisson's ratio.

Viscoelastic Cohesive Zone Constitutive Equation

Evolving damage is taken into account by allowing for microcrack growth at the local-scale. Crack initiation and propagation are modeled using a viscoelastic cohesive zone model, in which the traction–separation relation is defined by Allen and Searcy [Allen and Searcy, 2000]:

$$T_i(t) = \frac{1}{\delta_i}\frac{u_i(t)}{\lambda(t)}\big(1-\alpha(t)\big)\left(\sigma_i^f + \int_0^t E^C(t-\tau)\frac{\partial \lambda(\tau)}{\partial \tau}\,d\tau\right) \qquad \text{in } \partial V_I^L \tag{3.33}$$

where i represents the local direction, normal n or tangential t (there is no summation over the index i); $T_i(t)$ and $u_i(t)$ are the cohesive zone traction and displacement,

respectively; δ_i is the empirical material length parameter; $\alpha(t)$ is the internal damage parameter; σ_i^f is the state of stress in the vicinity of crack tip upon the initiation of damage; $E^C(t-\tau)$ is the uniaxial relaxation modulus of the cohesive zone; $\lambda(t)$ is the normalized cohesive zone opening displacement such that

$$\lambda(t) = \sqrt{\left(\frac{u_n}{\delta_n}\right)^2 + \left(\frac{u_t}{\delta_t}\right)^2} \tag{3.34}$$

The material length parameters δ_n and δ_t can be determined by equating the total work of separation dissipated by the cohesive zone to the energy released during crack growth experiments.

A power law function can be used to represent the internal damage parameter, such as [Allen and Searcy, 2000]:

$$\dot{\alpha}(t) = \begin{cases} A\lambda(t)^m, & \dot{\lambda} \geq 0 \text{ and } \alpha < 1 \\ 0, & \dot{\lambda} \leq 0 \text{ or } \alpha = 1 \end{cases} \tag{3.35}$$

where A and m are material parameters; the dot indicates time derivatives.

3.1.5 Time Incrementalization of the Constitutive Equations

The process of obtaining numerical solutions of problems involving time- or history-dependent constitutive equations are usually given in an incremental form. This section includes the incremental formulation of the viscoelastic constitutive equation, Equation 3.31, and cohesive zone traction–displacement law, Equation 3.33.

Viscoelastic Constitutive Equation

The incremental formulation of linear viscoelastic stress–strain relationship, Equation 3.31, is presented here. The objective is to derive a method of expressing stresses at time $t + \Delta t$ in terms of stresses and strains at time t. The incrementalization process summarized here was developed by Zocher et al. [Zocher et al., 1997]. First, let's define the following variables in the incremental forms:

$$\Delta\epsilon_{ij} \equiv \epsilon_{ij}(t + \Delta t) - \epsilon_{ij}(t) \tag{3.36}$$

$$\Delta\sigma_{ij} \equiv \sigma_{ij}(t + \Delta t) - \sigma_{ij}(t) \tag{3.37}$$

$$\Delta C_{ijkl} \equiv C_{ijkl}(t + \Delta t) - C_{ijkl}(t) \tag{3.38}$$

Also, it is assumed $\epsilon_{ij}(t)$ can be approximated by a linear function over each interval $t \leq \tau \leq t + \Delta t$. So:

$$\epsilon_{kl}(\tau) = \epsilon_{kl}(t) + R_{\epsilon}(\tau - t)\, H(\tau - t) \tag{3.39}$$

where is R_{ϵ} a constant representing the strain rate over the interval; $H(\tau - t)$ is Heaviside step function.

Therefore, the following expression is valid.

$$\frac{\partial\epsilon_{kl}(\tau)}{\partial\tau} \approx R_{\epsilon} \equiv \frac{\Delta\epsilon_{kl}}{\Delta t} \tag{3.40}$$

Also, suppose that each element of C_{ijkl} can be represented by the Wiechert model in form of Prony series:

$$C_{ijkl}(t) = C_{ijkl_{\infty}} + \sum_{m=1}^{M_{ijkl}} C_{ijkl_m} e^{-\frac{C_{ijkl}}{\eta_{ijkl}}t} \tag{3.41}$$

Therefore, the incremental form of viscoelastic constitutive equation can be written as follows:

$$\Delta\sigma_{ij} = C'_{ijkl}\,\Delta\epsilon_{kl} + \Delta\sigma^R_{ij} \tag{3.42}$$

where C'_{ijkl} is given by:

$$C'_{ijkl} = C_{ijkl_\infty} + \frac{1}{\Delta t}\sum_{m=1}^{M_{ijkl}} \eta_{ijkl_m}\left(1 - e^{-\frac{C_{ijkl}}{\eta_{ijkl}}\Delta t}\right) \tag{3.43}$$

and $\Delta\sigma^R_{ij}$ is given by

$$\Delta\sigma^R_{ij} = -\sum_{k=1}^{3}\sum_{l=1}^{3} A_{ijkl} \tag{3.44}$$

where

$$A_{ijkl} = \sum_{m=1}^{M_{ijkl}}\left(1 - e^{-\frac{C_{ijkl}}{\eta_{ijkl}}\Delta t}\right) S_{ijkl_m}(t) \tag{3.45}$$

and

$$S_{ijkl_m}(t) = e^{-\frac{C_{ijkl}}{\eta_{ijkl}}\Delta t} S_{ijkl_m}(t-\Delta t) + \eta_{ijkl_m} R_\epsilon\left(1 - e^{-\frac{C_{ijkl}}{\eta_{ijkl}}\Delta t}\right) \tag{3.46}$$

Note that there is no sum over i, j, k and l.

Viscoelastic Cohesive Zone Constitutive Equation

This section represents an incremental form of the viscoelastic cohesive zone traction–separation relationship, Equation 3.33. The goal is to express the traction at time $t+\Delta t$ in terms of the properties at time t. This is done by Allen and Searcy (2000) and it is summarized here [Allen and Searcy, 2000, Searcy, 1998]. To derive an expression

for the increment in the cohesive traction, ΔT_i, the following incremental variables are defined:

$$T_i(t+\Delta t) \equiv T_i(t) + \Delta T_i \tag{3.47}$$

$$u_i(t+\Delta t) \equiv u_i(t) + \Delta u_i \tag{3.48}$$

$$\lambda_i(t+\Delta t) \equiv \lambda_i(t) + \Delta \lambda_i \tag{3.49}$$

$$\alpha(t+\Delta t) \equiv \alpha(t) + \Delta \alpha \tag{3.50}$$

$$E_i^C(t+\Delta t) \equiv E_i^C(t) + \Delta E_i^C \tag{3.51}$$

Also, suppose a linear variation can represent the displacement function over the interval $t \leq \tau \leq t + \Delta t$, which is defined by:

$$\lambda(\tau) = \lambda(t) + R_\lambda(\tau - t)\, H(\tau - t) \tag{3.52}$$

so,

$$\frac{\partial \lambda}{\partial \tau} = R_\lambda \equiv \frac{\Delta \lambda}{\Delta t} \tag{3.53}$$

Also, it is assumed that:

$$\frac{u_i(t+\Delta t)}{\lambda(t+\Delta t)} \approx \frac{u_i(t)}{\lambda(t)} \tag{3.54}$$

and

$$\frac{\partial \lambda}{\partial u_i}\Big|_t \approx \frac{1}{\delta_i} \tag{3.55}$$

Furthermore, when small time steps are taken, the increment in the damage is

given by:

$$\Delta\alpha = \dot{\alpha}(t)\,\Delta t \tag{3.56}$$

where $\dot{\alpha}(t)$ is known at time t.

Now, suppose the following Prony series specifies the constitution for the cohesive zone:

$$E^C(t) = E_\infty + \sum_{j=1}^{P} E_j e^{-\frac{E_j}{\eta_j}t} \tag{3.57}$$

Finally, the resulting recursive traction for the viscoelastic cohesive zone can be written as follows:

$$\Delta T_i = K_i\,\Delta u_i + \Delta T_i^R \tag{3.58}$$

where

$$K_i = \frac{1}{\delta_i^2}\frac{u_i(t)}{\lambda(t)}\big(1-\alpha(t+\Delta t)\big)E^C(\Delta t) \tag{3.59}$$

and

$$\begin{aligned}\Delta T_i^R =& \frac{-1}{\delta_i}\frac{u_i(t)}{\lambda(t)}\Delta\alpha\left(\sigma_i^f + E_\infty\lambda(t) + \sum_{j=1}^{P} S_j(t)\right)\\ &+ \frac{1}{\delta_i}\frac{u_i(t)}{\lambda(t)}\big(1-\alpha(t+\Delta t)\big)\left(-\sum_{j=1}^{P}\left(1-e^{-\frac{E_j}{\eta_j}\Delta t}\right)S_j(t)\right)\end{aligned} \tag{3.60}$$

and

$$E^C(\Delta t) = E_\infty + \frac{1}{\Delta t}\sum_{j=1}^{P}\eta_j\left(1-e^{-\frac{E_j}{\eta_j}\Delta t}\right) \tag{3.61}$$

and

$$S_j(t) = e^{-\frac{E_j}{\eta_j}\Delta t} S_j(t-\Delta t) + \eta_j R_\lambda \left(1 - e^{-\frac{E_j}{\eta_j}\Delta t}\right) \tag{3.62}$$

3.1.6 Finite Element Formulation

The main objective of solving a solid mechanic problem is to predict displacements, strains, and stresses throughout an object when it is subjected to a set of boundary conditions. In this study, a finite element (FE) formulation is utilized to predict these unknown. This section explains the steps to obtain the FE formulation for this problem. The weak formulation is obtained by multiplying conservation of linear momentum by an arbitrary weight function, δu_i, and integrating it over domain V. The resulting equation can be written in the symmetric variational form:

$$\int_V \left(\delta u_i \sigma_{ji}\right)_{,j} dV = \int_V \delta u_{i,j} \sigma_{ji}\, dV \tag{3.63}$$

Applying the divergence theorem and Cauchy's formula into Equation 3.63 yields:

$$\int_V \delta\epsilon_{ij}\, \sigma_{ji}\, dV = \int_{S_{E_t}} \delta u_i\, \hat{T}_i\, dS + \int_{S_C} \delta u_i\, T_i\, dS \tag{3.64}$$

where traction, $\hat{T}_i$, is specified on S_{E_t}; cohesive zone traction, T_i, is specified on S_C; displacements are applied on S_{E_u}.

The state variables can be expressed in incremental form as follows:

$$\Delta\sigma_{ij} \equiv \sigma_{ij}(t+\Delta t) - \sigma_{ij}(t) \tag{3.65a}$$

$$\Delta\epsilon_{ij} \equiv \epsilon_{ij}(t+\Delta t) - \epsilon_{ij}(t) \tag{3.65b}$$

$$\Delta u_i \equiv u_i(t+\Delta t) - u_i(t) \tag{3.65c}$$

Substituting Equation 3.65c into Equation 3.64 and reformulating gives:

$$\int_V \delta\Delta\epsilon_{ij}\,\sigma_{ji}(t)\,dV + \int_V \delta\Delta\epsilon_{ij}\,\Delta\sigma_{ji}\,dV = \int_{S_{E_t}} \delta\Delta u_i\,\hat{T}_i(t+\Delta t)\,dS - \int_{S_C} \delta\Delta u_i\,T_i(t)\,dS - \int_{S_C} \delta\Delta u_i\,\Delta T_i\,dS \quad (3.66)$$

Introducing Equations 3.58 and 3.42 in Equation 3.66 and rearranging gives the following relation:

$$\begin{aligned}\int_V \delta\Delta\epsilon_{ij}\,C'_{ijkl}\,\Delta\epsilon_{kl}\,dV + \int_{S_C} \delta\Delta u_i\,K_i\Delta u_i\,dS &= \int_{S_{E_t}} \delta\Delta u_i\,\hat{T}_i(t+\Delta t)\,dS \\ - \int_V \delta\Delta\epsilon_{ij}\,\sigma_{ij}(t)\,dV - \int_V \delta\Delta\epsilon_{ij}\,\Delta\sigma^R_{ij}\,dV - \int_{S_C} \delta\Delta u_i\,T_i(t)\,dS - \int_{S_C} \delta\Delta u_i\,\Delta T^R_i\,dS\end{aligned} \quad (3.67)$$

Applying the displacement shape function, $\{\boldsymbol{\Delta u}\} = [\boldsymbol{N}]\{\boldsymbol{\Delta U}\}$, strain–displacement operator, $\{\boldsymbol{\Delta\epsilon}\} = [\boldsymbol{B}]\{\boldsymbol{\Delta U}\}$, and displacement transformation function, $\{\boldsymbol{\Delta u}\} = [\boldsymbol{N_C}]\{\boldsymbol{\Delta U}\}$, gives:

$$\begin{aligned}\int_V \big[\boldsymbol{\delta\Delta U}\big]^T\big[\boldsymbol{B}\big]^T\big[\boldsymbol{C'}\big]\big[\boldsymbol{B}\big]^T\big[\boldsymbol{\Delta U}\big]dV + \int_{S_C} \big[\boldsymbol{\delta\Delta U}\big]^T\big[\boldsymbol{N_C}\big]^T\big[\boldsymbol{K}\big]\big[\boldsymbol{N_C}\big]^T\big[\boldsymbol{\Delta U}\big]dS &= \int_{S_{E_t}} \big[\boldsymbol{\delta\Delta U}\big]^T\big[\boldsymbol{N}\big]^T\big[\hat{\boldsymbol{T}}(t+\Delta t)\big]dS \\ - \int_V \big[\boldsymbol{\delta\Delta U}\big]^T\big[\boldsymbol{B}\big]^T\big[\boldsymbol{\sigma}(t)\big]dV - \int_V \big[\boldsymbol{\delta\Delta U}\big]^T\big[\boldsymbol{B}\big]^T\big[\boldsymbol{\Delta\sigma}^R\big]dV \\ - \int_{S_C} \big[\boldsymbol{\delta\Delta U}\big]^T\big[\boldsymbol{N_C}\big]^T\big[\boldsymbol{T}(t)\big]dS - \int_{S_C} \big[\boldsymbol{\delta\Delta U}\big]^T\big[\boldsymbol{N_C}\big]^T\big[\boldsymbol{\Delta T}^R\big]dS\end{aligned} \quad (3.68)$$

Since $[\boldsymbol{\delta\Delta U}]^T$ is arbitrary, it can be factored out. Then Equation 3.68 can be represented for each element as follows:

$$\big\{\boldsymbol{F}^e\big\} = \big[\boldsymbol{K}^e\big]\big\{\boldsymbol{\Delta U}^e\big\} \quad (3.69)$$

where

$$\left[\boldsymbol{K}^e\right] = \left[\boldsymbol{K}_1^e\right] + \left[\boldsymbol{K}_2^e\right] \tag{3.70}$$

$$\left[\boldsymbol{K}_1^e\right] = \int_{V^e} \left[\boldsymbol{B}\right]^T \left[\boldsymbol{C'}\right] \left[\boldsymbol{B}\right]^T \left[\boldsymbol{\Delta U}\right] dV \tag{3.71a}$$

$$\left[\boldsymbol{K}_2^e\right] = \int_{S_C^e} \left[\boldsymbol{N}_C\right]^T \left[\boldsymbol{K}\right] \left[\boldsymbol{N}_C\right]^T \left[\boldsymbol{\Delta U}\right] dS \tag{3.71b}$$

and

$$\left[\boldsymbol{f}^e\right] = \left[\boldsymbol{f}_1^e\right] + \left[\boldsymbol{f}_2^e\right] + \left[\boldsymbol{f}_3^e\right] + \left[\boldsymbol{f}_4^e\right] + \left[\boldsymbol{f}_5^e\right] \tag{3.72}$$

$$\left[\boldsymbol{f}_1^e\right] = \int_{S_{E_t}} \left[\boldsymbol{N}\right]^T \left[\hat{\boldsymbol{T}}(t+\Delta t)\right] dS \tag{3.73a}$$

$$\left[\boldsymbol{f}_2^e\right] = -\int_{V^e} \left[\boldsymbol{B}\right]^T \left[\boldsymbol{\sigma}(t)\right] dV \tag{3.73b}$$

$$\left[\boldsymbol{f}_3^e\right] = -\int_{V^e} \left[\boldsymbol{B}\right]^T \left[\boldsymbol{\Delta\sigma}^R\right] dV \tag{3.73c}$$

$$\left[\boldsymbol{f}_4^e\right] = -\int_{S_C^e} \left[\boldsymbol{N}_C\right]^T \left[\boldsymbol{T}(t)\right] dS \tag{3.73d}$$

$$\left[\boldsymbol{f}_5^e\right] = -\int_{S_C^e} \left[\boldsymbol{N}_C\right]^T \left[\boldsymbol{\Delta T}^R\right] dS \tag{3.73e}$$

where $[\boldsymbol{K}^e]$ is the elemental stiffness matrix including stiffness of bulk element, $[\boldsymbol{K}_1^e]$, and the effects from neighboring cohesive zones, $[\boldsymbol{K}_2^e]$; $[\boldsymbol{f}^e]$ is the elemental force matrix including the contributions from surface tractions, $[\boldsymbol{f}_1^e]$, stresses at the previous time step, $[\boldsymbol{f}_2^e]$, changes in stresses during the current time step, $[\boldsymbol{f}_3^e]$, cohesive zone tractions at the previous time step, $[\boldsymbol{f}_4^e]$, and changes in cohesive zone tractions during the current time step, $[\boldsymbol{f}_5^e]$.

Global system of equations can be obtained by assembling elemental stiffness

matrices and force vectors, as follows:

$$\big[\boldsymbol{K}^g\big]\big\{\boldsymbol{\Delta U}^g\big\} = \big\{\boldsymbol{F}^g\big\} \tag{3.74}$$

where $[\boldsymbol{K}^g]$ is the total global stiffness matrix; $\{\boldsymbol{F}^g\}$ is the total global force vector; $\{\boldsymbol{\Delta U}^g\}$ is the global displacement increment during Δt, which is unknown.

Shape Functions of CST Elements

Displacements in the domain of a finite element can be interpolated by the following relation

$$\big\{\boldsymbol{u}\big\} = \big[\boldsymbol{N}\big]\big\{\boldsymbol{U}\big\} \tag{3.75}$$

where $\{\boldsymbol{U}\}$ is the nodal displacement vector and $[\boldsymbol{N}]$ is the shape function matrix defined as follows

$$\big[\boldsymbol{N}\big] = \begin{bmatrix} N_1 & 0 & N_2 & 0 & N_3 & 0 \\ 0 & N_1 & 0 & N_2 & 0 & N_3 \end{bmatrix} \tag{3.76}$$

For Constant Strain Triangle (CST) element the shape functions are given by

$$\begin{aligned} N_1^e &= \frac{1}{2A^e}\Big(x_2^e y_3^e - x_3^e y_2^e + \big(y_2^e - y_3^e\big)x + \big(x_3^e - x_2^e\big)y\Big) \\ N_2^e &= \frac{1}{2A^e}\Big(x_3^e y_1^e - x_1^e y_2^e + \big(y_3^e - y_1^e\big)x + \big(x_1^e - x_2^e\big)y\Big) \\ N_3^e &= \frac{1}{2A^e}\Big(x_1^e y_2^e - x_2^e y_1^e + \big(y_1^e - y_2^e\big)x + \big(x_2^e - x_1^e\big)y\Big) \end{aligned} \tag{3.77}$$

where

$$2A^e = \big(x_2^e y_3^e - x_3^e y_2^e\big) + \big(x_3^e y_1^e - x_1^e y_3^e\big) + \big(x_1^e y_2^e - x_2^e y_1^e\big) \tag{3.78}$$

Also, the strain of a CST element can be estimated by

$$\big\{\boldsymbol{\epsilon}\big\} = \big[\boldsymbol{B}\big]\big\{\boldsymbol{U}\big\} \tag{3.79}$$

where the derivatives of shape functions for CST elements are given by

$$\left[\boldsymbol{B}\right] = \begin{bmatrix} \frac{\partial N_1}{\partial x} & 0 & \frac{\partial N_2}{\partial x} & 0 & \frac{\partial N_3}{\partial x} & 0 \\ 0 & \frac{\partial N_1}{\partial y} & 0 & \frac{\partial N_2}{\partial y} & 0 & \frac{\partial N_3}{\partial y} \\ \frac{\partial N_1}{\partial y} & \frac{\partial N_1}{\partial x} & \frac{\partial N_2}{\partial y} & \frac{\partial N_2}{\partial x} & \frac{\partial N_3}{\partial y} & \frac{\partial N_3}{\partial x} \end{bmatrix} \tag{3.80}$$

Transformation Funcions of Cohesive Zone Interface Elements

The four-noded interface elements are used in this study to model the cohesive cracks, as shown in Figure 3.5. Each node has two degrees of freedom. Hence, the interface elements can have relative opening in normal direction, $\delta U_n = U_n^2 - U_n^1$, and tangential direction, $\delta U_t = U_t^2 - U_t^1$. The superscripts indicate node numbers and the subscripts refer to the coordinate system. The constitutive equation relating the transferred loads to the relative opening of interface elements in the local coordinate system is as follows:

$$\left\{\boldsymbol{F}^l\right\} = \left[\boldsymbol{E}^l\right]\left\{\boldsymbol{\delta U}^l\right\} \tag{3.81}$$

where

$$\left\{\boldsymbol{F}^l\right\} = \begin{Bmatrix} F_n \\ F_t \end{Bmatrix} \tag{3.82}$$

$$\left\{\boldsymbol{E}^l\right\} = \begin{bmatrix} E_n & 0 \\ 0 & E_t \end{bmatrix} \tag{3.83}$$

and

$$\left[\boldsymbol{\Delta U}^l\right] = \begin{Bmatrix} \Delta U_n \\ \Delta U_t \end{Bmatrix} \tag{3.84}$$

It should be mentioned that $F_i = T_i\, w$ and $E_i = K_i\, w$ where w is the width of the cohesive interface element. T_i and K_i are transferred load and tangent stiffness of cohesive zone respectively. T_i and K_i can be calculated at each time step using Equation 3.47 and Equation 3.59. The subscripts t and n indicates the normal and tangential directions in the local coordinate system.

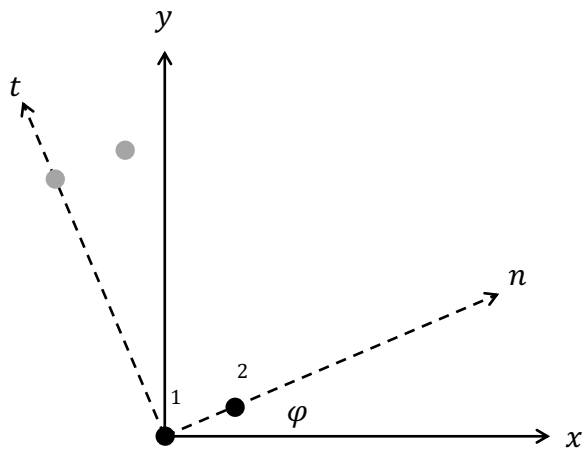

Figure 3.5: The four-node cohesive interface elements.

Because the cohesive constitutive relationship is defined in terms of local separation and traction of cohesive interface element, a transformation between local and global coordinate system is necessary. Let's assume the crack direction, t, makes an angle of $\pi/2 + \varphi$ with the x axis in the global coordinate system, as shown in Figure 3.5. The global relative opening of cohesive interface element can be obtained as

$$\begin{Bmatrix} \Delta U_n \\ \Delta U_t \end{Bmatrix} = \left[\boldsymbol{N}_C\right] \begin{Bmatrix} U_x^1 \\ U_y^1 \\ U_x^2 \\ U_y^2 \end{Bmatrix} \tag{3.85}$$

where

$$\left[\boldsymbol{N}_C\right] = \begin{bmatrix} -\cos(\phi) & -\sin(\phi) & \cos(\phi) & \sin(\phi) \\ \sin(\phi) & -\cos(\phi) & -\sin(\phi) & \cos(\phi) \end{bmatrix} \tag{3.86}$$

The elemental stiffness matrix $\left\{\boldsymbol{K}^g\right\}$ and the nodal force vector $\left\{\boldsymbol{F}^g\right\}$ in the global coordinate system can be derived based on transformation relations.

$$\left\{\boldsymbol{F}^g\right\} = \left[\boldsymbol{N}_C\right]^T \left\{\boldsymbol{F}^l\right\} \tag{3.87}$$

$$\left\{\boldsymbol{K}^g\right\} = \left[\boldsymbol{N}_C\right]^T \left\{\boldsymbol{K}^l\right\} \left[\boldsymbol{N}_C\right] \tag{3.88}$$

3.2 Core Part No. 2: Localization of RVE

In this study, it is assumed that an RVE fails when a localized band forms inside the RVE. Localization is regarded as onset of weak discontinuity surface. Before explaining the theoretical aspect of weak discontinuity surface for 2D cases, first the nature of the localization phenomena is explained using a simple 1D example [Jirasek, 2007].

Consider a straight bar, as shown in Figure 3.6, which is made of a material with a bilinear stress–strain behavior. As shown in Figure 3.7, the first part of stress–strain curve is a linear elastic behavior up to σ_t, while the second phase is a linear softening behavior. Assume the bar is under a uniaxial tensile loading by an applied displacement of u. The bar's response remains in elastic regime while the resultant stress is less than σ_t. The equilibrium condition dictates a uniform stress along the bar. Therefore, all points along the bar experience a unique stress and a corresponding strain. Once the stress level reaches the peak stress, σ_t, any further loading causes resistance reduction of the bar. Hence, the load carrying capacity of

the bar decreases. For any stress level of $\overline{\sigma}$ less than σ_t there are two strain levels which satisfy constitutive equation, ϵ_e and ϵ_s in Figure 3.7. This means unlike the stress profile, the strain profile does not have to be constant through the bar. Any piecewise constant strain profile such as the one shown in Figure 3.6 (b) represents a valid answer. Therefore, the problem has an infinite number of answers. If the bar is truly homogeneous, every point along bar reaches the σ_t and then experience the softening behavior. However, in reality a bar cannot be perfectly uniform. Usually there are some imperfections which make a material point slightly weaker as compared to the neighbor material points. Those points, such as the regions in darker color in Figure 3.6 (a), will reach to the peak stress sooner than the remaining portion of the bar. Then softening starts at weaker points and stress level decreases through the bar. The parts of the bar outside the weaker region unloads elastically, however the weaker regions show increasing strain ϵ_s following a softening behavior. The softening behavior happens only in those areas with minimum strength which can be arbitrarily small. This one-dimensional example explains how localized inelastic strain happens as a process zone with an arbitrarily small width.

The previous simple example explains the localization of deformation in one-dimensional problems. In one-dimensional problems, the criterion for localization can be as simple as when the stress level reaches the peak of the stress–strain curve where the tangent modulus ceases to be positive. In multi-dimensional problems, onset of localization is usually identified through analysis of tangent modulus tensor. The following section mathematically shows that under which conditions localization happens in multi-dimensional problems [Jirasek, 2007]. Localization of deformation is defined as when the inelastic strain increments are localized in an infinitely narrow band which is separated from the neighboring points by weak discontinuity surfaces.

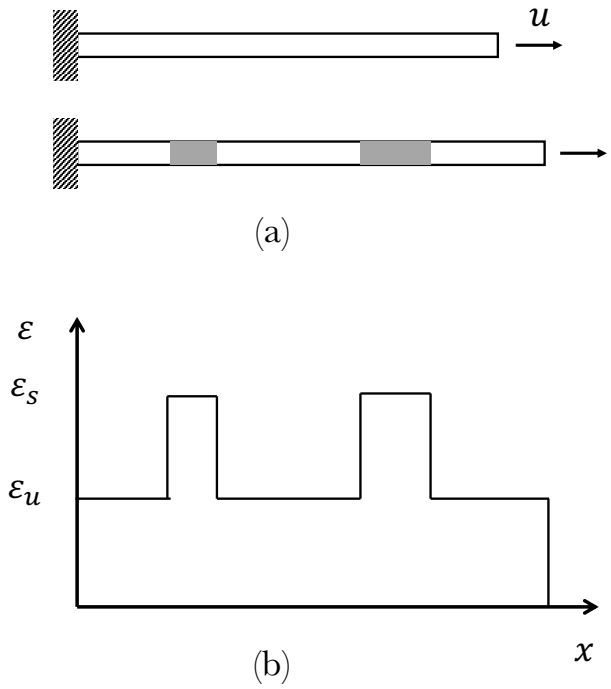

Figure 3.6: (a) A bar under uniaxial tension, (b) and its strain profile.

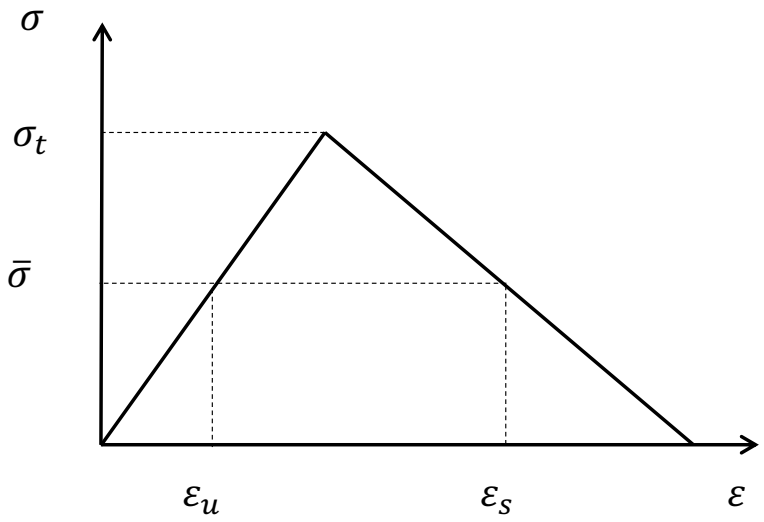

Figure 3.7: Stress–strain diagram.

Weak discontinuity surface is where displacement field is continuous but displacement gradient field, i.e. strain, can have a jump. The onset of localization is when the strain field still remains continuous but the strain rate show potential jumps. Consider a localized deformation surface splits a body into + and − subdomains as shown in Figure 3.8. The unit normal vector to the surface oriented toward + is $\boldsymbol{n}$.

However, there are jumps in stress and strain rates at the localized surface, while the traction and displacement are continuous. The traction continuity is written as

$$\boldsymbol{n}.\dot{\boldsymbol{\sigma}}^{+} = \boldsymbol{n}.\dot{\boldsymbol{\sigma}}^{-} \tag{3.89}$$

where + and − superscripts denote from which side a value is approached. The strain discontinuity condition can be written in the following form

$$\dot{\boldsymbol{\epsilon}}^{+} = \dot{\boldsymbol{\epsilon}}^{-} + \frac{1}{2}(\boldsymbol{m} \otimes \boldsymbol{n} + \boldsymbol{n} \otimes \boldsymbol{m}).\dot{e} \tag{3.90}$$

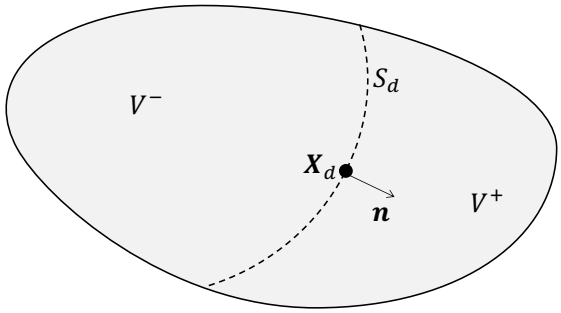

Figure 3.8: Body split by a potential localized deformation surface.

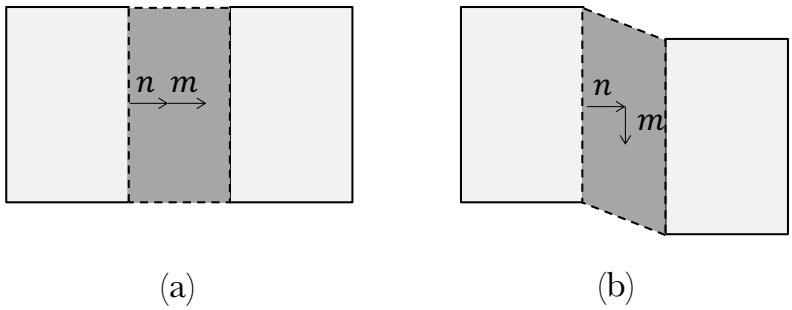

Figure 3.9: Localization band, (a) tensile failure, (b) shear failure.

where $\boldsymbol{m}$ is a unit first-order tensor called *polarization vector*; And $\dot{e}$ is the magnitude of the jump.

Unit vector $\boldsymbol{m}$ shows the direction of strain rate. Hence, the angle between unit vectors $\boldsymbol{m}$ and $\boldsymbol{n}$ describes the failure mode, ranging from opening mode to sliding mode, as shown in Figure 3.9.

The stress and strain rates are connected through the constitutive law as follows

$$\dot{\boldsymbol{\sigma}}^+ = \boldsymbol{C} : \dot{\boldsymbol{\epsilon}}^+, \dot{\boldsymbol{\sigma}}^- = \boldsymbol{C} : \dot{\boldsymbol{\epsilon}}^- \tag{3.91}$$

where $\boldsymbol{C}$ is the tangent stiffness tensor. For simplification it is assumed that at the

onset of localization $\boldsymbol{C}^{+} = \boldsymbol{C}^{-}$.

Substituting Equation 3.91 into Equation 3.45, replacing $\dot{\boldsymbol{\epsilon}}^{+}$ using Equation 3.90, and using the minor symmetry of $\boldsymbol{C}$ lead to

$$\boldsymbol{n}.\boldsymbol{C} : \dot{\boldsymbol{\epsilon}}^{-} + \boldsymbol{n}.\boldsymbol{C} : (\boldsymbol{m} \otimes \boldsymbol{n}).\dot{e} = \boldsymbol{n}.\boldsymbol{C} : \dot{\boldsymbol{\epsilon}}^{-} \tag{3.92}$$

By reorganizing the equation and the fact that $\dot{e} \neq 0$, we obtain

$$(\boldsymbol{n}.\boldsymbol{C}.\boldsymbol{n}).\boldsymbol{m} = \boldsymbol{0} \tag{3.93}$$

The second-order tensor $\boldsymbol{Q} = \boldsymbol{n}.\boldsymbol{C}.\boldsymbol{n}$ is called *localization tensor*. Therefore, formation of localized strain band requires that the localization tensor be singular, i.e. $det(\boldsymbol{Q}) = 0$, where $\boldsymbol{m}$ is its eigenvector associated with eigenvalue zero. Also, singularity of localization tensor is also called the *loss of ellipticity*. Loss of ellipticity is necessary but not sufficient for the formation of localized band with a weak discontinuity, because the analysis presented here is limited to a point $\boldsymbol{x}_d$ and its infinitely small neighborhood. Localization tensor can also be written in index notation form as follows.

$$Q_{ij} = n_k C_{iklj} n_l \tag{3.94}$$

Localization tensor is a function of tangent stiffness tensor $\boldsymbol{C}$ and unit vector $\boldsymbol{n}$. However tangent stiffness matrix is known at each stage, unit vector $\boldsymbol{n}$ is not given a priori. So, the first step is to find a unit vector $\boldsymbol{n}$ such that the $det(\boldsymbol{Q})$ becomes zero. If such a vector does not exist, the strain field remains continuous. If there is a unit vector $\boldsymbol{n}$ that satisfies singularity of the localization tensor, a weak discontinuity surface with a normal $\boldsymbol{n}$ can form [Jirasek, 2007].

As discussed earlier, for nonlinear finite-deformation problems the relation between stress and strain is expressed in an incremental form:

$$\Delta\sigma_{ij} = C_{ijkl}\,\Delta\epsilon_{kl} \tag{3.95}$$

According to the principle of conservation of angular momentum, the stress tensor is symmetric, $\sigma_{ij} = \sigma_{ji}$. In small strain deformation, the linearized strain tensor is also symmetric by definition, $\epsilon_{ij} = \epsilon_{ji}$. Symmetry of stress and strain tensor lead to the conclusion that $\boldsymbol{C}$ must have minor symmetry as follows:

$$C_{ijkl} = C_{jikl} = C_{ijlk} \tag{3.96}$$

If the material possess a strain energy density function, the tensor $\boldsymbol{C}$ exhibits the major symmetry which reduces the number of independent constants even further as follows:

$$C_{ijkl} = C_{klij} \tag{3.97}$$

In 3D space, the minor symmetry of $\boldsymbol{C}$ tensor reduces the number of independent terms from $3 \times 3 \times 3 \times 3 = 81$, to 36. If besides minor symmetry the $\boldsymbol{C}$ tensor has major symmetry, it features only 21 independent terms. For a fully anisotropic material without major symmetry, the stress and strain relation can be written in

matrix form in the following way [Weinberg, 2008, Aboudi et al., 2012]:

$$\begin{Bmatrix} \sigma_{11} \\ \sigma_{22} \\ \sigma_{33} \\ \sigma_{23} \\ \sigma_{13} \\ \sigma_{12} \end{Bmatrix} = \begin{bmatrix} C_{1111} & C_{1122} & C_{1133} & C_{1123} & C_{1113} & C_{1112} \\ C_{2211} & C_{2222} & C_{2233} & C_{2223} & C_{2213} & C_{2212} \\ C_{3311} & C_{3322} & C_{3333} & C_{3323} & C_{3313} & C_{3312} \\ C_{2311} & C_{2322} & C_{2333} & C_{2323} & C_{2313} & C_{2312} \\ C_{1311} & C_{1322} & C_{1333} & C_{1323} & C_{1313} & C_{1312} \\ C_{1211} & C_{1222} & C_{1233} & C_{1223} & C_{1213} & C_{1212} \end{bmatrix} \begin{Bmatrix} \epsilon_{11} \\ \epsilon_{22} \\ \epsilon_{33} \\ \epsilon_{23} \\ \epsilon_{13} \\ \epsilon_{12} \end{Bmatrix} \tag{3.98}$$

which for 2D problems can be represented by:

$$\begin{Bmatrix} \sigma_{11} \\ \sigma_{22} \\ \sigma_{12} \end{Bmatrix} = \begin{bmatrix} C_{1111} & C_{1122} & C_{1112} \\ C_{2211} & C_{2222} & C_{2212} \\ C_{1211} & C_{1222} & C_{1212} \end{bmatrix} \begin{Bmatrix} \epsilon_{11} \\ \epsilon_{22} \\ \epsilon_{12} \end{Bmatrix} \tag{3.99}$$

Equation 3.99 can be written in terms of compliance as well:

$$\begin{Bmatrix} \epsilon_{11} \\ \epsilon_{22} \\ \epsilon_{12} \end{Bmatrix} = \begin{bmatrix} S_{1111} & S_{1122} & S_{1112} \\ S_{2211} & S_{2222} & S_{2212} \\ S_{1211} & S_{1222} & S_{1212} \end{bmatrix} \begin{Bmatrix} \sigma_{11} \\ \sigma_{22} \\ \sigma_{12} \end{Bmatrix} \tag{3.100}$$

In equations 3.98, and 3.99, 3.100, the $\boldsymbol{C}$ matrix possesses only the minor symmetry, which leaves 9 independent entries for 2D cases.

3.3 Core Part No. 3: Crack Simulation Using Element Elimination Method

Crack propagation can be regraded as creation of new traction-free boundaries, crack faces. Numerous techniques have been developed and implemented in FE framework

to simulate crack nucleation and propagation. Some of the techniques to simulate crack advancement are based on consecutively redefining FE mesh, such as *node decoupling*, *element splitting*, and *element elimination* methods [Mishnaevsky Jr, 2007].

In node decoupling method, which is also called as node splitting method, a crack grows once a node ahead of a crack tip is cloned and decoupled from the original node (Figure 3.10 (a)). This technique allows cracks to grow only on the edges of the elements which leads to a mesh-dependent results [Mishnaevsky Jr, 2007]. Element splitting technique allows a crack to propagate through an element as it is shown in Figure 3.10 (b) [Wang et al., 2009, Johnson et al., 2005]. This method is less mesh-bias as compared to the node decoupling method because the crack path is not limited to the element edges, but more challenging numerically [Leon et al., 2014].

Element elimination method does not require cloning nodes. The new boundaries, i.e. crack walls, are created by removing an element or elements ahead of the crack tip for which the failure criterion is satisfied, as shown in Figure 3.10 (c). However, this method clearly induces physical inaccuracy by violating the conservation of mass and mesh-dependency, while the overall accuracy can be improved by defining a finer and unstructured mesh [Lee et al., 2009, Leon et al., 2014]. Element elimination method has been implemented by many commercial FE software, such as ABAQUS and LS-DYNA due to its simplicity and fast performance. Also, since the failed element is removed in this method, this method can overcome the stress concentration at the cracked surface and thereby prevent over-estimation of stress and strain values. Element elimination method has fundamental similarities with *Element Weakening* method, in which when the failure criterion is met for an element, the element is not removed but its stiffness is set to a very low value [Mishnaevsky Jr, 2007].

This study uses artificial elimination of failed elements from the finite element

solution without changing the mesh structure. The flowchart of implementation of element elimination method within a FE framework is illustrated in Figure 3.11. Instead of removing a failed element from the FE solution, its contribution is excluded from updating stiffness matrix and force vector. The implementation of this method requires three steps that are repeated at each time step:

- **Identifying failed elements**: A failure criterion determines those elements that need to be eliminated at each time step. When the failure criterion are met for an element/elements, candidate element/elements for elimination will be stored for the next time step. In this study, it is assumed that once an element meet the weak discontinuity criterion, it is no longer able to carry load.

- **Eliminating failed elements**: Failed elements are excluded from connectivity matrix. In order to do that the contribution of failed elements to stiffness matrix and force vector is excluded during assembling of the global stiffness matrix and global force vector without changing the connectivity matrix or renumbering mesh.

- **Adjusting boundary condition**: Excluding element may result in producing isolated nodes. Isolated nodes are the ones that remain without involving in neighboring elements when all the surrounding elements are eliminated. If these nodes are part of boundary condition nodes, the boundary condition should be adjusted appropriately.

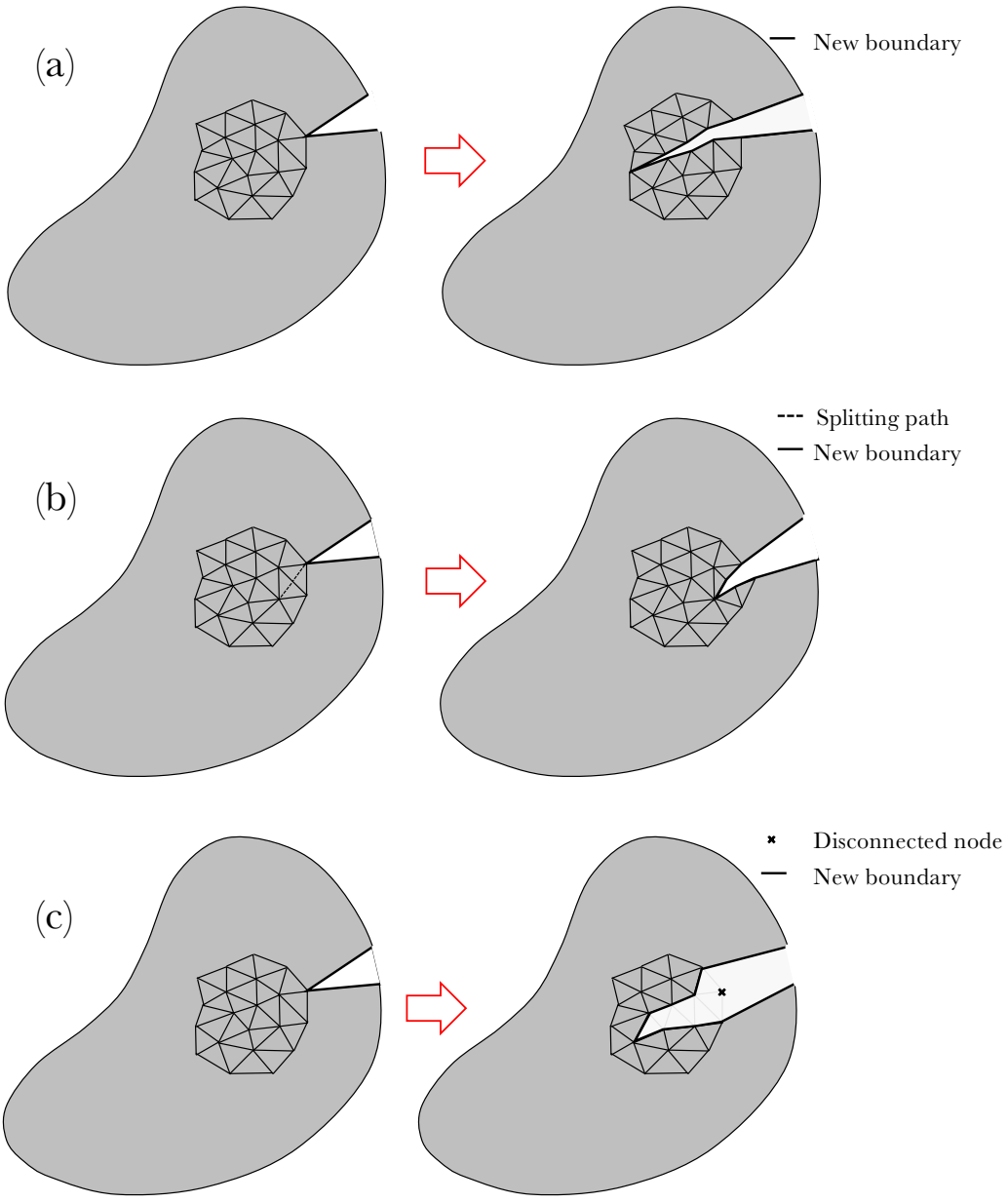

Figure 3.10: Sketch of (a) node decoupling method (b) element splitting method (c) element elimination method for crack simulation.

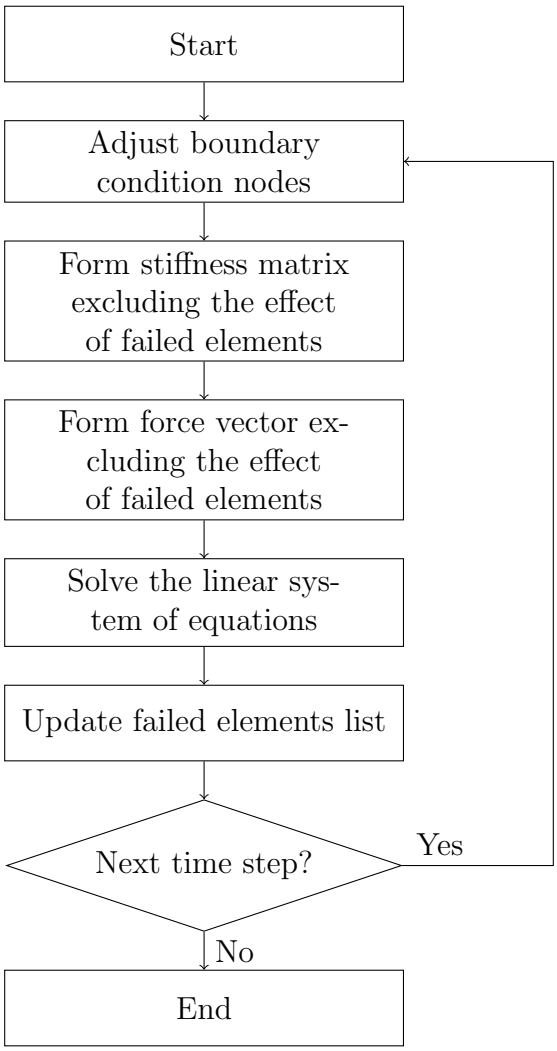

Figure 3.11: Flowchart of implementation of element elimination method into a FE framework.

Chapter 4

Implementation of Algorithms

4.1 Introduction

This chapter explains the Finite Element (FE) algorithm utilized to simulate crack propagation in heterogeneous materials using a multiscale approach. The entire algorithm is implemented in an in-house FORTRAN 77 code. The initial version of the code, MULTISCALE-SADISTIC, was developed by David H. Allen and is capable of predicting global-scale stiffness reduction due to evolution of damage in local-scale. In the original version of this code, it was assumed that the RVE is isotropic and will remain isotropic even after development of microcracks. In this study, the code was extended as follows:

- Improvement to the cohesive zone model by implementing a penalty method that can avoid interpenetration issue of interface elements.
- Implementation of uniform displacement boundary condition for RVEs.
- Implementation of an algorithm that obtains the anisotropic tangent stiffness

matrix of RVE at each time step.

- Implementation of the bifurcation analysis subroutine to evaluate the onset of weak discontinuity surface in RVE.

- Integration of an element elimination method in global-scale FE in order to simulate discrete fracture.

In a finite element framework, the two-way linked multiscale approach includes solving two Initial Boundary Value Problems (IBVPs) using the nonlinear FE method: global-scale FE problem and local-scale FE problem. Each integration point in global-scale is linked to its exclusive local-scale RVE. The response of RVE governs the constitutive behavior of the integration point. Thus, the local-scale FE problem is solved within the global-scale FE problem to obtain the unknown macroscopic constitutive behavior. Both FE problems are identical in terms of the implementation algorithm. The next section describes the implementation of a nonlinear FE framework in an incrementalized form.

4.2 Nonlinear Finite Element Framework

To capture the time-dependent constitutive properties of materials and progressive damage within an RVE, the nonlinear FE solver was developed in a time incremental form. The step-by-step algorithms of global-scale and local-scale FE solvers are similar and are represented in an incrementalized form in Figure 4.1. Prior to the start of solving the IBVP, the program initializes all state variables to zero and then it enforces the effect of traction BC to the force matrix. After traction BC, the stiffness matrix is calculated for each element, $[\boldsymbol{K}^e]$. The element stiffness matrices are as-

sembled to obtain the global stiffness matrix, $[\boldsymbol{K}^g]$. The force vector is also obtained for each element, $\{\boldsymbol{F}^e\}$, and is assembled over the entire domain to obtain the global force vector, $\{\boldsymbol{F}^g\}$. Once $[\boldsymbol{K}^g]$ and $\{\boldsymbol{F}^g\}$ are calculated, both are adjusted based on the effect of the displacement BC. Finally, the linear system of equations given by the assembled stiffness matrix and the assembled force vector is solved for unknown displacement increments using Equation 3.74. Once displacement increments are obtained, the corresponding strain increments, $\Delta\epsilon_{ij}$, and stress increments, $\Delta\sigma_{ij}$, are calculated.

4.3 Two-way Linked Multiscale Modeling of Fracture Framework

All the steps used to obtain the solution of multiscale simulation of crack propagation are presented in Figure 4.2. For each time step, global-scale IBVP is solved to obtain the solution for global-scale state variables. At each integration point in global-scale that is linked to local-scale RVE, the FE solution results are exchanged between the global-scale FE model and the local-scale FE model and vice versa, as follows:

- **Global-scale to local-scale**: The global-scale incremental responses, $\Delta\sigma_{ij}^G$ and $\Delta\epsilon_{ij}^G$, are sent to the local-scale model to determine the equivalent RVE responses.

- **Local-scale to global-scale**: The homogenized tangent stiffness tensor C_{ijkl}^* is sent to the global-scale for the next time step analysis.

In this study, the global-scale strain solution is used to obtain homogeneous displacement boundary condition on an RVE as expressed in Equation 3.2. Considering

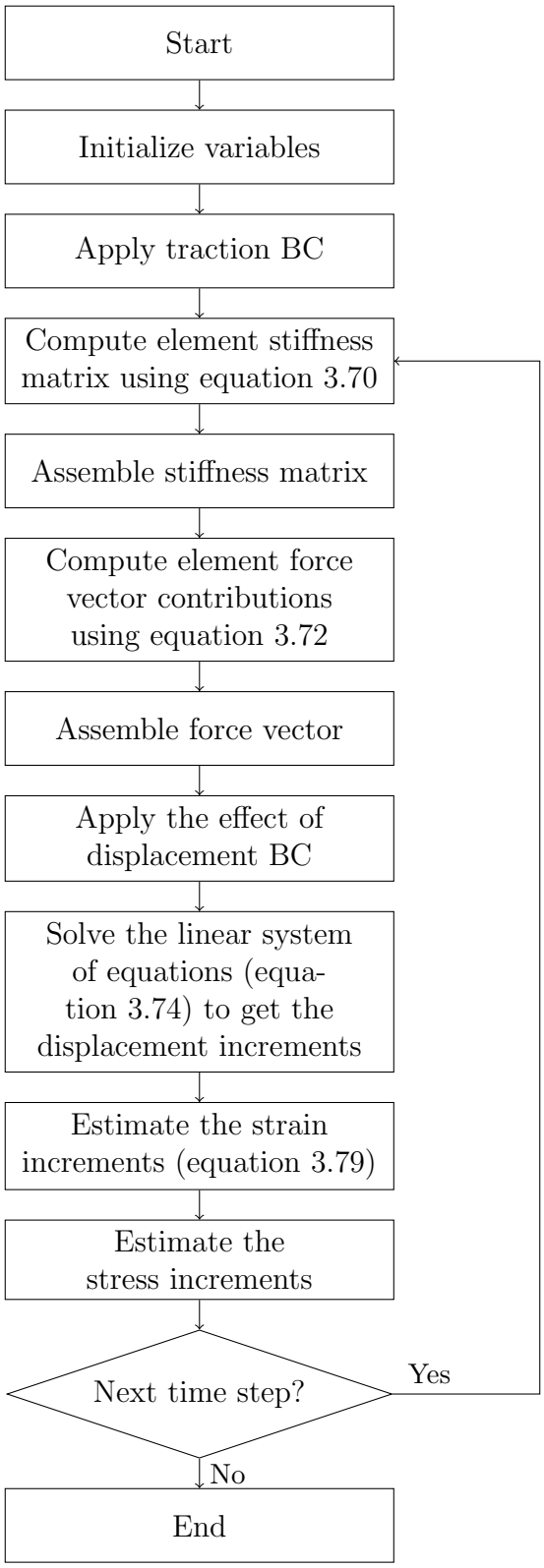

Figure 4.1: Flowchart of forming and solving an IBVP using an incrementalized FE algorithm.

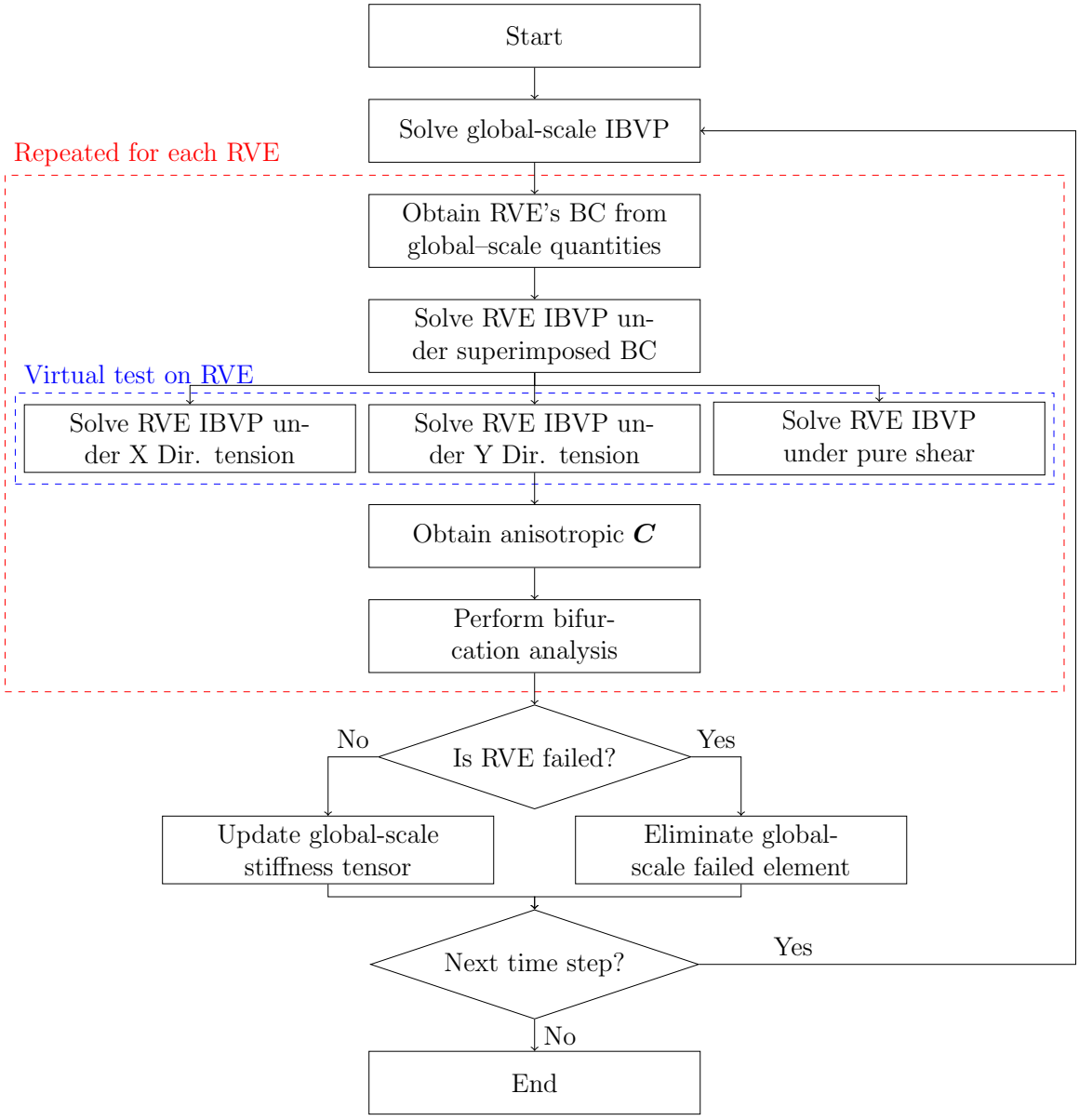

Figure 4.2: Algorithm for multiscale fracture simulation.

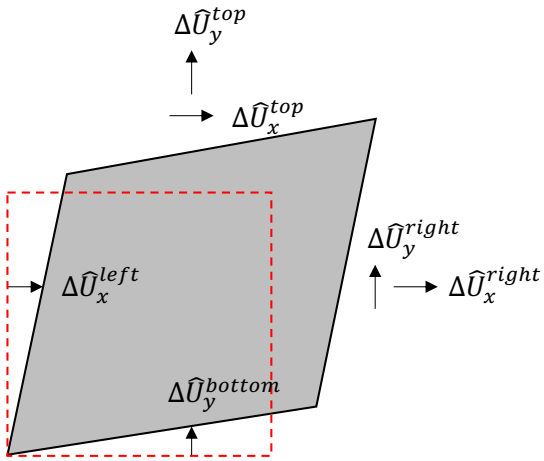

Figure 4.3: Homogeneous displacement boundary condition.

the RVE shown in Figure 4.3, the following incremental displacement boundary condition is applied to the external boundary of RVE:

$$\Delta\hat{U}_x^{left} = \frac{1}{2}\,\Delta\epsilon_{xy}^{G}\,y \tag{4.1}$$

$$\Delta\hat{U}_y^{left} = 0 \tag{4.2}$$

$$\Delta\hat{U}_x^{top} = \frac{1}{2}\,\Delta\epsilon_{xy}^{G}\,w_{RVE} \tag{4.3}$$

$$\Delta\hat{U}_y^{top} = \Delta\epsilon_{yy}^{G}\,w_{RVE} + \frac{1}{2}\,\Delta\epsilon_{xy}^{G}\,x \tag{4.4}$$

$$\Delta\hat{U}_x^{right} = \Delta\epsilon_{xx}^{G}\,w_{RVE} + \frac{1}{2}\,\Delta\epsilon_{xy}^{G}\,y \tag{4.5}$$

$$\Delta\hat{U}_y^{right} = \frac{1}{2}\,\Delta\epsilon_{xy}^{G}\,w_{RVE} \tag{4.6}$$

$$\Delta\hat{U}_x^{bottom} = 0 \tag{4.7}$$

$$\Delta\hat{U}_y^{bottom} = \frac{1}{2}\,\Delta\epsilon_{xy}^{G}\,x \tag{4.8}$$

where w_{RVE} is the width of the RVE.

Then the RVE IBVP is solved under prescribed boundary condition for incremen-

tal strain and stress. The response of RVE represents the current stage of RVE which may involve development of microcracks. The response of RVE is used to obtain the homogenized tangent stiffness tensor, as shown in Equation 3.3. If the damaged RVE can be reasonably approximated by an isotropic constitutive model, the Equation 3.3 is reduced to the following form, at each time step:

$$\Delta\bar{\sigma}_{ij}^{L} = \lambda^{*}\ \Delta\bar{\epsilon}_{kk}^{L}\ \delta_{ij} + 2\mu^{*}\ \Delta\bar{\epsilon}_{ij}^{L} \tag{4.9}$$

where λ and μ are the Lame parameters; the superscript * indicates the homogenized quantities. Lame parameters are calculated using the following equations:

$$\mu^{*} = \frac{1}{2}\ \frac{\Delta\bar{\sigma}_{ij}^{L}}{2\ \Delta\bar{\epsilon}_{ij}^{L}} \tag{4.10}$$

$$\lambda^{*} = \frac{1}{3}\ \frac{\Delta\bar{\sigma}_{kk}^{L}}{2\ \Delta\bar{\epsilon}_{kk}^{L}} - \frac{2}{3}\ \mu^{*} \tag{4.11}$$

The lame parameters are used to calculate elastic moduli and Poisson's ratio:

$$E^{*} = \frac{\mu^{*}(3\lambda^{*} + 2\mu^{*})}{\lambda^{*} + \mu^{*}} \tag{4.12}$$

$$\nu^{*} = \frac{\lambda^{*}}{2(\lambda^{*} + \mu^{*})} \tag{4.13}$$

For plane strain and plane stress deformations, the isotropic tangent stiffness can be simplified and written in terms of E^{*} and ν^{*}.

- For plane strain:

$$\boldsymbol{C}^{*} = \frac{E^{*}}{(1+\nu^{*})(1-2\nu^{*})} \begin{bmatrix} 1-\nu^{*} & \nu^{*} & 0 \\ \nu^{*} & 1-\nu^{*} & 0 \\ 0 & 0 & \frac{1-2\nu^{*}}{2} \end{bmatrix} \tag{4.14}$$

- For plane stress:

$$\boldsymbol{C}^* = \frac{E^*}{1-\nu^{*2}} \begin{bmatrix} 1 & \nu^* & 0 \\ \nu^* & 1 & 0 \\ 0 & 0 & \frac{1-\nu^*}{2} \end{bmatrix} \tag{4.15}$$

If the RVE is not isotropic due to either its original microstructure or microcrack distribution and orientation, the homogenized tangent stiffness/compliance tensor contains nine unknown components. These components can be determined by separately applying arbitrary small uniaxial normals and shear prescribed displacement increments to the RVE at the end of each time step as shown in Figure 4.4. The unknown components of the anisotropic homogenized tangent compliance matrix, $\boldsymbol{S}^*$, can be obtained using the following three equations which correspond to each loading scenarios presented in Figure 4.4:

$$\begin{Bmatrix} \bar{\epsilon}_{xx} \\ \bar{\epsilon}_{yy} \\ \bar{\epsilon}_{xy} \end{Bmatrix} = \begin{bmatrix} S^*_{11} & Arb. & Arb. \\ S^*_{21} & Arb. & Arb. \\ S^*_{31} & Arb. & Arb. \end{bmatrix} \begin{Bmatrix} \bar{\sigma}_{xx} \\ 0 \\ 0 \end{Bmatrix} \tag{4.16}$$

$$\begin{Bmatrix} \bar{\epsilon}_{xx} \\ \bar{\epsilon}_{yy} \\ \bar{\epsilon}_{xy} \end{Bmatrix} = \begin{bmatrix} Arb. & S^*_{12} & Arb. \\ Arb. & S^*_{22} & Arb. \\ Arb. & S^*_{32} & Arb. \end{bmatrix} \begin{Bmatrix} 0 \\ \bar{\sigma}_{yy} \\ 0 \end{Bmatrix} \tag{4.17}$$

$$\begin{Bmatrix} \bar{\epsilon}_{xx} \\ \bar{\epsilon}_{yy} \\ \bar{\epsilon}_{xy} \end{Bmatrix} = \begin{bmatrix} Arb. & Arb. & S^*_{13} \\ Arb. & Arb. & S^*_{23} \\ Arb. & Arb. & S^*_{33} \end{bmatrix} \begin{Bmatrix} 0 \\ 0 \\ \bar{\sigma}_{xy} \end{Bmatrix} \tag{4.18}$$

The homogenized tangent stiffness matrix, $\boldsymbol{C}^*$, is simply equal to the inverse of $\boldsymbol{S}^*$ matrix.

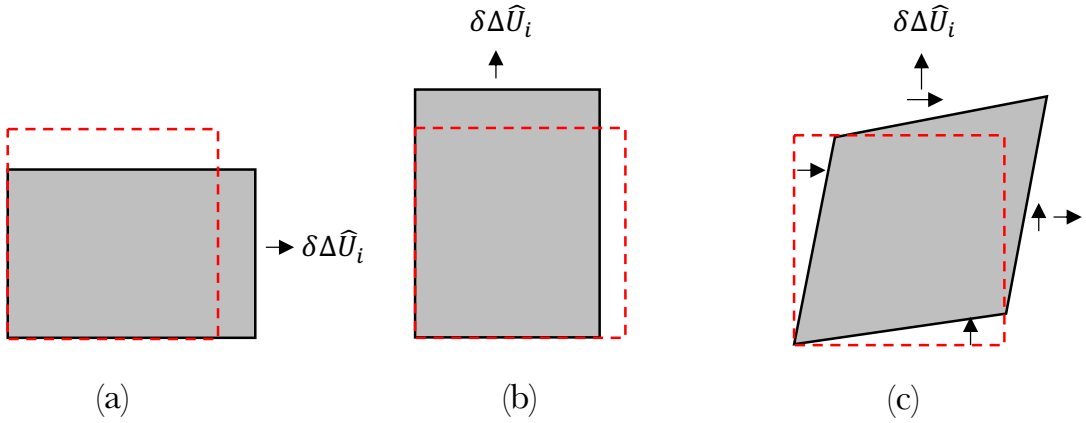

Figure 4.4: Homogeneous displacement boundary condition: (a) Uniaxial tension in X Dir., (b) Uniaxial tension in Y Dir., (c) Pure shear.

Then the anisotropic homogenized tangent stiffness tensor is utilized to predict the onset of localization of RVE using a bifurcation analysis. Based on the status of the RVE, two scenarios can happen. If the RVE satisfies the weak discontinuity criterion, the corresponding element at global-scale will be eliminated. If the RVE is not failed, the global-scale element properties will be updated using the homogenized tangent stiffness tensor. It is worthy to mention that calculating homogenized stiffness tensor and assessing localization of RVE, which are highlighted by a dashed box in Figure 4.2, are repeated for each integration point that is linked to the local-scale RVE. Bifurcation analysis requires that the stiffness tensor be anisotropic without isotropy assumption.

Chapter 5

Example Problems

In this chapter, the viability of the proposed method is demonstrated by solving a few example problems and analyzing the results. First, the process of obtaining the FE model of an RVE is explained. Then, certain example cases are solved to show the capabilities of the proposed approach. The examples are categorized in two groups: first, the models in which no damage is allowed to occur in the RVE, and second, the models in which microcracks are allowed to develop in a user-defined area.

The first step in implementation of the homogenization theory is to define an RVE. In periodic materials, one can simply choose the unit cell of the microstructure as an RVE. However, in random medias, defining an RVE is more complicated. A widely accepted method is to use statistical measures to determine the condition of statistical homogeneity, such as to reach a convergence of effective homogenized properties of RVE [Beran, 2001, Hill, 1972]. According to this approach, one can specify the dimension of an RVE such that the averaged properties of the material is equivalent to the averaged properties obtained from the RVE. The next section describes the process of creating FE model of an RVE of a random particulate composite.

5.1 Obtaining Microstructural FE Model of RVE

In the multiscale modeling approach, the heterogeneity of the material is represented by RVE. So obtaining an RVE that fully represents the features of the actual microstructure, including random spatial distribution and irregular shapes of particles, is crucial, yet is sometimes difficult and time-consuming, especially when the particles have irregular shapes, sizes, and random distribution. Fortunately, there are many imaging technologies such as optical microscopy, scanning electron microscopy (SEM), and atomic force microscopy (AFM) that allow the microstructure of materials to be captured at a wide range of length scales. These microstructure images can be effectively used to create an accurate FE model of heterogeneous materials. In this section, a program, MIDAS-VT-Pre, is designed and developed in MATLAB to assist with generating the two-dimensional FE mesh of particle/fiber embedded composites directly from microstructure images without losing significant morphological details [Zare-Rami, 2018, Zare-Rami and Kim, 2019]. The MIDAS-VT-Pre user's manual is presented in Appendix A.

As mentioned previously, the cohesive zone model (CZM) is used to simulate microcrack development in local-scale RVE [Kim, 2011, Rami et al., 2017]. This method assumes that there is a fictitious fracture process zone ahead of the crack tip that follows a softening behavior. The fracture process zone is simulated using cohesive interface elements. Interface elements connect the two edges shared between adjacent continuum elements. MIDAS-VT-Pre is equipped with a feature for embedding cohesive zone interface elements within the FE mesh structure to simulate potential microcrack propagation. MIDAS-VT-Pre first identifies the microstructure of the heterogeneous material using an image processing method, then meshes the sample

with or without cohesive zone interface elements. These two steps are explained in detail below.

5.1.1 Image processing

MIDAS-VT-Pre is equipped with an image processing module that identifies the microstructure geometry of RVE. This module uses color segmentation tools available in the Image Processing Toolbox of MATLAB. The color segmentation method requires color intensity contrast between constituents. The current version of MIDAS-VT-Pre is capable of handling two-phase mixtures, including distinct particles within a continuous matrix phase. The steps used to obtain an accurate 2D microstructure of the particle/fiber embedded composite are illustrated in Figure 5.1. The program distinguishes particles from the background based on the difference between their color intensities, then converts the original image to a binary one. In the image processing module, it is assumed that the particles are lighter than the background, as shown in Figure 5.1(a). Figure 5.1(b) shows the resulting binary image in which the particles are represented as white objects, while the surrounding matrix phase is represented by the black background. In the next step, the boundary pixels of particles are transformed into a vectoral format to describe the geometry of each particle in the form of a polygon (Figure 5.1(c)). The resulting geometry consists of polygons with a large number of vertices, equal to the number of boundary pixels of the particles. Defining particles with an unreasonably large number of vertices may induce an undesired extremely fine mesh. Therefore, the program removes unnecessary vertices of each polygon in order to define each particle with a much smaller number of vertices, while important geometric features of polygons are retained (Figure 5.1(d)). The image processing module defines the preliminary microstructure in terms of a coordi-

nate system defined by image pixels. Thus, prior to the meshing step, the preliminary microstructure must be scaled from pixel coordinates to the actual size of the sample.

5.1.2 Cohesive Zone Interface Element Insertion

MIDAS-VT-Pre has an automated interface element insertion module. As previously mentioned, the cohesive zone interface element is a four-node element that allows crack propagation within the FE framework to be simulated. The insertion process of cohesive zone interface elements is shown in Figure 5.2. Assume the two bulk elements at the right side are in the non-cracking region, while the other two elements are in the cracking region. Using this method, the interface elements are added within the cracking region; i.e., between elements 1 and 2, and along the boundary of the cracking region; i.e., between elements 2 and 3. Algorithm 1 describes the pseudocode for insertion of interface elements. To define interface elements between the existing mesh structure, the nodes within the cracking region are first duplicated in such a way that no elements share any nodes. Thus, unlike the regular FE mesh, multiple nodes may have the same coordinates (Figure 5.2(b)). Once the new nodes are generated, the element connectivity matrix is updated accordingly. The cohesive interface elements are then defined between adjacent bulk elements using the nodes of overlapped edges, as shown in Figure 5.2(c) and Algorithm 1, lines 10 to 20. Since the node duplication process changes the node numbering order, the Reverse Cuthill-McKee algorithm is used to optimize the nodal numbering in order to minimize the size of the stiffness matrix [Liu and Sherman, 1976].

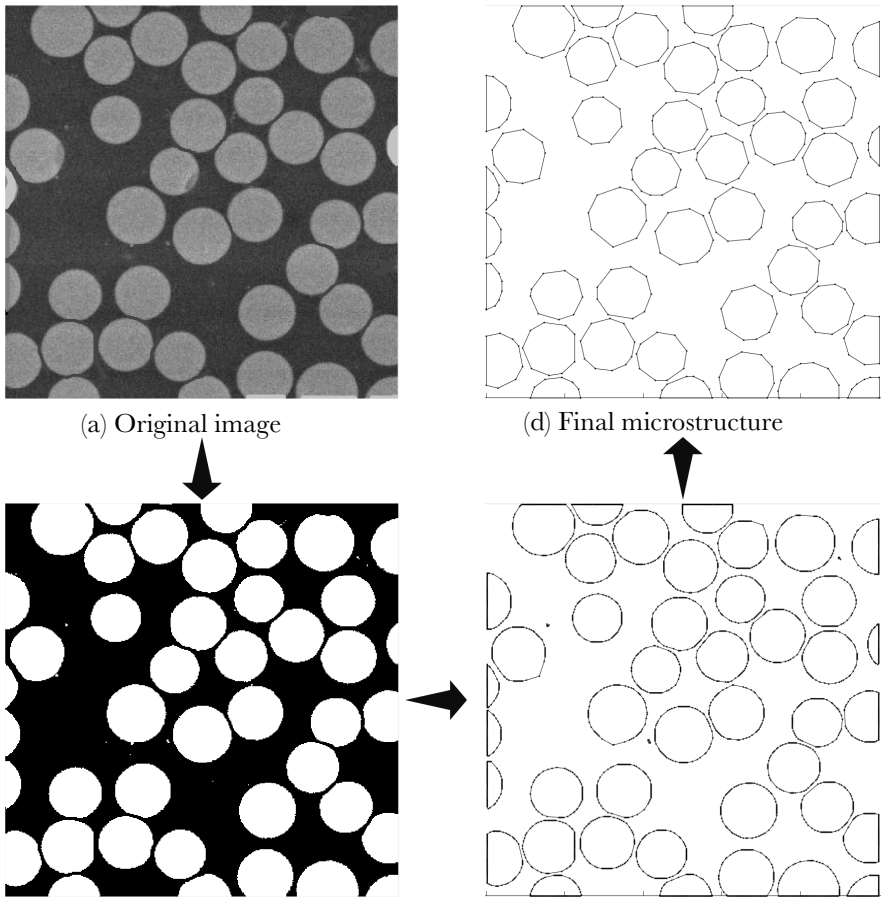

Figure 5.1: Steps of generating 2D microstructure of RVE.

Algorithm 1: Embedding interface elements between bulk elements.

Duplicate nodes and update element connectivity

for $i = 1 : number\ of\ bulk\ elements$ **do**
  if *element* $i \in$ *cracking zone* **then**
    for $j = 1 : 3$ **do** ▷ Loop over element's nodes
      $NewNode(c, 1{:}3) = OldNode(OldConn(i, j), 1{:}3)$
      $NewConn(i, j) = c$ ▷ Update the element connectivity matrix
      $c = c + 1$
    end for
  end if
end for

Define interface elements

for $i = 1 : number\ of\ bulk\ elements$ **do**
  if *element* $i \in$ *cracking zone* **then**
    for $j = 1 : 3$ **do** ▷ Loop over element's edges
      $k \leftarrow neighboring\ element\ number$
      $m \leftarrow the\ first\ node\ of\ the\ overlapped\ edge$
      $n \leftarrow the\ second\ node\ of\ the\ overlapped\ edge$
      $CohConn(c, 1{:}4) = [NewConn(i, m : n)\ NewConn(k, m : n)]$
      $c = c + 1$
    end for
  end if
end for

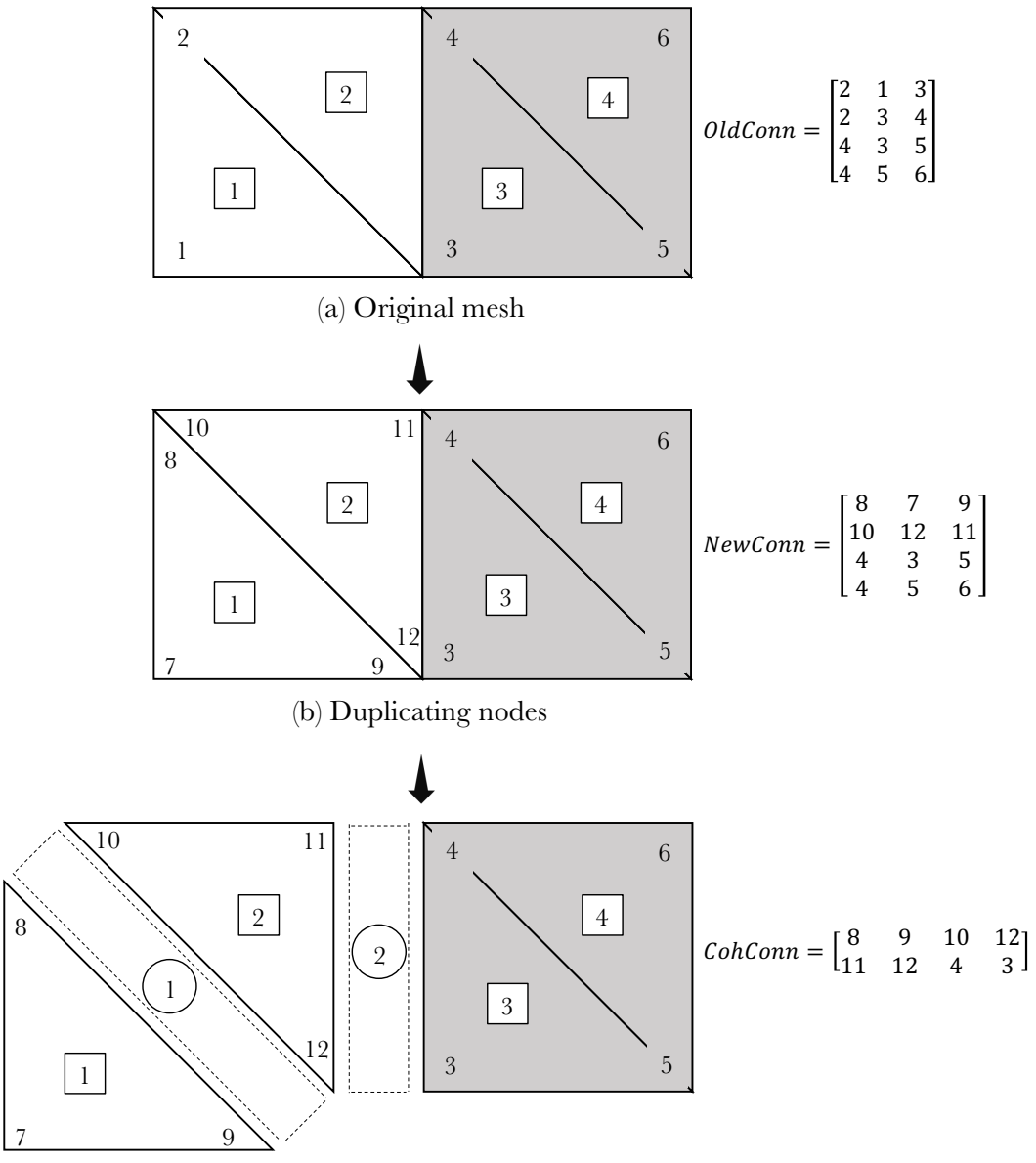

(a) Original mesh

(b) Duplicating nodes

(c) Embedding cohesive interface elements

Figure 5.2: Embedding cohesive zone elements between bulk elements.

5.2 Analyzing Isotropic and Anisotropic RVE without Damage

To show the viability of the proposed method for obtaining the anisotropic tangent stiffness matrix of an RVE in a two-way linked multiscale framework, three multiscale examples are solved and presented in this section. These example problems simulate a three-point bending test in which the integration points of elements of the vertical midline of the beam are linked to an RVE, as shown in Figure 5.3. For applying load to the beam, a displacement control movement is applied to the mid-span of the top of the beam. To minimize the computational cost, a simplified microstructure consisting of one particle is used. The simulation was performed for three different scenarios: Case I, Case II, and Case III. In Case I, Case II, and Case III the global-scale model was linked to RVEs with a circular, horizontal ellipse, and vertical ellipse respectively, as shown in Figure 5.3. These three particle shapes were selected to represent both microstructural isotropy and anisotropy of the RVE even without any damage associated. It should be noted that these models are intended only to illustrate the viability of the proposed model, not to simulate a specific test or material. Thus, the material properties and model dimensions are arbitrarily selected. The material properties for the global and local-scale are presented in Table 5.1. Only the global elements that are not linked to a local-scale model require defined material properties. The properties of the global-scale elements that are linked to the local-scale come from the homogenization of the local-scale response.

The resulting stress contour plots of the global-scale and the local-scale models are illustrated in Figure 5.4. The response of the RVE at two different locations along the midline of the beam was selected to be shown for the three cases. As the beam is

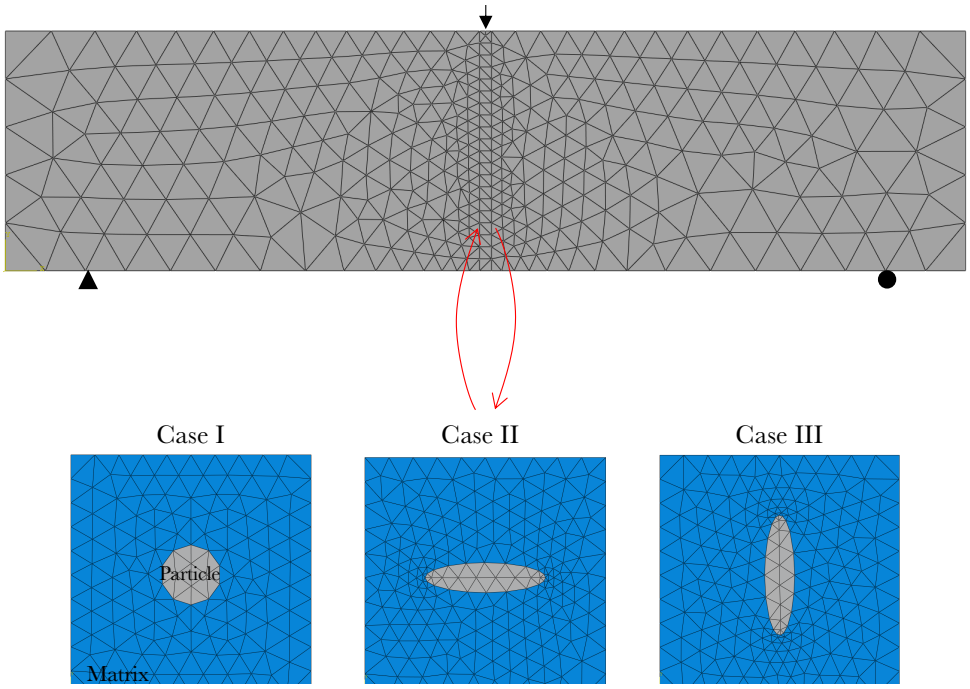

Figure 5.3: A sketch of the multiscale model of a three-point bending test wherein the midline elements are two-way linked to an RVE without damage.

loaded, different elements of the beam experience different states of strain and stress. The global-scale strain (or stress) at each time step is used to obtain the uniform displacement (or traction) boundary condition, which is applied to the corresponding RVE. Thus, it is expected that the RVE linked to location A experiences higher tensile stress as compared to the one linked to location B. The RVE at location A in Case I, II, and III is subjected to almost identical boundary conditions; however, the resulting stress distribution in local-scale model is different. This difference in stress distribution is the result of different RVE microstructures. That explains why two identical objects, except with different microstructure, may result in different amount of damage under the same loading condition.

In order to obtain the anisotropic tangent stiffness matrix, arbitrary displacement boundary conditions are separately applied at each time step to the current stage of

Table 5.1: Material properties of each constituent.

Global-scale bulk element
Elastic properties:
$E = 5000$ (MPa) $\quad \nu = 0.2$
Local-scale particle
Elastic properties:
$E = 2000$ (MPa) $\quad \nu = 0.2$
Local-scale matrix
Elastic properties:
$E = 5000$ (MPa) $\quad \nu = 0.2$

RVE to create simple tension in the x-direction, simple tension in the y-direction, and pure shear, as shown in Figure 5.5. The response of RVE for each loading case is then homogenized and used to calculate the nine independent components of the anisotropic tangent stiffness matrix (Equation 3.100). This method takes into account capturing microstructure- or damage-induced anisotropy during the simulation. The accuracy of this process was assessed by comparing the components of tangent stiffness matrix obtained for Case I under the isotropic assumption (Equations 4.15 and 4.14) with the ones derived under the anisotropic assumption (Equation 4.18). Since the RVE in Case I is isotropic, the $\boldsymbol{C}$ matrix components obtained from both assumptions should be consistent with each other. The result presented in Figure 5.6 agrees with the expectations.

The components of the anisotropic tangent stiffness matrix for RVE with horizontal ellipse particle are tracked over time and are plotted in Figure 5.7. No damage is allowed to occur in the RVE; thus, it is clear that $\boldsymbol{C}$ matrix components remain constant over time. In the case of growing damage in the RVE, the components of $\boldsymbol{C}$ matrix reduce possibly in different rates, depending on the orientation of microcracks. Also, as shown in Figure 5.7, the proposed approach can correctly capture the anisotropy resulting from the anisotropic microstructure.

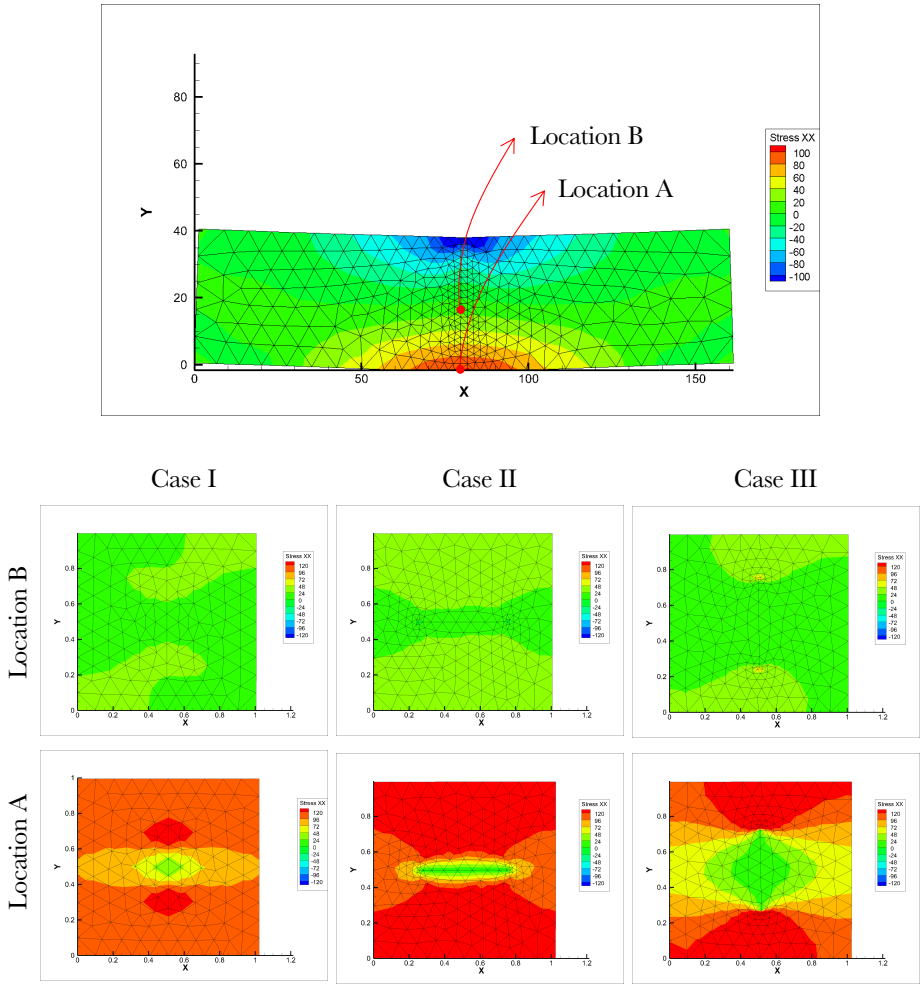

Figure 5.4: Three-point bending multiscale model result (no damage allowed in the RVE).

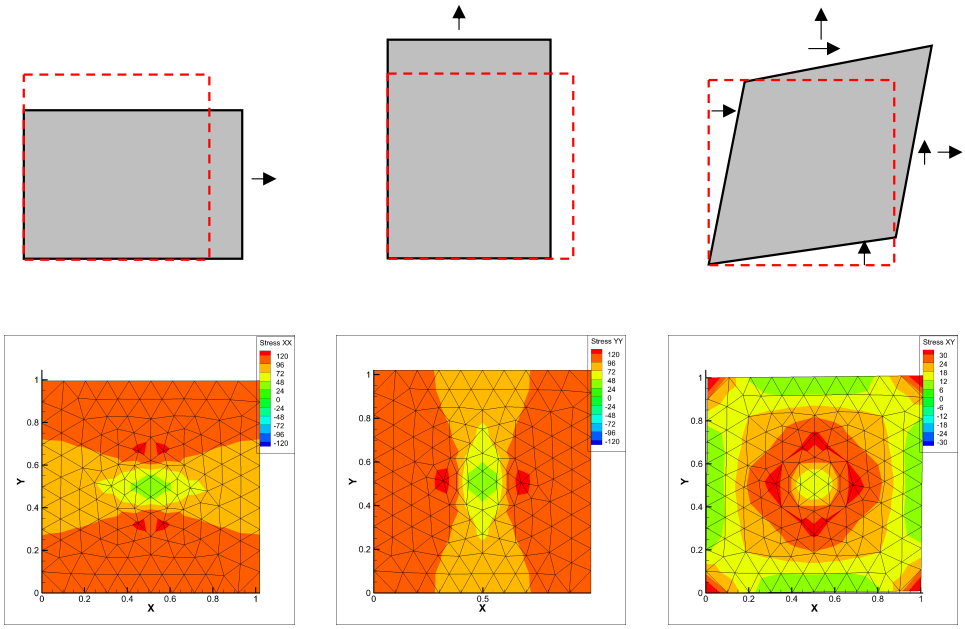

(a) (b) (c)

Figure 5.5: RVE with circular particle under: (a) uniaxial tension in the x-direction; (b) uniaxial tension in the y-direction; (c) pure shear (no damage allowed in the RVE).

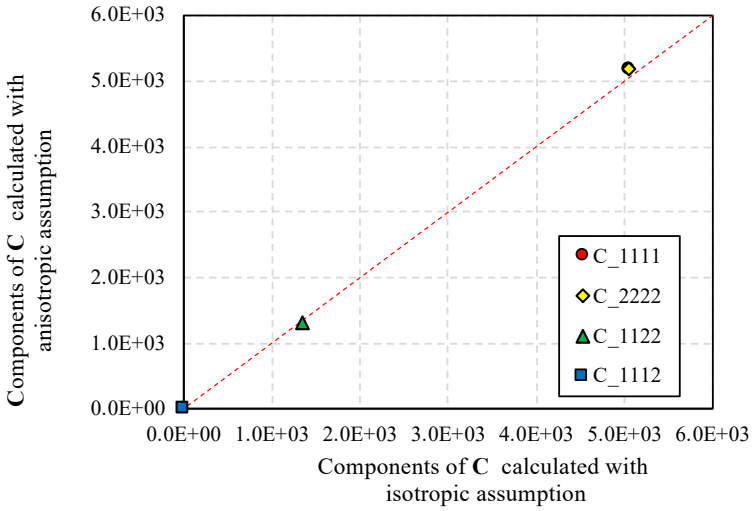

Figure 5.6: Components of $\boldsymbol{C}$ matrix for RVE with a circular particle obtained based on isotropic and anisotropic assumptions.

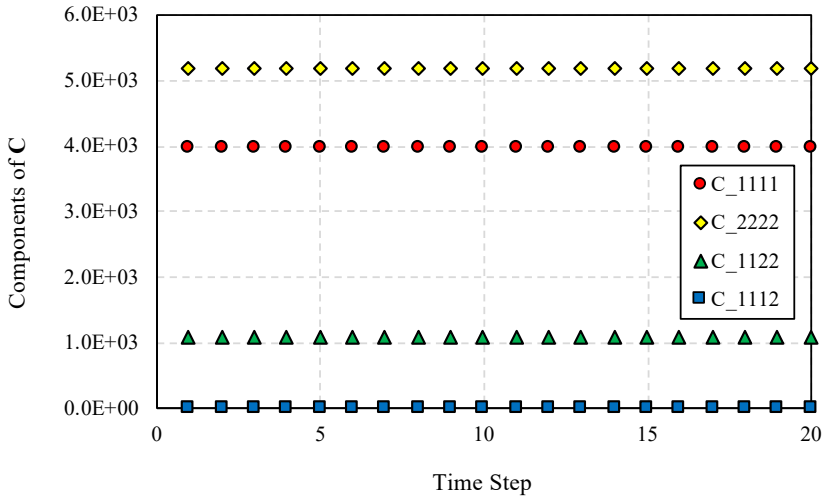

Figure 5.7: Components of $\boldsymbol{C}$ matrix for RVE with a horizontal ellipse particle.

Bifurcation analysis has been widely used to predict strain localization [Bigoni and Hueckel, 1991]. Following the idea of strain localization discussed in section 3.2, the localization criterion is equivalent to the determinant of the acoustic tensor being zero. The singularity of the acoustic tensor significantly depends on the homogenized constitutive model, which is determined from the response of an RVE. For cases where no damage is allowed in the RVE to initiate a weak discontinuity band, the determinant of $\boldsymbol{Q}$ remains constant with time. However, the bifurcation analysis can still be used to determine the critical angle that corresponds to the minimum value of the $Det(\boldsymbol{Q})$. The relationship between the computed determinant of the acoustic tensor and the angle that the unit normal vector of a potential weak discontinuity surface makes with the x-axis, α, is given in Figure 5.8. The $Det(\boldsymbol{Q})$ obtained from Case I is nearly constant with respect to α, while those obtained from Case II and Case III vary. The minimum value of $Det(\boldsymbol{Q})$ is found where there is a weak axis in the RVE. For example, for Case II, the minimum value at $\alpha = 0$ indicates that the RVE possesses a weak surface that is oriented along the y-axis.

5.3 Analyzing RVE with Damage

In order to show the capabilities of the proposed approach for simulating crack propagation in heterogeneous materials, a three-point bending test was simulated using the multiscale approach in which the midline elements of the beam were linked to an RVE consisting of one circular particle. This model is identical to model Case I defined previously except formation of microcracks is allowed within the RVE, which is simulated by the cohesive zone model. The cohesive zone interface elements are introduced everywhere in the matrix phase and along the boundary of the particle.

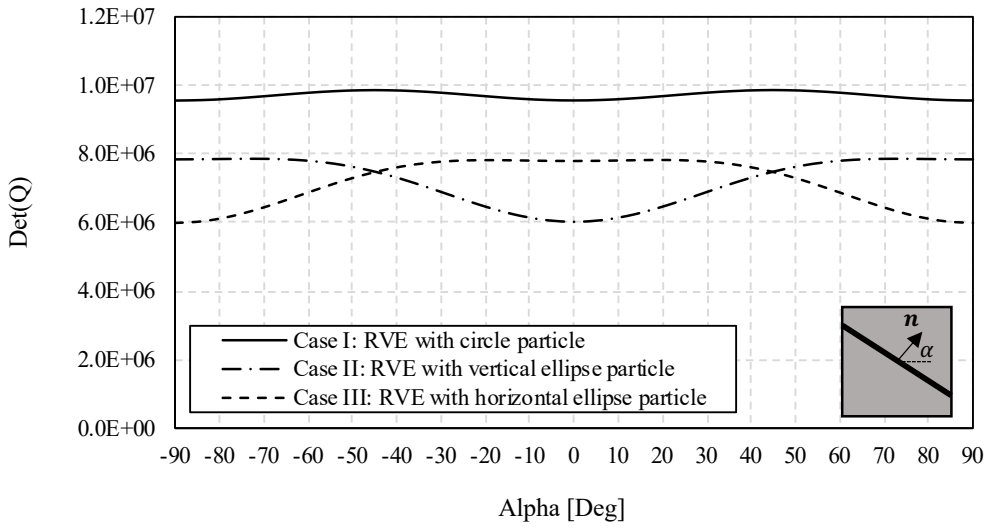

Figure 5.8: Determinant of acoustic tensor, $\boldsymbol{Q}$, versus potential weak discontinuity band orientation.

This model is intended for illustrative purposes and not for replicating a specific material behavior; thus, the material properties are selected arbitrarily. The material constitutive properties used to define the local-scale are presented in Table 5.2.

At each time step, global-scale IBVP is solved in order to obtain the stress and strain throughout the beam. For each global-scale element that is linked to an RVE, the calculated strain is applied to the corresponding RVE in the form of uniform displacement BC. The resulting stress contour plots of global-scale and local-scale models are shown in Figure 5.9. Snapshots of the RVE at selected times at two different locations along the midline of the beam are presented in Figure 5.9. Considering the loading condition of the global-scale model, the RVE linked to location A experienced higher tensile strain and hence it failed earlier than the RVE linked to location B. At time step 24, the RVE A had the highest stress, yet no microcrack formed. At time step 34, some microcracks were formed, which resulted in reduction of the

Table 5.2: Material properties of local-scale RVE.

Particle			
Elastic properties:			
$E = 2000$ (MPa)	$\nu = 0.2$		
Matrix			
Elastic properties:			
$E = 5000$ (MPa)	$\nu = 0.2$		
Cohesive zone viscoelastic properties (in Prony series):			
$E_\infty = 5000$ (MPa)	$E_1 = 5000$ (MPa)	$\rho_1 = 1$ s	$\nu = 0.2$
$\delta_s^* = 1.0$	$\delta_t^* = 1.0$		
$\sigma_s^f = 0.0$	$\sigma_t^f = 0.0$		
$A = 2.0$	$m = 0.2$		

overall stress of the RVE. At time step 38, the RVE linked to location A was severely damaged such that the failure criterion was met. Failure of an RVE is reflected to the global-scale model by elimination of the corresponding element. Removing the failed element from the global-scale changed the response of the beam that can be seen in the load-displacement curve shown in Figure 5.10. The red dashed line indicates the moment (time step 39) at which the RVE A failed. At time step 46, six additional elements also failed at the same time. It was assumed that failure of those elements is equivalent to the failure of the beam, hence the simulation was stopped. Assessing the failure of RVE A was obtained through the bifurcation analysis, which is discussed in the next section by analyzing the behavior of $\boldsymbol{C}$ and $Det(\boldsymbol{Q})$.

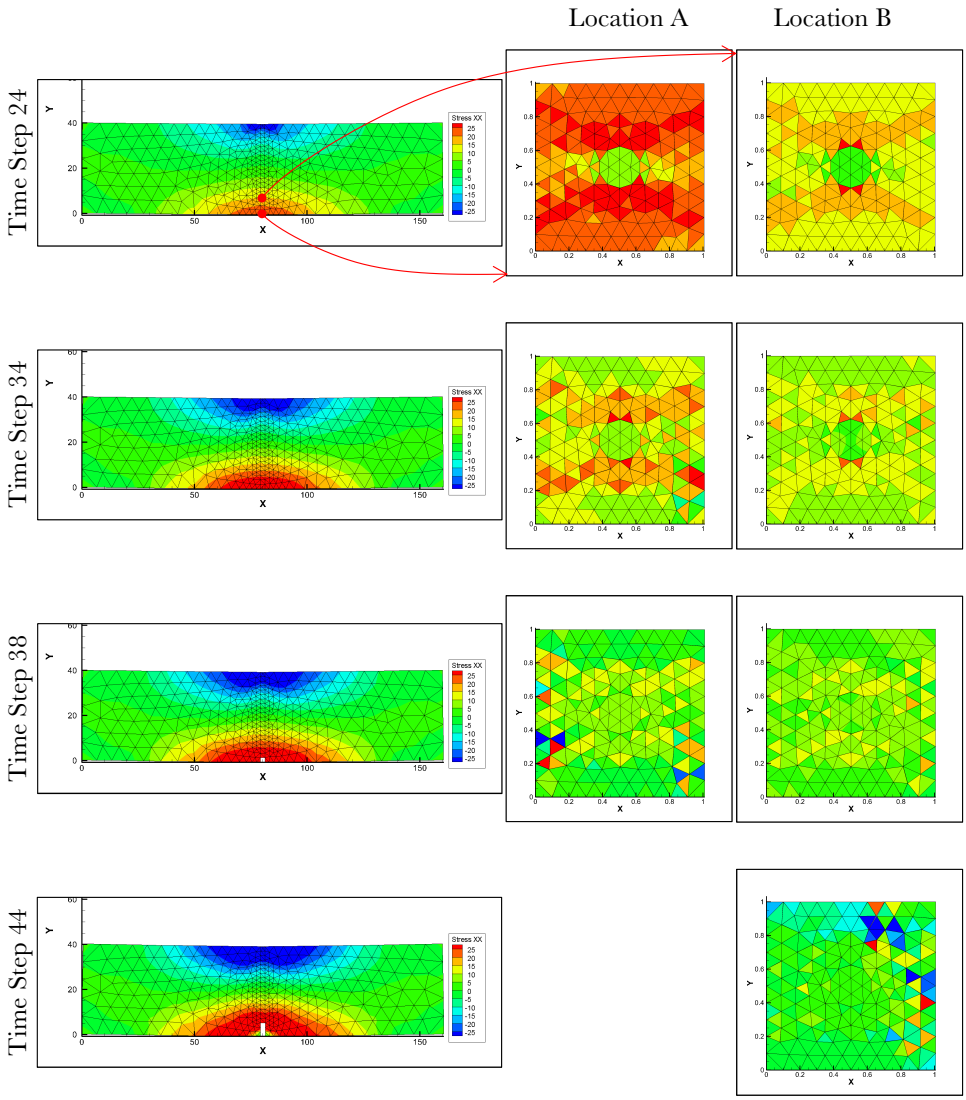

Figure 5.9: Three-point bending test multiscale simulation result (damage is allowed in RVE).

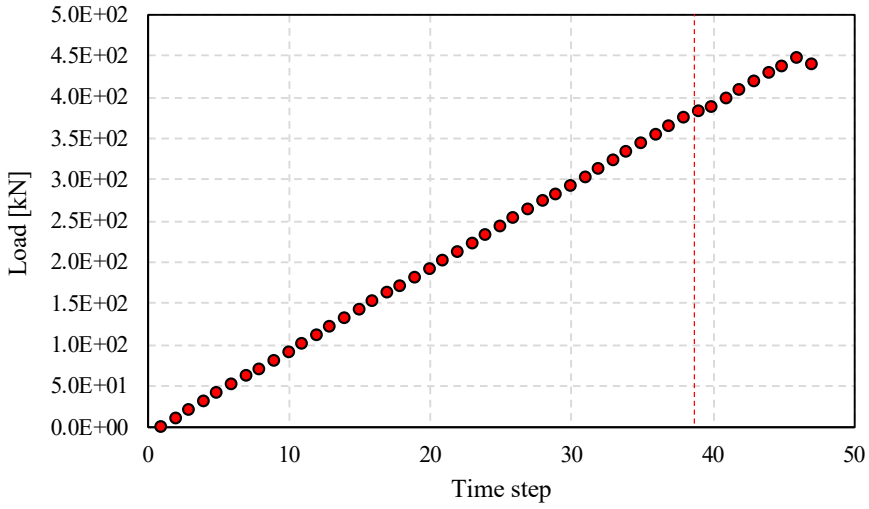

Figure 5.10: Load-displacement curve for three-point bending test multiscale simulation.

The evolution of the components of tangent stiffness tensor, C_{1111} and C_{2222}, with respect to time step are shown in Figure 5.11, which shows the effect of accumulated damage on tangent stiffness reduction. C_{1111} and C_{2222} decreased gradually then dropped quickly at time step 35. This gradual decrease was due to the effect of pre-failure softening behavior of cohesive zones, while the sharp drop occurred when a number of the cohesive elements failed, which created internal free surfaces within the RVE. The formation of an internal boundary causes an increase in the averaged strain (Equation 3.8) which results in decrease in homogenized stiffness. Since the RVE was initially isotropic, C_{1111} and C_{2222} were equal at the early stages of loading. But, as the loading increased, the discrepancy between the C_{1111} and C_{2222} was magnified, which corresponds to the anisotropic development of damage. At location A, σ_{11} was dominant, so damage grew faster in the direction perpendicular to the highest principal stress. Consequently, the reduction of C_{1111} was faster as compared to C_{2222}.

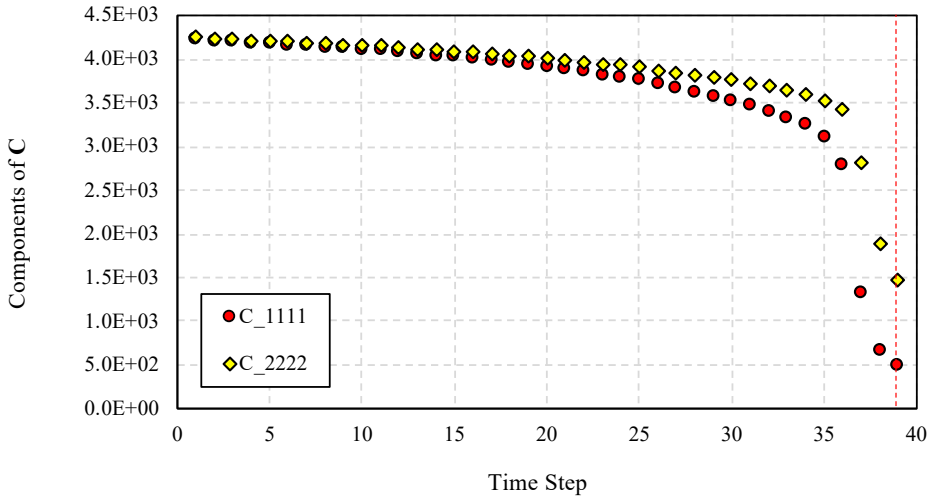

Figure 5.11: Components of tangent stiffness matrix of RVE at location A over time.

In order to study the performance of bifurcation analysis, the determinant of the acoustic tensor is plotted as a function of potential weak discontinuity surface orientation for different time steps, as shown in Figure 5.12. This determinant function is used to identify the onset of strain localization. When the acoustic tensor becomes non-positive definite for a certain direction, strain localization takes place in the RVE.

As the load increases, the cohesive zone elements expand and energy dissipates, and therefore damage accumulates. As damage accumulates, the stiffness of the RVE reduces, and as more damage occurs perpendicular to the loading axis, the tangent stiffness tensor, which was initially symmetrical, becomes asymmetrical. In this example, the cohesive damage variables developed faster in the y-direction, hence the localization zone formed vertically and the material was subjected to a mode I failure. Figure 5.12 shows how the changes in stiffness tensor make $Det(\boldsymbol{Q})$ at $\alpha = 0$ close to zero with time. It is worth mentioning that if the primary stress direction at location A in the global-scale changes, new microcracks develop in a different direction

and, consequently, the shape of $Det(\boldsymbol{Q})$ changes because the tangent stiffness tensor is altered.

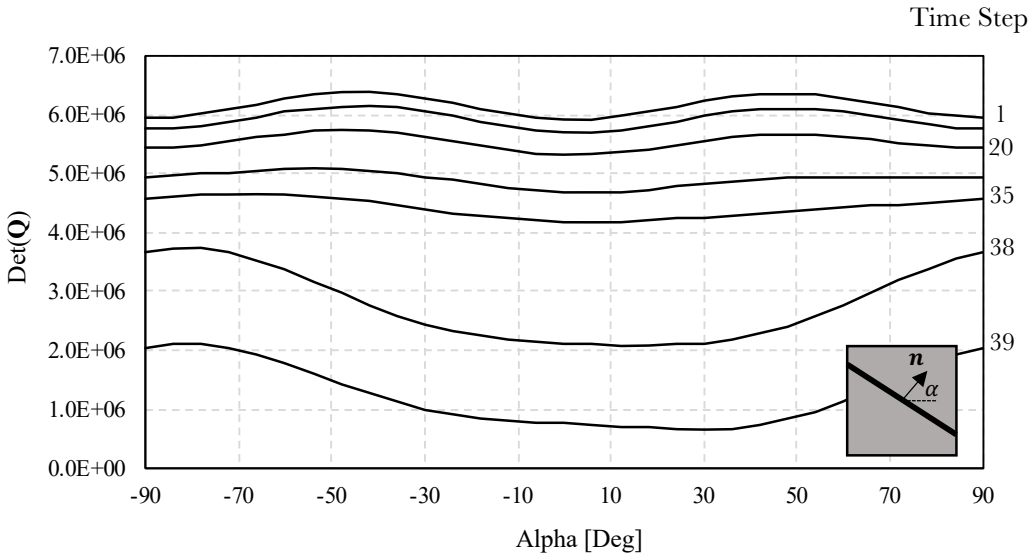

Figure 5.12: Determinant of acoustic tensor, $\boldsymbol{Q}$, versus potential weak discontinuity band orientation.

In the next example, the proposed multiscale method is further demonstrated by a two-way linked multiscale model where its RVE has a more complex microstructure. The global-scale model is the same as the one used in previous examples, while the local-scale RVE is composed of randomly embedded particles in an isotropic matrix. The RVE is a 2D representation of unidirectional fiber-reinforced composite in direction transverse to the fiber orientation. The fiber volume fraction is 55%, as shown in Figure 5.13.

Since the RVE represents a random heterogenous microstructure, the RVE size must be determined first. The minimum RVE size depends on the property of interest that is measured. A common practice is to plot the quantity of interest with respect to the RVE size. The size at which the quantity does not show a significant variation is

regarded as the minimum required RVE size. From the computational point of view, the RVE should not be larger than the optimum size in order to prevent redundant calculations from being performed [Gitman et al., 2007, Kim et al., 2009, Nguyen et al., 2010]. To obtain the average stiffness of RVE, a simple tension test simulation was performed on four square trial RVEs with increasing size. The FE model of RVEs were obtained from the cross-sectional image of a fiber-reinforced composite (Figure 5.13). The average stiffness is plotted as a function of trial RVE size in Figure 5.14. By comparing the four different RVE, the 30 $\mu m \times 30$ μm RVE is assumed to be large enough to be representative of the composite and used for multiscale simulations.

The multiscale modeling approach requires only the mechanical properties of RVE components as model inputs. In this study, the mechanical properties include elastic properties of the individual phases and fracture properties of matrix phases, which is subjected to cracking. These properties can be either obtained directly from experimental tests or back-calculated through a calibration process, however, they were arbitrarily assumed for the purpose of this example. The material properties are presented in Table 5.3. To reduce the modeling complexity at this stage, two assumptions were made. First, microcracks nucleate and propagate only within the matrix and along the boundaries between matrix and fibers in the RVE. Second, cohesive fracture within the matrix was assumed to be the same as the adhesive fracture between the matrix and fibers.

Table 5.3: Material properties of local-scale RVE of composite.

Fiber	
Elastic properties:	
$E = 5000$ (MPa)	$\nu = 0.2$
Matrix	
Elastic properties:	
$E = 2000$ (MPa)	$\nu = 0.2$
Cohesive zone viscoelastic properties (in Prony series):	
$E_\infty = 2000$ (MPa)	$E_1 = 2000$ (MPa) $\quad \rho_1 = 1$ s $\quad \nu = 0.2$
$\delta_s^* = 0.5$	$\delta_t^* = 0.5$
$\sigma_s^f = 0.0$	$\sigma_t^f = 0.0$
$A = 2.0$	$m = 0.2$

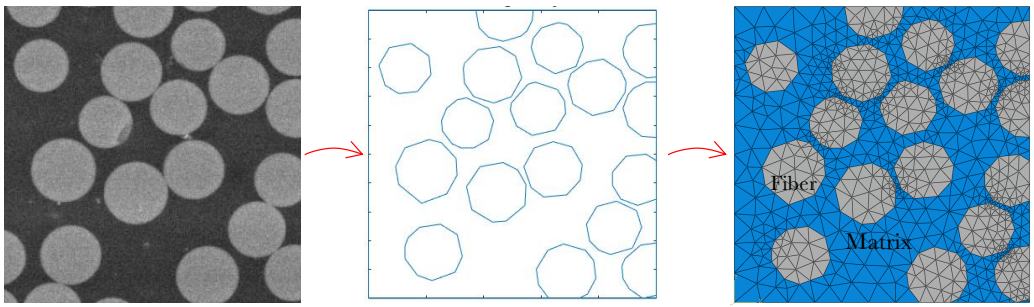

Figure 5.13: Obtaining FE model of RVE: (a) cross-sectional image of composite; (b) microstructure geometry; (c) FE model.

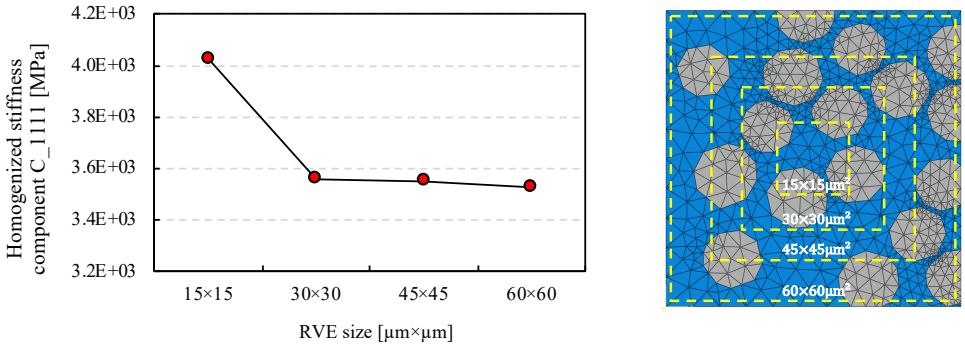

Figure 5.14: RVE size investigation.

In this example, the three-point bending beam, which is the global-scale model, was discretized using linear triangle elements. Based on physical observations from the specimens tested, it was reasonably assumed that the crack nucleates and propagates only through the vertical midline of the beam, while development of damage in other parts of the beam was neglected. For the areas without damage, the properties of global-scale element were obtained through a hierarchical multiscale method in which the response of RVE is homogenized once. The homogenized stiffness was calculated over the RVE which underwent a uniaxial tension test while no microcrack was allowed to form. On the other hand, the elements of vertical midline along the potential crack zone (the red zone in Figure 5.15) were linked to the RVE in two-way linked multiscale manner. The two-way linked multiscale method allows for stiffness reduction due to microcracking in RVE, which is consequently reflected in the form of stiffness reduction of the corresponding global-scale elements. Since each global-scale element experiences a unique loading history, each element is linked to its exclusive RVE. Hence, the number of global-scale elements that are linked to RVE significantly affects the computational efficiency of the two-way linked multiscale approach. In

this example, the number of elements linked to local-scale RVEs were limited to 4 elements (the red zone in Figure 5.15) that are critical in failure of the global-scale model.

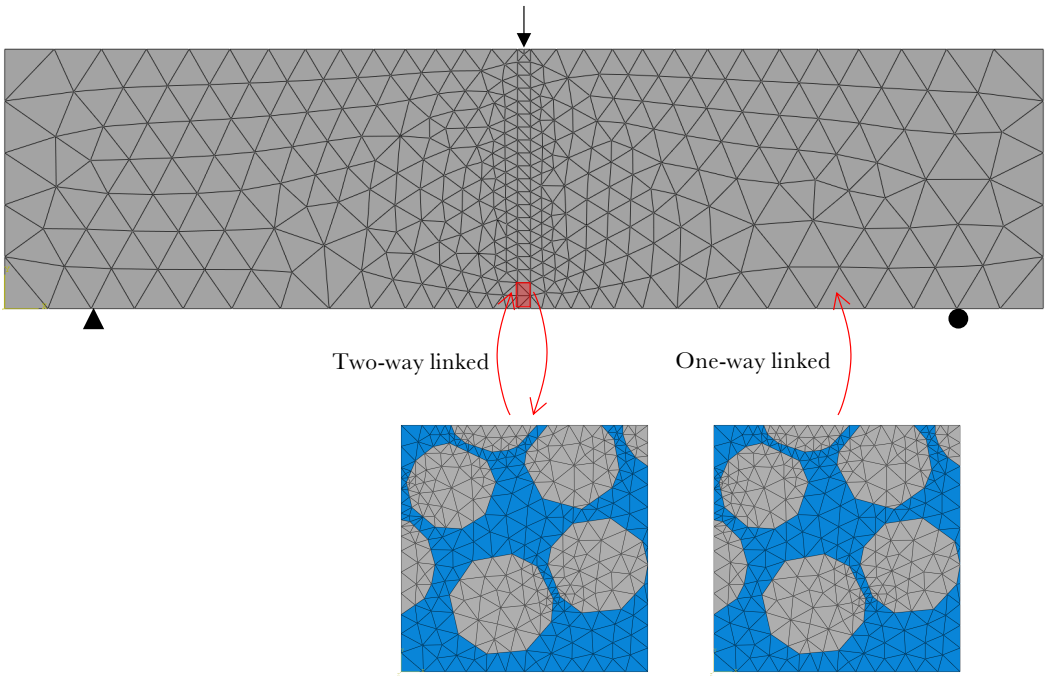

Figure 5.15: A sketch of the two-way linked multiscale model of the three-point bending test.

Simulation results are represented in the form of contours of horizontal component of stress, σ_{11}, for both global-scale beam specimen and local-scale RVE at three different stages (time step 18, 28, and 38), as shown in Figure 5.16. Local-scale plots represents the status of the RVE linked to the critical location at the global-scale model which has the highest tensile stress. At each time step the strain of global-scale element is converted to uniform displacement boundary condition and applied to the local-scale RVE (global-to-local linking), and cracking in the RVE due to progressive

loading is homogenized to update the effective properties of the global-scale element (local-to-global linking). When a cohesive zone opening reaches the critical opening displacement, a crack develops fully, and an internal boundary creates. Creation of internal boundaries results in loss of effective stiffness of an RVE. As the simulation continues, more microcracks develop in RVE until the determinant of acoustic tensor reaches a value close to zero which is assumed to be equivalent to crack initiation in the global-scale model (Figure 5.17).

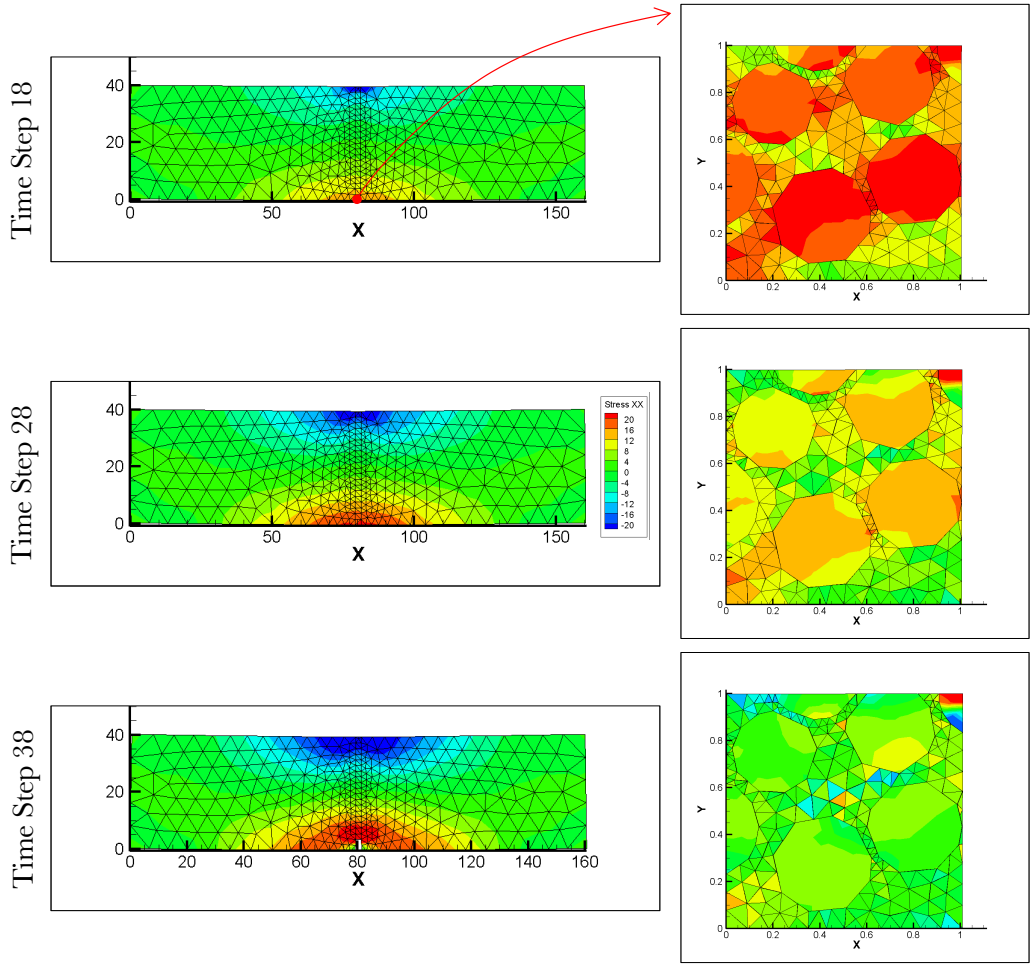

Figure 5.16: Three-point bending test multiscale simulation result.

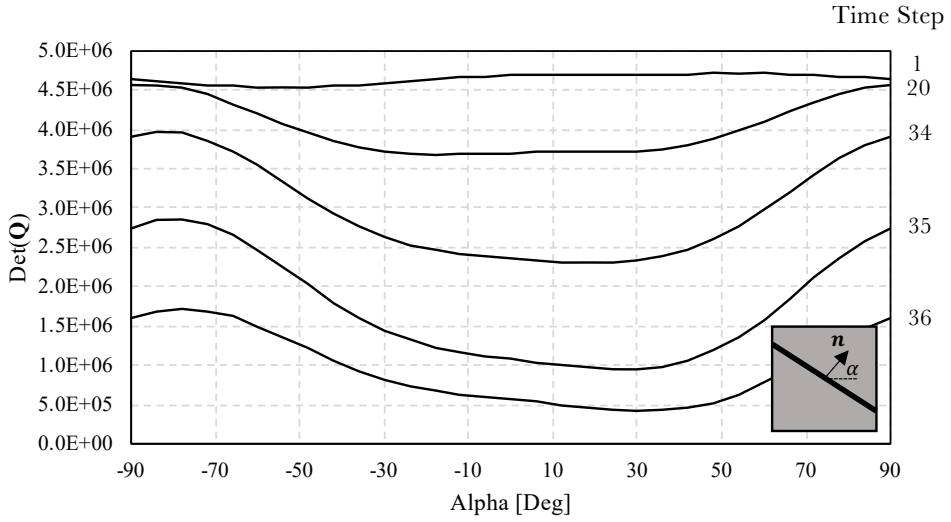

Figure 5.17: Determinant of acoustic tensor, $\boldsymbol{Q}$, versus potential weak discontinuity band orientation.

In this section the effect of material properties of local-scale model on the global-scale structural performance were investigated. For illustration purpose, the damage evolution factor in Equation 3.35, A, was varied while other material properties were kept constant. Figure 5.18 shows how C_{1111} component of homogenized tangent stiffness of each RVE changed with time. The slope of this curve shows how brittle or ductile the material is. The graph demonstrates that this material is brittle. Homogenized stiffness tends to drop sooner when the damage evolution factor is higher. The link between RVE to global-scale model through homogenization ensures that a change in local-scale properties affects the overall global-scale response. Figure 5.19 shows the load–displacement curve of the global-scale beam. In this particular example, the load–displacement curves evolved similarly up to the point when the beam started to fail, however, the failure loads were different. For instance, reducing A from 2.0 to 1.5, caused 25% increase in the maximum load.

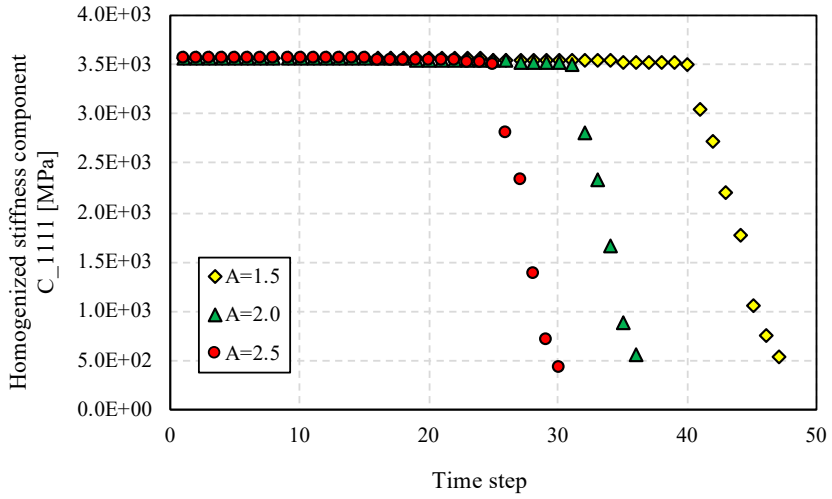

Figure 5.18: Homogenized tangent stiffness matrix component, C_{1111}, of RVE.

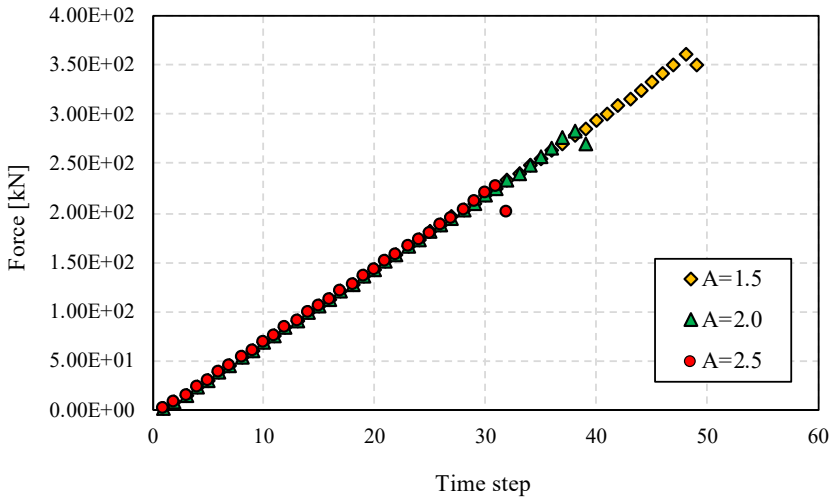

Figure 5.19: Load–displacement curve for three-point bending test multiscale simulation.

Chapter 6

Conclusions and Recommendations

6.1 Concluding Remarks

The macroscopic behavior of heterogeneous materials is highly dependent on the microstructure and properties of different components of microscopic scale. The two-way linked multiscale approach was effectively used to simulate the behavior of heterogeneous materials while taking into account the microscopic details of the material. The aim of this dissertation is to develop and implement algorithms to account for localization of RVE and then reflecting it as a discontinuity on the macroscale model within a two-way linked multiscale framework for heterogeneous materials. In this approach, a macroscopic model (global-scale) with effective properties is linked to a heterogeneous RVE (local-scale). The RVE is allowed to develop microcracks, i.e. initiate and propagate, that is represented by the cohesive zone fracture model. Degradation of material due to growth in damage in the RVE is addressed as a reduction of components of tangent stiffness tensor. Accumulation of microcracks within the RVE may form the strain localization band that is assessed using bifurcation analysis.

Once an RVE is localized, a discontinuity is placed in the macroscopic model using the element elimination method. This approach was implemented in a multiscale FE FORTRAN code. The viability of the method was then demonstrated by simulating some example cases. The main contributions and findings of this research relative to previous works include:

- The homogenized anisotropic tangent stiffness tensor can be obtained at each time step by applying arbitrary normal and shear BC to the current stage of RVE. The anisotropy of the RVE can be induced by anisotropic microstructure of the original RVE, anisotropic microstructural evolution of the RVE due to growth of damage, or both.

- Weak discontinuity band within an RVE can be predicted by performing a bifurcation analysis on the homogenized anisotropic tangent stiffness tensor of the RVE.

- Localization of RVE can be successfully reflected on the macroscopic scale by eliminating the corresponding element from the solution.

It is expected that a successful two-way linked multiscale computational model such as the one proposed herein can be beneficial in the following scenarios:

- Despite the technological advances in material characterization at microscopic length scales, there are still limitations regarding experimental investigation of damage-related properties at very small length scales. This approach provides a numerical bridging between microscopic and macroscopic length scales that allows use of macroscopic testing results (which are usually feasible to obtain) to indirectly characterize smaller-scale properties.

- The proposed approach provides opportunities to investigate the effect of microscopic heterogeneity on the macroscopic performance of structures. Using this method, materials' microstructure and properties of microscopic components can be regarded as design variables in order to achieve better macroscopic performance.

6.2 Recommendations and Future Work

Although, the proposed method herein can simulate fracture within the heterogeneous material using the two-way linked multiscale approach, many additional improvements can be made. Some of these potential improvements are summarized below:

- The main objective of this research was to propose and implement an effective multiscale method for dealing with localized RVE in situations where standard homogenization methods fail. Although, the proposed method was demonstrated with several example problems, the validity of this method still needs to be investigated by simulating real-world problems; i.e., problems with true microstructure and material properties and comparing the results with experimental data.

- Localization of RVE is equivalent to the formation of strain weak discontinuity band on the global-scale; however, in this study, the localized RVE was replaced with a discrete fracture (strong discontinuity) on the global-scale. In a more rigorous approach, localization of RVE should be represented by inserting a weak discontinuity surface within the global-scale element.

- One of the main advantages of the multiscale approach as compared to direct numerical simulation (DNS) models is that a single scale large BVP with a large number of degrees of freedom (DOF) can be split into multiple BVPs with a significantly reduced number of DOF. In this case, higher computational efficiency can be achieved by employing parallel computing techniques that enable use of multiple CPUs simultaneously solve a number of local-scale BVPs.

- The code developed in this dissertation only allows linkage between global-scale elements to RVEs that possess an identical microstructure. This can be extended by linking each global-scale element to a different RVE, yet they all represent the same microstructure. This may be an interesting topic for future research, as it may capture random propagation path and branching of cracks that are usually observed in many real materials with random heterogeneity.

- The proposed method can be coupled with multiphysics aspects, such as thermal effects, in order to perform thermo-mechanical analysis. However, further investigation is needed to properly adjust the imposed boundary conditions on the RVE and the homogenization procedures.

Bibliography

[Aboudi et al., 2012] Aboudi, J., Arnold, S. M., and Bednarcyk, B. A. (2012). *Micromechanics of composite materials: a generalized multiscale analysis approach*. Butterworth-Heinemann.

[Akcaoglu et al., 2005] Akcaoglu, T., Tokyay, M., and Celik, T. (2005). Assessing the itz microcracking via scanning electron microscope and its effect on the failure behavior of concrete. *Cement and Concrete Research*, 35(2):358–363.

[Allen and Searcy, 2000] Allen, D. H. and Searcy, C. R. (2000). Numerical aspects of a micromechanical model of a cohesive zone. *Journal of Reinforced Plastics and Composites*, 19(3):240–248.

[Andersson, 1977] Andersson, H. (1977). Analysis of a model for void growth and coalescence ahead of a moving crack tip. *Journal of the Mechanics and Physics of Solids*, 25(3):217–233.

[Bazant and Oh, 1983] Bazant, Z. P. and Oh, B. H. (1983). Crack band theory for fracture of concrete. *Materiaux et construction*, 16(3):155–177.

[Belytschko et al., 2008] Belytschko, T., Loehnert, S., and Song, J.-H. (2008). Multiscale aggregating discontinuities: a method for circumventing loss of material

stability. *International Journal for Numerical Methods in Engineering*, 73(6):869–894.

[Belytschko and Song, 2010] Belytschko, T. and Song, J.-H. (2010). Coarse-graining of multiscale crack propagation. *International journal for numerical methods in engineering*, 81(5):537–563.

[Beran, 1965] Beran, M. (1965). Statistical continuum theories. *Transactions of the Society of Rheology*, 9(1):339–355.

[Beran, 2001] Beran, M. (2001). Statistical continuum mechanics. In *Mechanics of Random and Multiscale Microstructures*, pages 1–31. Springer.

[Bigoni and Hueckel, 1991] Bigoni, D. and Hueckel, T. (1991). Uniqueness and localization—i. associative and non-associative elastoplasticity. *International Journal of Solids and structures*, 28(2):197–213.

[Broberg, 1997] Broberg, K. (1997). The cell model of materials. *Computational Mechanics*, 19(6):447–452.

[Budarapu and Rabczuk, 2017] Budarapu, P. and Rabczuk, T. (2017). Multiscale methods for fracture: A review. *Journal of the Indian Institute of Science*, 97(3):339–376.

[Christensen, 2012] Christensen, R. (2012). *Theory of viscoelasticity: an introduction*. Elsevier.

[Feyel and Chaboche, 2000] Feyel, F. and Chaboche, J.-L. (2000). Fe2 multiscale approach for modelling the elastoviscoplastic behaviour of long fibre sic/ti composite

materials. *Computer methods in applied mechanics and engineering*, 183(3-4):309–330.

[Geers et al., 2010] Geers, M. G., Kouznetsova, V. G., and Brekelmans, W. (2010). Multi-scale computational homogenization: Trends and challenges. *Journal of computational and applied mathematics*, 234(7):2175–2182.

[Gitman et al., 2007] Gitman, I., Askes, H., and Sluys, L. (2007). Representative volume: existence and size determination. *Engineering fracture mechanics*, 74(16):2518–2534.

[Hashin, 1983] Hashin, Z. (1983). Analysis of composite materials—a survey. *Journal of Applied Mechanics*, 50(3):481–505.

[Hill, 1972] Hill, R. (1972). On constitutive macro-variables for heterogeneous solids at finite strain. *Proc. R. Soc. Lond. A*, 326(1565):131–147.

[Hori and Nemat-Nasser, 1999] Hori, M. and Nemat-Nasser, S. (1999). On two micromechanics theories for determining micro–macro relations in heterogeneous solids. *Mechanics of Materials*, 31(10):667–682.

[Inglis et al., 2008] Inglis, H. M., Geubelle, P. H., and Matous, K. (2008). Boundary condition effects on multiscale analysis of damage localization. *Philosophical Magazine*, 88(16):2373–2397.

[Jirasek, 2007] Jirasek, M. (2007). Mathematical analysis of strain localization. *Revue europeenne de genie civil*, 11(7-8):977–991.

[Johnson et al., 2005] Johnson, P. R., Petrinic, N., and Süli, E. (2005). Element-splitting for simulation of fracture in 3d solid continua. *Computational Plasticity*

VIII, Fundamentals and Applications, Owen, DRJ, Oñate, E., Suarez, B.(Eds.), Part, 1:507–512.

[Karamnejad, 2016] Karamnejad, A. (2016). Multiscale computational modeling of brittle and ductile materials under dynamic loading.

[Karamnejad et al., 2017] Karamnejad, A., Ahmed, A., and Sluys, L. J. (2017). A numerical homogenization scheme for glass particle-toughened polymers under dynamic loading. *Journal of Multiscale Modelling*, 8(01):1750001.

[Karamnejad and Sluys, 2015] Karamnejad, A. and Sluys, L. (2015). A multi-scale scheme for modelling fracture under dynamic loading conditions. In *Key Engineering Materials*, volume 627, pages 37–40. Trans Tech Publ.

[Karamnejad and Sluys, 2014] Karamnejad, A. and Sluys, L. J. (2014). A dispersive multi-scale crack model for quasi-brittle heterogeneous materials under impact loading. *Computer Methods in Applied Mechanics and Engineering*, 278:423–444.

[Kim, 2011] Kim, Y.-R. (2011). Cohesive zone model to predict fracture in bituminous materials and asphaltic pavements: state-of-the-art review. *International Journal of Pavement Engineering*, 12(4):343–356.

[Kim et al., 2009] Kim, Y.-R., Lutif, J., and Allen, D. (2009). Determining representative volume elements of asphalt concrete mixtures without damage. *Transportation Research Record: Journal of the Transportation Research Board*, (2127):52–59.

[Kim et al., 2013] Kim, Y.-R., Souza, F. V., and Teixeira, J. E. S. L. (2013). A two-way coupled multiscale model for predicting damage-associated performance of asphaltic roadways. *Computational Mechanics*, 51(2):187–201.

[Kouznetsova et al., 2002] Kouznetsova, V., Geers, M. G., and Brekelmans, W. M. (2002). Multi-scale constitutive modelling of heterogeneous materials with a gradient-enhanced computational homogenization scheme. *International Journal for Numerical Methods in Engineering*, 54(8):1235–1260.

[Kroner, 1972] Kroner, E. (1972). *Statistical continuum mechanics*. Number 92. Springer.

[Lee et al., 2009] Lee, H., Choi, J., Jung, K., and Im, Y.-T. (2009). Application of element deletion method for numerical analyses of cracking. *Journal of Achievements in Materials and Manufacturing Engineering*, 35(2):154–161.

[Leon et al., 2014] Leon, S., Spring, D., and Paulino, G. (2014). Reduction in mesh bias for dynamic fracture using adaptive splitting of polygonal finite elements. *International Journal for Numerical Methods in Engineering*, 100(8):555–576.

[Liu and Sherman, 1976] Liu, W.-H. and Sherman, A. H. (1976). Comparative analysis of the cuthill–mckee and the reverse cuthill–mckee ordering algorithms for sparse matrices. *SIAM Journal on Numerical Analysis*, 13(2):198–213.

[Loehnert and Belytschko, 2007] Loehnert, S. and Belytschko, T. (2007). A multiscale projection method for macro/microcrack simulations. *International Journal for Numerical Methods in Engineering*, 71(12):1466–1482.

[Massart et al., 2007] Massart, T., Peerlings, R., and Geers, M. (2007). An enhanced multi-scale approach for masonry wall computations with localization of damage. *International journal for numerical methods in engineering*, 69(5):1022–1059.

[Mishnaevsky Jr et al., 1998] Mishnaevsky Jr, L., Mintchev, O., and Schmauder, S. (1998). Fe-simulation of crack growth using damage parameter and cohesive surface concept. In *ECF12, Sheffield 1998*.

[Mishnaevsky Jr, 2007] Mishnaevsky Jr, L. L. (2007). *Computational mesomechanics of composites: numerical analysis of the effect of microstructures of composites of strength and damage resistance*. John Wiley & Sons.

[Moorthy and Ghosh, 1998] Moorthy, S. and Ghosh, S. (1998). A voronoi cell finite element model for particle cracking in elastic-plastic composite materials. *Computer methods in applied mechanics and engineering*, 151(3-4):377–400.

[Nemat-Nasser and Hori, 2013] Nemat-Nasser, S. and Hori, M. (2013). *Micromechanics: overall properties of heterogeneous materials*, volume 37. Elsevier.

[Nguyen et al., 2010] Nguyen, V. P., Lloberas-Valls, O., Stroeven, M., and Sluys, L. J. (2010). On the existence of representative volumes for softening quasi-brittle materials–a failure zone averaging scheme. *Computer Methods in Applied Mechanics and Engineering*, 199(45-48):3028–3038.

[Nguyen et al., 2011] Nguyen, V. P., Lloberas-Valls, O., Stroeven, M., and Sluys, L. J. (2011). Homogenization-based multiscale crack modelling: from micro-diffusive damage to macro-cracks. *Computer Methods in Applied Mechanics and Engineering*, 200(9-12):1220–1236.

[Nguyen et al., 2012a] Nguyen, V. P., Lloberas-Valls, O., Stroeven, M., and Sluys, L. J. (2012a). Computational homogenization for multiscale crack modeling. implementational and computational aspects. *International Journal for Numerical Methods in Engineering*, 89(2):192–226.

[Nguyen et al., 2012b] Nguyen, V. P., Stroeven, M., and Sluys, L. J. (2012b). An enhanced continuous–discontinuous multiscale method for modeling mode-i cohesive failure in random heterogeneous quasi-brittle materials. *Engineering Fracture Mechanics*, 79:78–102.

[Nguyen et al., 2012c] Nguyen, V. P., Stroeven, M., and Sluys, L. J. (2012c). Multiscale failure modeling of concrete: micromechanical modeling, discontinuous homogenization and parallel computations. *Computer Methods in Applied Mechanics and Engineering*, 201:139–156.

[Oliver, 1995] Oliver, J. (1995). Continuum modelling of strong discontinuities in solid mechanics using damage models. *Computational Mechanics*, 17(1-2):49–61.

[Oliver et al., 2014] Oliver, J., Caicedo, M., Roubin, E., Hernandez, J., and Huespe, A. (2014). Multi-scale (fe2) analysis of material failure in cement/aggregate-type composite structures. *Computational Modelling of Concrete Structures p*, 39.

[Oliver et al., 2015] Oliver, J., Caicedo, M., Roubin, E., Huespe, A. E., and Hernandez, J. (2015). Continuum approach to computational multiscale modeling of propagating fracture. *Computer Methods in Applied Mechanics and Engineering*, 294:384–427.

[Ozdemir et al., 2008] Ozdemir, I., Brekelmans, W., and Geers, M. G. (2008). Fe2 computational homogenization for the thermo-mechanical analysis of heterogeneous solids. *Computer Methods in Applied Mechanics and Engineering*, 198(3-4):602–613.

[Qin and Yang, 2008] Qin, Q.-H. and Yang, Q.-S. (2008). *Macro-micro theory on multi-field coupling behavior of heterogeneous materials*. Springer,.

[Rami et al., 2017] Rami, K. Z., Amelian, S., Kim, Y.-R., You, T., and Little, D. N. (2017). Modeling the 3d fracture-associated behavior of viscoelastic asphalt mixtures using 2d microstructures. *Engineering Fracture Mechanics*, 182:86–99.

[Rice and Tracey, 1969] Rice, J. R. and Tracey, D. M. (1969). On the ductile enlargement of voids in triaxial stress fields. *Journal of the Mechanics and Physics of Solids*, 17(3):201–217.

[Sanchez et al., 2013] Sanchez, P. J., Blanco, P. J., Huespe, A. E., and Feijoo, R. (2013). Failure-oriented multi-scale variational formulation: micro-structures with nucleation and evolution of softening bands. *Computer Methods in Applied Mechanics and Engineering*, 257:221–247.

[Searcy, 1998] Searcy, C. R. (1998). *A micromechanical model for a viscoelastic cohesive zone*. PhD thesis, Texas A&M University.

[Song and Belytschko, 2009] Song, J.-H. and Belytschko, T. (2009). Multiscale aggregating discontinuities method for micro-macro failure of composites. *Composites Part B: Engineering*, 40(6):417–426.

[Souza et al., 2008] Souza, F., Allen, D., and Kim, Y.-R. (2008). Multiscale model for predicting damage evolution in composites due to impact loading. *Composites science and technology*, 68(13):2624–2634.

[Souza and Allen, 2010] Souza, F. V. and Allen, D. H. (2010). Multiscale modeling of impact on heterogeneous viscoelastic solids containing evolving microcracks. *International Journal for Numerical Methods in Engineering*, 82(4):464–504.

[Souza and Allen, 2011] Souza, F. V. and Allen, D. H. (2011). Modeling the transition of microcracks into macrocracks in heterogeneous viscoelastic media using a two-

way coupled multiscale model. *International Journal of Solids and Structures*, 48(22-23):3160–3175.

[Toro et al., 2016] Toro, S., Sanchez, P. J., Blanco, P. J., de Souza Neto, E., Huespe, A. E., and Feijoo, R. (2016). Multiscale formulation for material failure accounting for cohesive cracks at the macro and micro scales. *International Journal of Plasticity*, 76:75–110.

[Toro et al., 2014] Toro, S., Sanchez, P. J., Huespe, A. E., Giusti, S. M., Blanco, P. J., and Feijoo, R. (2014). A two-scale failure model for heterogeneous materials: numerical implementation based on the finite element method. *International Journal for Numerical Methods in Engineering*, 97(5):313–351.

[Verhoosel et al., 2010a] Verhoosel, C. V., Remmers, J. J., and Gutiérrez, M. A. (2010a). A partition of unity-based multiscale approach for modelling fracture in piezoelectric ceramics. *International Journal for Numerical Methods in Engineering*, 82(8):966–994.

[Verhoosel et al., 2010b] Verhoosel, C. V., Remmers, J. J., Gutierrez, M. A., and De Borst, R. (2010b). Computational homogenization for adhesive and cohesive failure in quasi-brittle solids. *International Journal for Numerical Methods in Engineering*, 83(8-9):1155–1179.

[Wang et al., 2009] Wang, L., Zhao, N., and Ma, S. (2009). A simple element-splitting model to simulate the tensile fracture of brittle materials and its experimental verification. *Computational Materials Science*, 46(3):672–676.

[Wang et al., 2007] Wang, X., Wu, K., Huang, W., Zhang, H., Zheng, M., and Peng, D. (2007). Study on fracture behavior of particulate reinforced magnesium matrix

composite using in situ sem. *Composites Science and Technology*, 67(11-12):2253–2260.

[Weinberg, 2008] Weinberg, K. (2008). Material modeling of microstructured solids—theory, numeric and applications—.

[Xia and Shih, 1995a] Xia, L. and Shih, C. F. (1995a). Ductile crack growth-i. a numerical study using computational cells with microstructurally-based length scales. *Journal of the Mechanics and Physics of Solids*, 43(2):233–259.

[Xia and Shih, 1995b] Xia, L. and Shih, C. F. (1995b). Ductile crack growth—ii. void nucleation and geometry effects on macroscopic fracture behavior. *Journal of the Mechanics and Physics of Solids*, 43(12):1953–1981.

[Xia and Shih, 1996] Xia, L. and Shih, C. F. (1996). Ductile crack growth—iii. transition to cleavage fracture incorporating statistics. *Journal of the Mechanics and Physics of Solids*, 44(4):603–639.

[Xia et al., 1995] Xia, L., Shih, C. F., and Hutchinson, J. W. (1995). A computational approach to ductile crack growth under large scale yielding conditions. *Journal of the Mechanics and Physics of Solids*, 43(3):389–413.

[Zare-Rami, 2018] Zare-Rami, K. (2018). Midas-vt preprocessor. `https://github.com/K1-ZR/midas-vt-pre`.

[Zare-Rami and Kim, 2019] Zare-Rami, K. and Kim, Y.-R. (2019). Midas-vt-pre: Software to generate 2d finite element model of particle/fiber embedded composites with cohesive zones. *SoftwareX*, 10:100292.

[Zocher et al., 1997] Zocher, M., Groves, S., and Allen, D. H. (1997). A three-dimensional finite element formulation for thermoviscoelastic orthotropic media. *International Journal for Numerical Methods in Engineering*, 40(12):2267–2288.

Appendix A

MIDAS-VT-Pre

A.1 Overview

MIDAS-VT-Pre, MIDAS-VT Preprocessor, is a part of MIDAS-VT, Microstructure Inelastic Damage Analysis Software-Virtual Tester, package that generates finite element model of common mechanical test settings. It is equipped with a unique meshing algorithm which inserts cohesive elements within a user-defined area. MIDAS-VT-Pre can be used to generate FE model of square RVEs. These RVE FE model can be used later in multiscale simulations involving progressive damage. The package is currently tailored to create microstructural FE model of two-phase materials. The overall flow of MIDAS-VT-Pre is shown in A.1. MIDAS-VT-Pre provides two options for the users:

- Case I: Generates the FE model directly from the RVE image or geometry
- Case II: Adds cohesive elements into FE mesh which is generated in advance

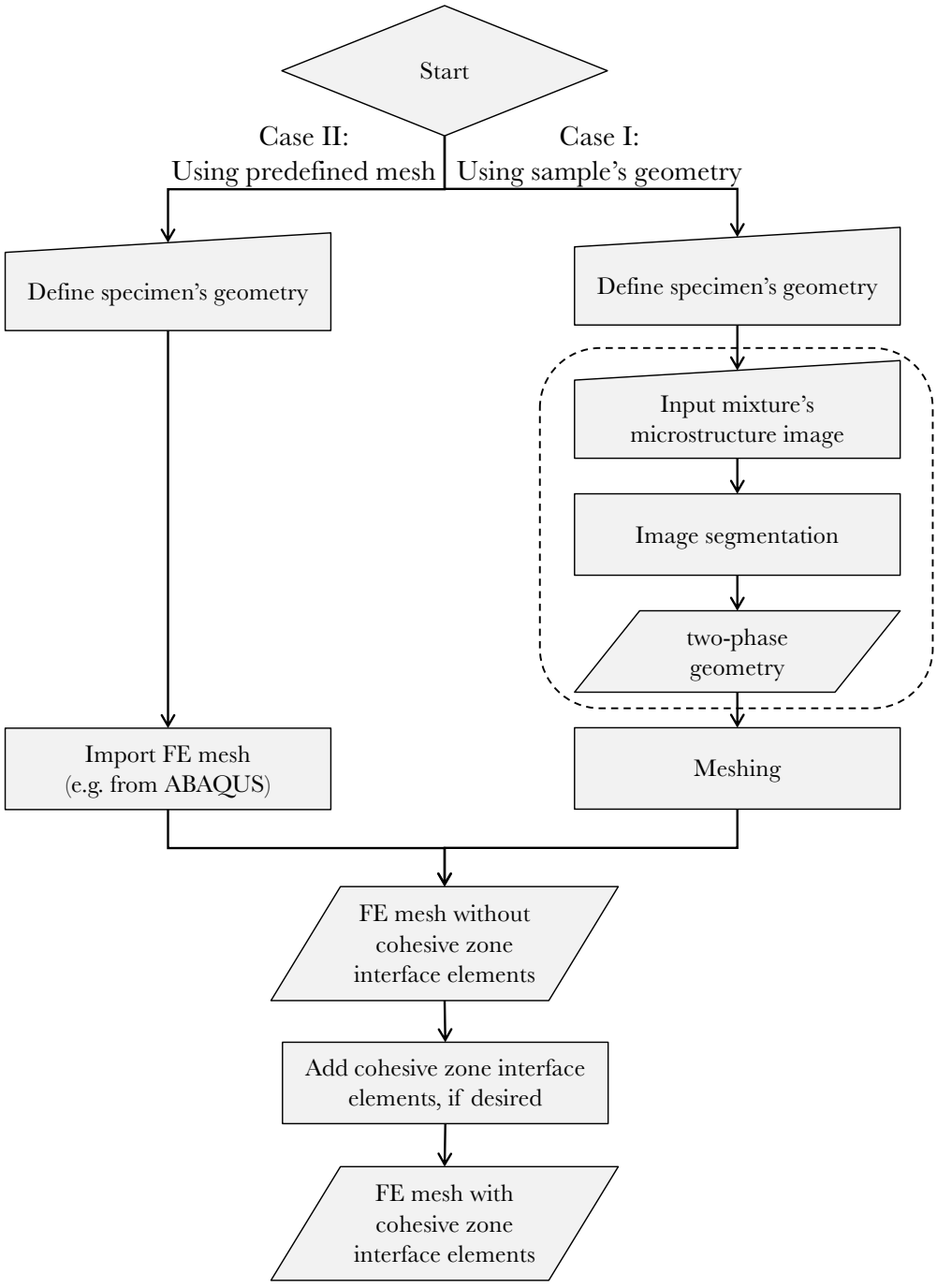

Figure A.1: Flowchart of MIDAS-VT-Pre.

A.2 Start MIDAS-VT-Pre

1. Package must have the following files:
    - MIDAS_VT_Pre.exe
    - Gallery folder
    - splash.PNG
2. Install the prerequisite:
    - 64-bit version of MATLAB Runtime version 9.5 (R2018b)
3. Run MIDAS_VT_Pre.exe

Note: all the output messages will be stored in STATUS.txt for future reference.
Note: The execution may take several minutes.

A.3 MIDAS-VT-Pre Description

MIDAS-VT-Pre starts with a pop-up window, Figure A.2, offering two options. The first option is used when the user is going to generate the FE model directly from the RVE image or geometry. This option corresponds to Case I in Figure A.1. The second option is used when the user is going to add cohesive elements into a regular FE mesh which is generated in advance. This option corresponds to Case II in Figure A.1.

A.3.1 Preprocessor Case I

Choosing Case I presented in Figure A.2, directs the user to the window shown in Figure A.3. There are four steps to generate the model:

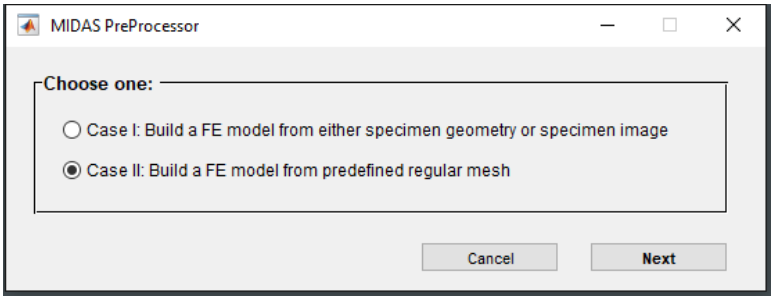

Figure A.2: MIDAS–VT–Pre starting window.

1. Specimen Geometry
2. Microstructure
3. Mesh
4. Export Output

For each section there are several inputs and actions required which are described bellow.

Specimen Geometry

At this panel, the user needs to select either *simple tension test* or *simple shear test* and provide the RVE dimensions.

Microstructure

MIDAS-VT-Pre is able to create either homogeneous (one-phase) or heterogenous (two-phase) models. In homogenous case, the software generates model geometry using RVE's dimensions provided in the first section. In the second case, a heterogenous material is defined as a two-phase material where non-contact random particles

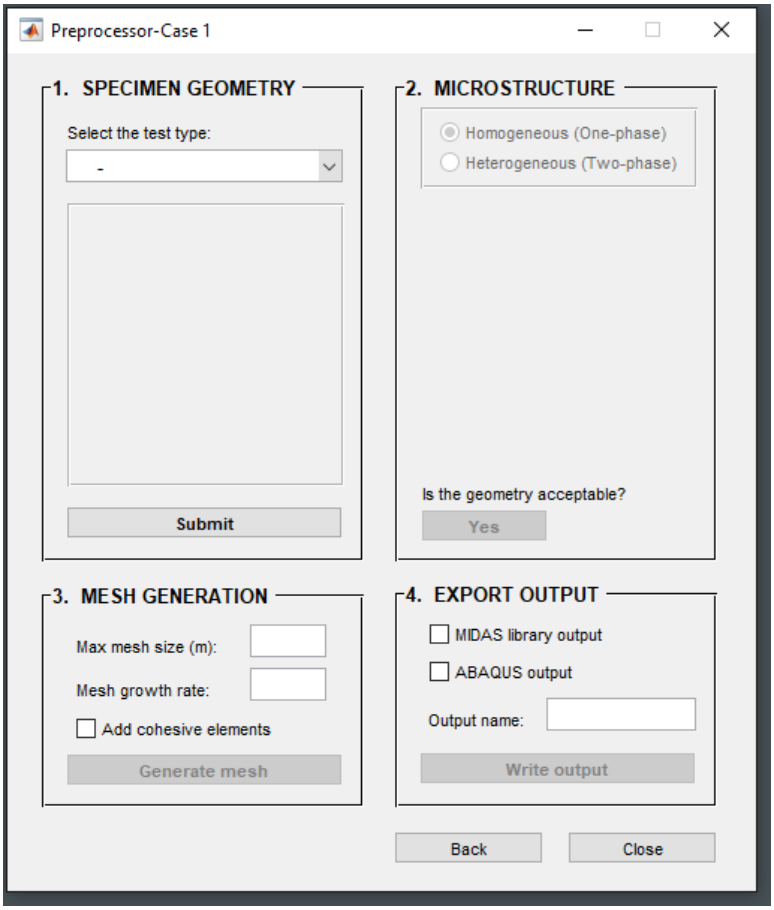

Figure A.3: MIDAS–VT–Pre Case I.

are scattered within a matrix phase. MIDAS-VT-Pre is equipped with an image-processing tool which obtains mixture's microstructure from the actual image of a RVE. The user needs to provide the software with the cross-section image of the RVE and follow the steps one to five in *image processing tool* shown in Figure A.4. In the cross-section image, particles must be lighter in color than the matrix background. MIDAS-VT-Pre uses color segmentation method to distinguish particles from matrix phase. *Color segmentation threshold* is a value between 0 to 1, which defines the boundary between particles (light color areas) and matrix phase (dark color areas). This value will be calculated automatically, however the user can adjust the value, if necessary. Also, *convexing factor* allows the user to adjust how particles' peripherals are being bounded. Setting convexing factor to 0 gives a convex hull around the particles while setting it to higher values gives a compact boundary around the particles (the default value is 0.2). The proper values of color segmentation threshold and convexing factor depends on the image and can be obtained by trial and error.

When the image segmentation process is done, the user can compare the result to the actual microstructure (Figure A.5). If the microstructure is similar enough to the original image, the user can approve the image segmentation result and go to the meshing step by clicking "Yes" button. If there are still mismatches that cannot be improved by changing color segmentation threshold and convexing factor, the user needs to modify the image manually. The manual image treatment is basically re-painting the indistinct areas or separating connected particles in the image. Modify particles or matrix areas should be done using a proper color of which lightness/darkness matches the average intensity of the corresponding area (particles or matrix). To facilitate the manual treatment procedure, Microsoft Paint software is integrated with MIDAS-VT-Pre. By clicking "No (redo)" button (Figure A.4) the original image will

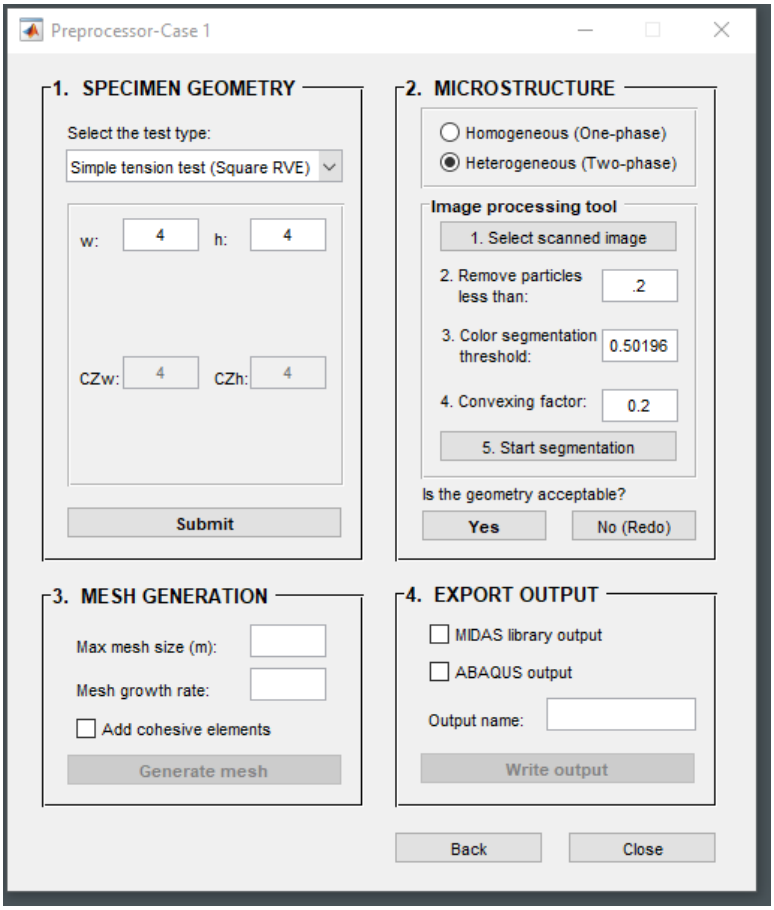

Figure A.4: MIDAS-VT-Pre Case I, image processing module.

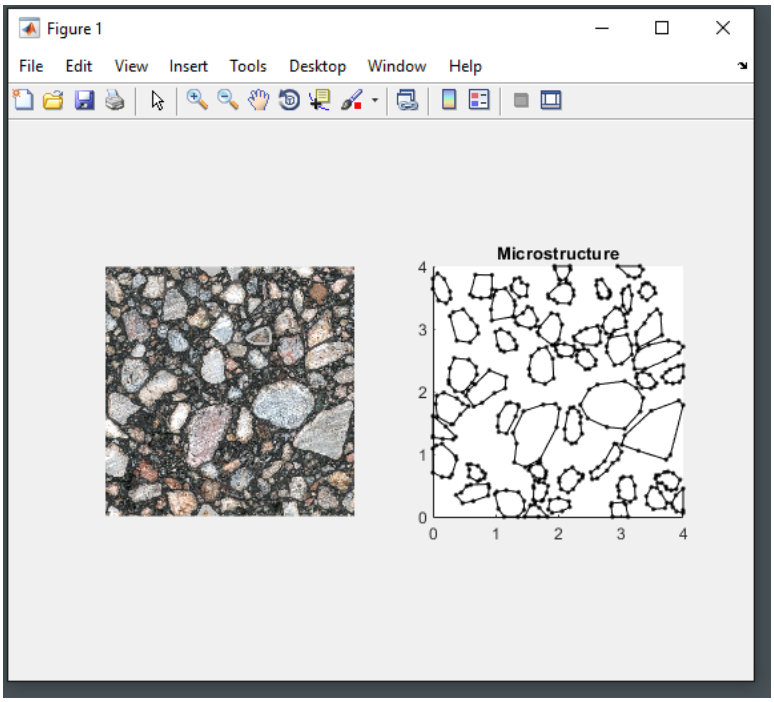

Figure A.5: Original image vs obtained microstructure.

be opened in Microsoft Paint for potential treatments. When the image treatment is finished, the user needs to do the image processing process again step one to five (see Figure A.4). This procedure may be repeated until the desired accuracy is obtained.

Mesh

The meshing module meshes the geometry using three-node elements. The user can adjust the maximum mesh size and *mesh growth rate*. The later one is specified as a scalar strictly between 1 and 2 and defines how the mesh size increases away from small parts of the geometry. The meshing module comes with an automated *cohesive element* insertion feature. Cohesive elements allow to simulate crack initiation and

propagation using *cohesive zone model*. Cohesive elements are zero thickness elements that links adjacent nodes of three-node elements [Rami et al., 2017]. The *add cohesive element* checkbox permits the user to add cohesive element between regular three-node elements over the RVE. The cohesive elements will be added within the matrix phase, which are labeled *cohesive element*, and particle-matrix interface, which are labeled *adhesive element*.

Export Output

The output produced by MIDAS-VT-Pre includes mesh data containing node coordinates and element connectivity matrix, element sets which list the elements ID within each set, and node sets which list the boundary nodes. The output data can be exported in two formats: one is compatible with MIDAS-VT, which is saved as a .mat file, the other is compatible with common FE software such as ABAQUS, which is saved as a .inp file. The later one contains the following information:

- Nodes coordinate matrix

```
*Node
Entry 1     Entry 2     Entry 3
. . .
```

  Entry 1: node ID

  Entry 2: x-coordinate of node

  Entry 3: y-coordinate of node

- Bulk elements connectivity matrix

```
*Element, type= Entry 0
Entry 1     Entry 2     Entry 3     Entry 4
```

```
. . .
```

Entry 0: bulk element type, which is *3-node*

Entry 1: element ID

Entry 2: 1st node number in global numbering system

Entry 3: 2nd node number in global numbering system

Entry 4: 3nd node number in global numbering system

- Cohesive element connectivity matrix

```
*Element, type= Entry 0
Entry 1     Entry 2     Entry 3     Entry 4     Entry 5
. . .
```

Entry 0: cohesive element type, which is *4-node cohesive*

Entry 1: element ID

Entry 2: 1st node number in global numbering system

Entry 3: 2nd node number in global numbering system

Entry 4: 3rd node number in global numbering system

Entry 5: 4th node number in global numbering system

- Element sets

```
*Elset, elset= Entry 0
Entry 1      [Entry 2] . . .
. . .
```

Set ID, which are: *Phase1*, which represents elements in matrix phase,

Entry 0: *Phase2*, which represents elements in particles,
Cohesive Elements,
and Adhesive Elements

Entry <i>: element ID

- Node sets

  This section will not be used in RVE studies and can be removed from the output.

A.3.2 Preprocessor Case II

This feature is provided for the case in which the model is meshed in advance using three-node elements. Selecting case II in Figure A.2, directs the user to MIDAS-VT-Pre Case II window, as shown in Figure A.6. To generate the model the user needs to finish steps one to four.

Specimen Geometry

Similar to the MIDAS-VT-Pre Case I the user must select test type (either simple tension or simple shear test) and input RVE dimensions as shown in Figure A.6. There is no need to specify the cracking region in this section. The cracking region is specified by introducing the elements within the cracking region as a separate set (see next section).

Input Mesh Data

The mesh data must include nodal coordinates, elemental connectivity, and element sets and be written in a single .txt or .inp file using the following format:

- Nodes coordinate matrix

```
*Node
Entry 1     Entry 2     Entry 3
. . .
```

  Entry 1: node ID

  Entry 2: x-coordinate of node

  Entry 3: y-coordinate of node

- Bulk elements connectivity matrix

```
*Element, type= Entry 0
Entry 1     Entry 2     Entry 3     Entry 4
. . .
```

  Entry 0: bulk element type, which is *3-node*

  Entry 1: element ID

  Entry 2: 1st node number in global numbering system

  Entry 3: 2nd node number in global numbering system

  Entry 4: 3nd node number in global numbering system

- Element sets

```
*Elset, elset= Entry 0
Entry 1      [Entry 2] . . .
. . .
```

Entry 0: Set ID, which are: *Phase1*, which represents elements in matrix phase,
Phase2, which represents elements in particles,
CZ, which represents cracking zone

Entry <i>: element ID

note: In common FE software such as ABAQUS, *partitioning* and *element set* tools are available to group elements in sets and assign associated tag.

Mesh Generation

This module adds zero thickness cohesive elements between bulk elements within the cracking region [Rami et al., 2017].

Export Output

This step is identical to export output in MIDAS-VT-Pre Case I.

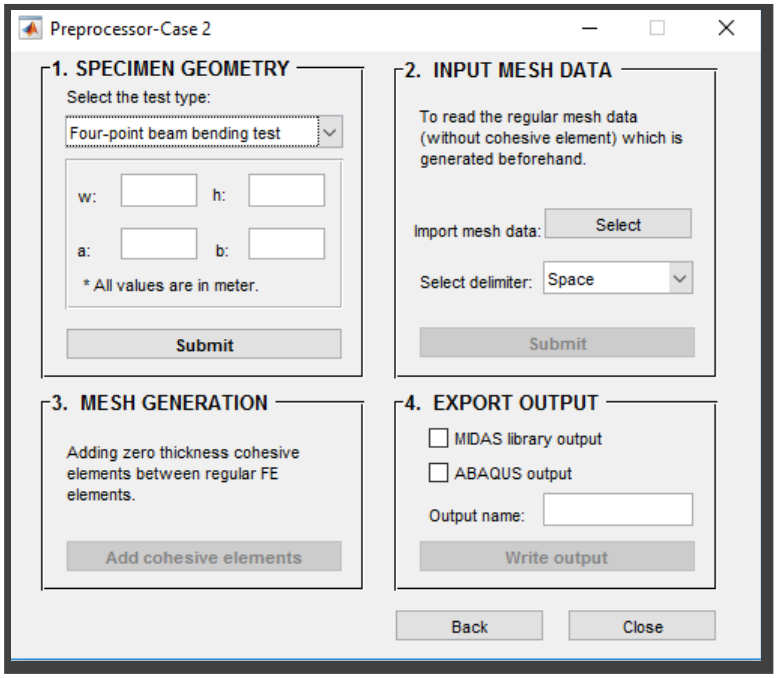

Figure A.6: MIDAS-VT-Pre Case II.